Spectral Integral Method and Spectral Element Method Domain Decomposition Method for Electromagnetic Field Analysis

by

Yun Lin

Department of Electrical and Computer Engineering
Duke University

Date: _____

Approved:

_____
Qing Huo Liu, Supervisor

_____
William T. Joines

_____
Tomoyuki Yoshie

_____
Gary A. Ybarra

_____
Anita T. Layton

Dissertation submitted in partial fulfillment of the requirements for the degree of Doctor of Philosophy in the Department of Electrical and Computer Engineering in the Graduate School of Duke University

2011

Abstract

(Electrical and Computer Engineering)

Spectral Integral Method and Spectral Element Method Domain Decomposition Method for Electromagnetic Field Analysis

by

Yun Lin

Department of Electrical and Computer Engineering
Duke University

Date: _____

Approved:

_____
Qing Huo Liu, Supervisor

_____
William T. Joines

_____
Tomoyuki Yoshie

_____
Gary A. Ybarra

_____
Anita T. Layton

An abstract of a dissertation submitted in partial fulfillment of the requirements for the degree of Doctor of Philosophy in the Department of Electrical and Computer Engineering
in the Graduate School of Duke University
2011

Abstract

In this work, we proposed a spectral integral method (SIM)-spectral element method (SEM)- finite element method (FEM) domain decomposition method (DDM) for solving inhomogeneous multi-scale problems. The proposed SIM-SEM-FEM domain decomposition algorithm can efficiently handle problems with multi-scale structures, by using FEM to model electrically small sub-domains and using SEM to model electrically large and smooth sub-domains. The SIM is utilized as an efficient boundary condition. This combination can reduce the total number of elements used in solving multi-scale problems, thus it is more efficient than conventional FEM or conventional FEM domain decomposition method. Another merit of the proposed method is that it is capable of handling arbitrary non-conforming elements. Both geometry modeling and mesh generation are totally independent for different sub-domains, thus the geometry modeling and mesh generation are highly flexible for the proposed SEM-FEM domain decomposition method. As a result, the proposed SIM-SEM-FEM DDM algorithm is very suitable for solving inhomogeneous multi-scale problems.

Contents

List of Tables

List of Figures

List of Abbreviations and Symbols

CFIE	Combined Field Integral Equation
DDM	Domain Decomposition Method
DG	Discontinuous Galerkin
EFIE	Electrical Field Integral Equation
FD	Finite Difference
FEM	Finite Element Method
FEM-BI	Finite Element Method - Boundary Integral
FFT	Fast Fourier Transform
GLL	Gauss Lobatto Legendre
IE	Integral Equation
MOM	Method of Moments
PEC	Perfect Electric Conductor
PMC	Perfect Magnetic Conductor
PML	Perfectly Matched Layer
RCS	Radar Cross Section

SEM Spectral Element Method

SIM Spectral Integral Method

SIE Surface Integral Equation

1

Introduction

1.1 Background

In recent years, the numerical electromagnetic analysis methods including finite difference method (FD), finite element method (FEM) and integral equation (IE) have been studied and applied in many areas such as scattering, radiation, electromagnetic compatible and signal integrity analysis. All of those popular methods have their own advantages and disadvantages. The surface integral equation (SIE) based methods are efficient in dealing with perfect electric conductor (PEC) or homogeneous structures, but have difficulties in dealing with inhomogeneous material. The FD and FEM are easy to model inhomogeneous targets. But in the FD and FEM based methods, computational domain in 3D space has to be discretized for a 3D problem; they also need field truncation on the boundary. However, these existing methods all have some difficulties when dealing with multi-scale problems, which have both electrically small structures and electrically large structures.

1.2 Problem Description

The electromagnetic scattering problems from arbitrary shaped inhomogeneous targets and with both electrically large parts and electrically fine structures in an unbounded background have received much attention for a long time. In these problems, targets are usually not just simple Perfect Electric Conductor (PEC) or homogeneous dielectric bodies alone, they can be composite objects with penetrable, inhomogeneous (ϵ_r and μ_r are functions of location) dielectric bodies and PEC bodies. In addition, these targets may have large parts (compared with wavelength), and contain many fine structures which cannot be ignored. Those structures are common in electromagnetic compatible, signal integrity analysis, antenna design and packaging problems. Take a simple patch antenna as an example. A patch antenna typically consists of PEC ground, PEC patch and dielectric substrate. The thickness of substrate is usually small, while the size of ground can be large. In other words, even in this simple patch antenna example we have material inhomogeneity together with multi-scale structure.

1.3 Challenges in the Problem

There are some theoretical difficulties in solving these problems. First, due to the complex shape, it is difficult to obtain any analytical solutions. Also because of the inhomogeneity of targets, surface integral equation cannot be used to solve these problems. Second, because of the unbounded background, any differential equation based method needs to truncate the field properly, but the most popular truncate methods such as absorbing boundary condition and perfect matched layer (PML) are not the best choices for solving these problems. For the absorbing boundary condition, it is not accurate. Using PML will result in the increasing system matrix size as well as the increasing condition number of the system matrix, especially for 3D

problems. The increasing system matrix size will lead to the large memory resource requirement in the solving process. Meanwhile the increasing condition number will result in a low convergence rate, when an iterative solver is used to solve the problem.

There are also some other practical difficulties for solving these problems. In order to use numerical methods to solve these problems, geometrical structures need to be meshed into elements, but the multi-scale geometrical nature of these problems makes the meshing with a global conforming mesh grid very difficult. Even though the mesh generator can generate the mesh grids, the number of the mesh grids is usually large, which is due to coexistence of the important fine structures and the global conforming mesh. Besides, the large number of mesh grids will require large computational resource to solve.

1.4 Contributions

We proposed a new spectral integral method (SIM) scheme for general 3D problem. This SIM is based on the surface integral equation. The surface of the SIM is chosen as cuboid. Because of the cuboid shape of the SIM surface and the shift invariant property of the Green's function, the SIM matrix has Toeplitz property. Then the fast Fourier transform algorithm is utilized to reduce the computational cost. As a result, the proposed SIM significantly reduces the computational cost from the conventional MOM solution of the integral equation. The memory requirement is reduced from $O(N^2)$ to $O(N^{1.5})$. At the same time, the CPU time cost of the matrix vector multiplication, which is repeatedly used in an iterative linear matrix solver, is reduced from $O(N^2)$ to $O(N^{1.5}\log N)$.

We proposed a hybridization of the spectral integral method (SIM) and spectral element method (SEM) by an interpolation matrix which is obtained from the boundary conditions on the interfaces between SIM and SEM. In the SIM-SEM scheme, the SIM is used as boundary condition of the SEM. This method is more efficient than

the conventional finite element method with boundary integral (FEM-BI) equation as boundary condition. In a test of dielectric cube problem, for the same prescribed accuracy, the presented SIM-SEM method shows 15 times faster than the conventional FEM-BI.

We implemented the FEM-SEM DDM algorithm via Robin's boundary condition and discontinuous Galerkin (DG) method. And the convergence properties of Robin's boundary condition and discontinuous Galerkin method have been studied. In a test of a dielectric cube problem, the DDM via discontinuous Galerkin method uses one third iterations as the DDM via Robin's boundary condition. The FEM-SEM DDM is applied to interconnect structures by the implementation of lumped element in FEM (SEM) region. Particularly, the FEM-SEM DDM algorithm is suitable for inhomogeneous multi-scale interconnect problems, because the proposed DDM algorithm can separate fine structures from other parts and generate mesh independently. Therefore this method is more efficient than the conventional FEM and FD methods.

We proposed the SIM-SEM-FEM DDM method which is implemented via discontinuous Galerkin method. The SIM is applied as the boundary condition of the SEM-FEM DDM. The discontinuous Galerkin method is used to connect the SIM and FEM (SEM) sub-domains, instead of using an interpolation matrix. The use of the discontinuous Galerkin method gives the ability to use non-conforming interface between SIM and SEM. Furthermore, the number of FEM (SEM) attached to SIM sub-domain can be multiple. As a result, the proposed SIM-SEM-FEM (DDM) algorithm suitable for solving inhomogeneous multi-scale problems.

2

Spectral Integral Method

2.1 Motivation

The surface integral equation method is widely used for the analysis of electromagnetic scattering problems for PEC or homogeneous targets. The surface integral equation method is based on the equivalence principle. The entire problem is divided into interior and exterior regions by an imaginary surface S, as shown in Fig. 2.1.

The scattered field in the exterior region is expressed by the surface equivalent electric and magnetic current on the surface S

$$\mathbf{E}^{sct} = \mathscr{L}\mathbf{J}_{eq} + \mathscr{K}\mathbf{M}_{eq} \tag{2.1}$$

where $\mathbf{J}_{eq}$ and $\mathbf{M}_{eq}$ are equivalent surface electric current density and magnetic current density, respectively. $\mathscr{L}$ and $\mathscr{K}$ will be defined latter.

The boundary conditions are used on the surface to connect the interior and exterior problems. (If the interior region is a homogeneous problem or a PEC problem, the problem can be solved by surface integral equation itself.)

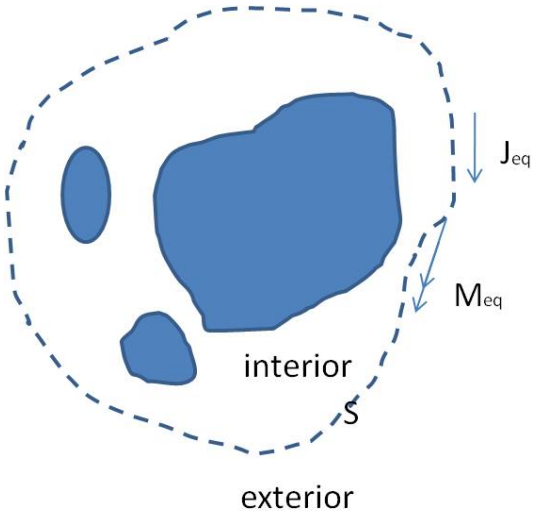

FIGURE 2.1: Equivalent electric and magnetic currents in equivalence principle

Surface integral equation in electromagnetic scattering problems is traditionally solved by the method of moments (MOM)[1]. The conventional MOM has high computational complexity. The memory cost is proportional to $O(N^2)$, and the CPU time cost in an iterative solver is also proportional to $O(N^2)$, where N is the number of unknowns.

There are several fast algorithms developed for accelerating the MOM calculation, such as the fast multipole method [2, 3] and the adaptive integral method [4, 5]. But both of them are complex in theory and difficult to implement.

In this work, an alternative method - spectral integral method (SIM) - is proposed to accelerate the MOM solution. The spectral integral method is based on the surface integral method. Because of the shift invariant property of the Green's function, the SIM system matrix has Toeplitz property. The Toeplitz matrix can be expressed by only one row and one column, thus the memory requirement in SIM is significantly reduced. Furthermore, as the product of a Toeplitz matrix and a vector can be calculated via fast Fourier transform, the CPU time is also reduced in SIM. In some previous studies, the Toeplitz structure of the integral equation system matrix of

planar structures has been utilized to accelerate the IE. The FFT accelerated IE is used as the boundary condition of FEM for some special cases, with planar surface structure such as cavity-backed aperture [6, 7]. In this work, a general way to apply SIM in 3D on a cuboid surface is presented.

2.2 Formulation

In this section, the detailed formulation of the SIM will be discussed [8]. The electric field surface integral equation (EFIE) as in Eq. 2.1 can be expressed as

$$\hat{\mathbf{n}} \times \mathbf{E}^{inc}(\mathbf{r}) = -\mathbf{M}(\mathbf{r}) + \hat{\mathbf{n}} \times \int_S [jk_b\eta_b g_b(\mathbf{r},\mathbf{r}')\mathbf{J}(\mathbf{r}')$$

$$+\frac{j\eta_b}{k_b}\nabla g_b(\mathbf{r},\mathbf{r}')\nabla'\cdot\mathbf{J}(\mathbf{r}')+\nabla g_b(\mathbf{r},\mathbf{r}')\times\mathbf{M}(\mathbf{r}')\Big]\, ds(\mathbf{r}') \tag{2.2}$$

where g_b is the Green's function of background; k_b and η_b are the wave number and impedance of the background, respectively; $\hat{\mathbf{n}}$ is the unit vector of the outer normal direction of the imaginary surface S, $\mathbf{E}^{inc}$ stand for the incident electric field and magnetic field, respectively.

Notice that the surface current density cannot be directly solved from the surface integral equation. However, coupling the surface current with the field on the interface makes the whole system solvable.

The next step is construction of the discretized linear system. The electric and magnetic current densities can be expressed by superposition of rooftop basis functions as

$$\mathbf{J}(\mathbf{r}) = \sum_{n=1}^{N_j} j_n \mathbf{f}_n(\mathbf{r}) \tag{2.3}$$

$$\mathbf{M}(\mathbf{r}) = \sum_{n=1}^{N_j} m_n \mathbf{f}_n(\mathbf{r}) \tag{2.4}$$

where $\{j_n\}$ and $\{m_n\}$ are the expansion coefficients of electric and magnetic current densities, and $\mathbf{f}_n$ is the rooftop basis function which can be expressed as

$$\mathbf{f}_n^x(\mathbf{r}) = \begin{cases} \hat{\mathbf{x}}(1-|x|/h_x) & -h_x \le x < h_x \\ 0 & \text{otherwise} \end{cases} \tag{2.5}$$

$$\mathbf{f}_n^y(\mathbf{r}) = \begin{cases} \hat{\mathbf{y}}(1-|y|/h_y) & -h_y \le y < h_y \\ 0 & \text{otherwise} \end{cases} \tag{2.6}$$

$$\mathbf{f}_n^z(\mathbf{r}) = \begin{cases} \hat{\mathbf{z}}(1-|z|/h_z) & -h_z \le z < h_z \\ 0 & \text{otherwise.} \end{cases} \tag{2.7}$$

Substituting the expansions of $\mathbf{J}$ and $\mathbf{M}$ into the integral equation (2.2), and applying Galerkin procedure yields the system matrix, which can be expressed in a matrix form

$$[\mathbf{Z}^{(1)} + \mathbf{Z}^{(2)}]\mathbf{J} + \mathbf{Z}^{(3)}\mathbf{M} = \mathbf{Z}_a\mathbf{J} + \mathbf{Z}_b\mathbf{M} = \mathbf{S}^e \tag{2.8}$$

The detailed formulation of $\mathbf{Z}^{(1)}$, $\mathbf{Z}^{(2)}$, and $\mathbf{Z}^{(3)}$ can be expressed as

$$\mathbf{Z}_{mn}^{(1)} = jk_b\eta_b \int_S ds(\mathbf{r})\mathbf{f}_m(\mathbf{r}) \cdot \int_S ds(\mathbf{r}')g_b(\mathbf{r},\mathbf{r}')\mathbf{f}_n(\mathbf{r}')$$

$$\mathbf{Z}_{mn}^{(2)} = \frac{\eta_b}{jk_b} \int_S ds(\mathbf{r})\nabla\cdot\mathbf{f}_m(\mathbf{r}) \cdot \int_S ds(\mathbf{r}')g_b(\mathbf{r},\mathbf{r}')\nabla'\cdot\mathbf{f}_n(\mathbf{r}') \tag{2.9}$$

$$\mathbf{Z}_{mn}^{(3)} = \frac{\eta_b}{jk_b} \int_S ds(\mathbf{r})\mathbf{f}_m(\mathbf{r}) \cdot [-\frac{1}{2}\mathbf{f}_n(\mathbf{r}) + \int_S ds(\mathbf{r}')\nabla g_b(\mathbf{r},\mathbf{r}')\times\mathbf{f}_n(\mathbf{r}')]$$

The next step is to utilize the FFT to accelerate the SIE. The core task of the SIM is to accelerate the multiplication of the system matrix and a vector ($\mathbf{Z}_a\mathbf{J}$ or $\mathbf{Z}_b\mathbf{M}$), which is used in iterative solvers such as conjugate gradient (CG), biconjugate gradient stabilized method (BICGStab(ℓ)) and Generalized minimal residual method (GMRES). The SIM is applied on the interface S, which in general can be chosen arbitrarily. But different choices of S may result in different computational

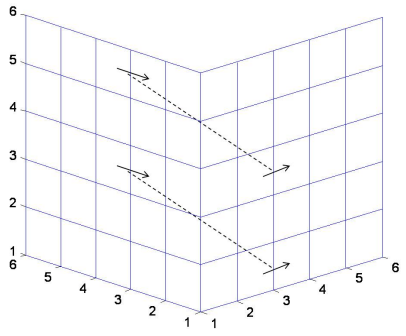

FIGURE 2.2: Shift invariant of Green's function on a cuboid surface. Scenario 1, basis function and testing function are on the adjacent planes case

complexity [9]. In this work, a cuboid is used as the SIM surface. This choice can result in the Toeplitz property in the SIM matrix.

All SIM basis functions are located on these six planar surfaces of the cuboid. Considering all combinations of geometrical locations of basis and testing functions, there are two different scenarios. First, when the basis functions and testing functions are located on two adjacent surfaces, the SIM matrix is a 1D Toeplitz matrix as shown in Fig. 2.2. Let's consider a cuboid which is discretized into N_x, N_y, N_z grids in $\hat{x}$, $\hat{y}$, $\hat{z}$ direction, with grid size Δx, Δy, Δz. The distance between basis function and testing function can be expressed as

$$d = [((N_x - m)\Delta x)^2 + ((N_y - n)\Delta y)^2 + ((p_1 - p_2)\Delta z)^2]^{\frac{1}{2}} \tag{2.10}$$

Second, when the basis functions and testing functions are located on the same surface or opposite surfaces, the SIM matrix is a 2D Toeplitz matrix as shown in Fig. 2.3 and Fig. 2.4. The distance between basis function and testing function can be expressed as

$$d = [((m_1 - m_2)\Delta x)^2 + ((n_1 - n_2)\Delta y)^2 + \delta_{pq}(N_z\Delta z)^2]^{\frac{1}{2}} \tag{2.11}$$

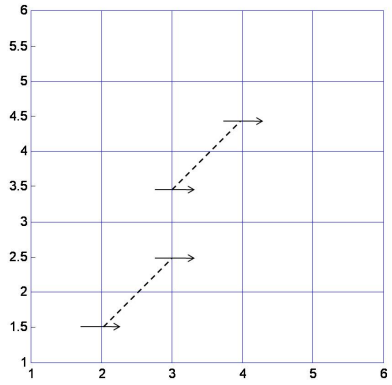

FIGURE 2.3: Shift invariant of Green's function on a cuboid surface. Scenario 2, basis function and testing function are on the same plane case

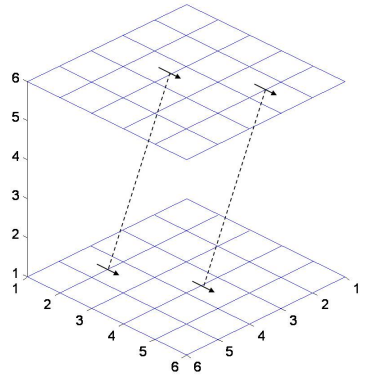

FIGURE 2.4: Shift invariant of Green's function on a cuboid surface. Scenario 2, basis function and testing function are on the opposite planes case

$$\delta_{pq} = \begin{cases} 1 & p = q \\ 0 & \text{otherwise} \end{cases} \tag{2.12}$$

Note that the computational complexity is dominated by the first scenario.

In both scenarios, there is a special case. Since rooftop basis functions are used in the SIM part, those basis functions located on edges have support on two orthogonal surfaces. Thus, the Toeplitz property is not valid for these basis functions. To

consider these special matrix entries, a remainder matrix is introduced

$$\mathbf{Z} = \mathbf{Z}_T + \mathbf{Z}_R \tag{2.13}$$

where $\mathbf{Z}_T$ is the Toeplitz part of the system matrix, and $\mathbf{Z}_R$ is the remainder part of the system matrix, which is highly sparse and can be stored directly.

The computational complexity can be analyzed by assuming that the cuboid surface has N_x, N_y, N_z cells in the $\hat{x}, \hat{y}, \hat{z}$ directions, respectively. The total unknowns for the SIM on the surface will be $N = 8(N_xN_y + N_xN_z + N_yN_z)$ including $\mathbf{J}$ and $\mathbf{M}$. If the conventional MOM is used, the system matrix is a full matrix, and the total number of matrix entries is N^2. Thus, if the matrix-vector multiplication is performed directly, the storage and the computation complexity will be $O(N^2)$ in an iterative solver. On the other hand, using SIM, for Z_T part, where the Toeplitz property is used, there are 144 combinations of the positions of basis and testing functions. Among these 144 combinations, 96 combinations belong to the first scenario, 48 combinations belong to the second scenario. For the first scenario, the memory cost is $O(96N_xN_yN_z)$, the CPU time cost is $O[32N_xN_yN_z \log(N_xN_yN_z)]$. For the second scenario, the memory cost is $O[16(N_xN_y + N_xN_z + N_yN_z)]$, the CPU time cost is $O[16(N_xN_y)\log(N_xN_y) + 16(N_xN_z)\log(N_xN_z) + 16(N_yN_z)\log(N_yN_z)]$. And for the Z_R part the memory and CPU time cost are $O[32(N_x+N_y+N_z)(N_xN_y+N_xN_z+N_yN_z)]$. The total cost for the SIM part is summation of the cost for Z_T part and Z_R part. Assuming $N_x = N_y = N_z$, then for the SIM-SEM the memory cost can be simplified to $O(N^{1.5})$, and the CPU time cost can be simplified to $O[N^{1.5}\log(N)]$.

In detail, the matrix-vector multiplication can be obtained as

$$\mathbf{Zv} = \mathbf{Z}_T\mathbf{v} + \mathbf{Z}_R\mathbf{v} \tag{2.14}$$

where the first term can be obtained through the FFT, but the second term needs to be calculated directly. Fortunately, since the $\mathbf{Z}_R$ is only associated with the edges, it

is highly sparse. The computational complexity for this part is also $O(N^{1.5})$. So the final computational complexity for the SIM part is $O(N^{1.5})$, as validated in numerical results.

The matrix-vector multiplication in the SIM will be discussed here. If the product of Toeplitz matrix $\mathbf{Z}_T$ and a vector $\mathbf{v}$ is needed, first a circulant vector $\mathbf{t}$ is defined as

$$\mathbf{t}_{i-j} = (\mathbf{Z}_T)_{ij} \qquad \text{i,j} = 1, \cdots, N_x \tag{2.15}$$

where the Toeplitz matrix in the x direction is given as an example (other directions are similar). Vector $\mathbf{v}'$ is obtained by zero padding

$$\mathbf{v}' = \begin{bmatrix} \mathbf{v} \\ 0 \end{bmatrix} \tag{2.16}$$

Then, use the fast Fourier transform to obtain the matrix-vector multiplication of $\mathbf{Z}_T\mathbf{v}'$

$$\mathbf{Z}_T\mathbf{v}' = \mathcal{F}^{-1}[\mathcal{F}(\mathbf{t})\mathcal{F}(\mathbf{v}')] \tag{2.17}$$

For some iterative solvers like the conjugate gradient squared (CGS) method requiring the conjugate transpose of the matrix $\mathbf{Z}_T^\dagger$, the product $\mathbf{Z}_T^\dagger\mathbf{v}'$ also can be easily obtained:

$$\mathbf{Z}_T^\dagger\mathbf{v}' = \mathscr{F}^{-1}(\mathscr{F}(\mathbf{t})\mathscr{F}(\mathbf{v}'^*))^* \tag{2.18}$$

where * denotes complex conjugate operation. $\mathcal{F}$ and $\mathcal{F}^{-1}$ indicates a FFT and an inverse FFT. 2D Toeplitz matrix-vector multiplications can be done in a similar way.

2.3 Numerical Examples

The first example is shown to validate of the SIM; a PEC cube problem is solved by MOM and SIM respectively. The edge length of the cube is 0.755 m. The frequency

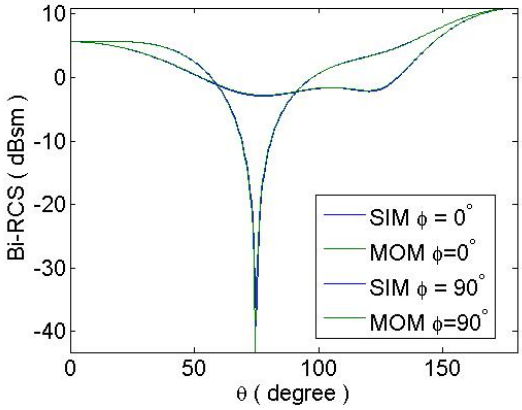

FIGURE 2.5: The Bi-static RCS of a PEC cube SIM and MOM comparison in $\phi = 0°$, and $\phi = 90°$ plane at 300 MHz.

of the incident plane wave is 300 MHz. The incident plane wave propagating in $\hat{z}$ direction has the polarization of the electric field in the $\hat{x}$ direction. The Bi-static results obtained from SIM-SEM and reference results have very good agreement as in Fig. 2.5.

The next example is a PEC cube which can not be solved by surface integral equation MOM solution because of the memory restriction, but it can be solved by proposed SIM. The edge length of the PEC cube is 4 m. The frequency of the incident plane wave is 300 MHz. The incident plane wave propagating in the $\hat{z}$ direction has a polarization of the electric field in the $\hat{x}$ direction. The results obtained from SIM-SEM and reference results [10] have very good agreement as shown in Fig. 2.6 and Fig. 2.7 .

Next, the computational complexity of the proposed SIM is studied by using different meshes for a PEC cube problem. The CPU time and memory costs in the SIM and MOM are shown in Fig. 2.8 and Fig. 2.9, indicating that the SIM has a CPU time complexity of $O(N^{1.5}logN)$ and memory complexity of $O(N^{1.5})$, compared with the $O(N^2)$ complexity for MOM in both CPU time and memory. In particular, we find that the CPU time for MOM is about 6 times higher for $N = 20,000$. The

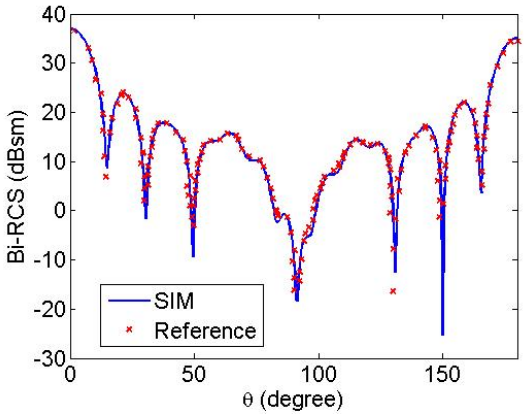

FIGURE 2.6: The Bi-static RCS of a PEC cube with 4 m in $\phi = 0°$ plane at 300 MHz.

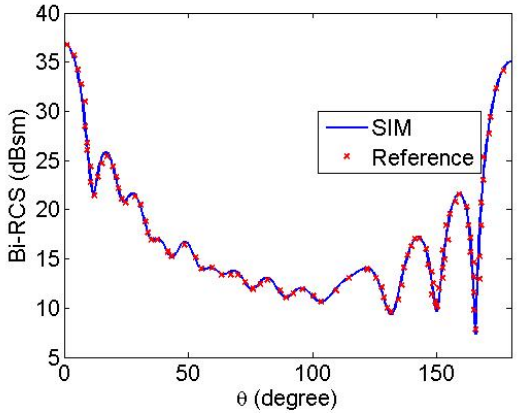

FIGURE 2.7: The Bi-static RCS of a PEC cube with 4 m in $\phi = 90°$ plane at 300 MHz.

acceleration factor increases more rapidly for larger problems.

2.4 Conclusion

In this chapter, we proposed a general way to apply 3D SIM on a cuboid surface. The proposed SIM utilizes the Toeplitz property of the system matrix. The fast Fourier transform is used to reduce the computational cost both in terms of memory and the CPU time. As a result, the memory cost of the proposed SIM is reduced from $O(N^2)$

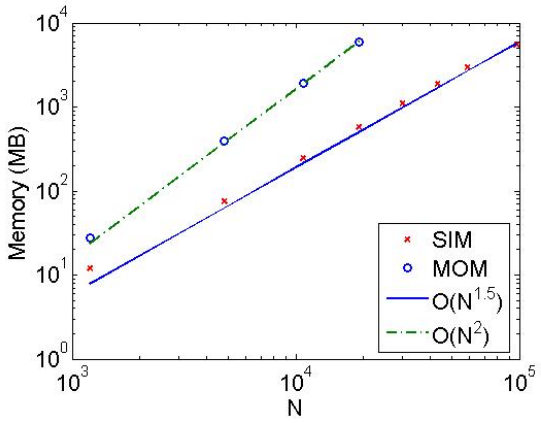

FIGURE 2.8: Comparison of the memory complexity of SIM and MOM of a PEC cube problem.

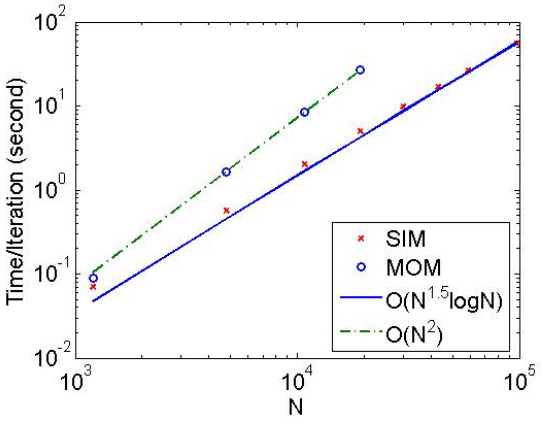

FIGURE 2.9: Comparison of the CPU time of SIM and MOM of a PEC cube problem.

of the conventional MOM to $O(N^{1.5})$, and the CPU time is reduced from $O(N^2)$ of the conventional MOM to $O(N^{1.5}\log N)$. The computational complexity has been analyzed theoretically and validated numerically. The proposed SIM can be used as the boundary condition in FEM. And the hybridization of SIM and SEM (FEM) is discussed in the next chapter.

3

Spectral Integral Method - Spectral Element Method

3.1 Motivation

The FEM is one of the most popular frequency-domain algorithms for inhomogeneous objects [11, 12], because of its ability to deal with complex geometry and material inhomogeneities. However, for scattering problems, the FEM requires an absorbing boundary condition such as the perfectly matched layer (PML) [13] to truncate an unbounded domain. The incorporation of PML has been demonstrated to increase the number of unknowns as well as the condition number of the system matrix [14]. Alternatively, surface integral equation (SIE) based methods such as the method of moments (MOM) can be used to model an arbitrary object with high accuracy, but they are limited to homogeneous (or piecewise homogeneous) targets; and they have high computational complexity. There are some fast algorithms such as FMM, AIM and SIM can be used to reduce the complexity.

The finite element method-boundary integral (FEM-BI) method was proposed for electromagnetic scattering problems first for 2D problems [15], and then for 3D

problems [16, 17, 18, 19]. In the FEM-BI method, a boundary integral equation is used as the radiation boundary condition of the FEM. As a result, an approximate absorbing boundary condition or a PML is not required. But the memory and CPU time cost of the boundary integral part are both expensive, so this method is limited to relatively small problems. The fast multipole method [20, 21] and adaptive integration method [4] have been used to reduce the computational cost of the boundary integral part. An alternative way is to use FFT to accelerate boundary integral part. The FFT accelerated SIE has been applied to 2D and 3D structures with planar surfaces, including PEC backed aperture structures and slots in a thick PEC plane [6, 7]. Based on the 2D spectral integral method for homogeneous and layered background media [22, 23], the 2D hybrid SIM-FEM method has been studied [24, 8], where the 2D version of SIM utilizes the FFT algorithm to treat the surface integral.

The spectral integral method-spectral element method (SIM-SEM) is proposed to solve 3D electromagnetic scattering from inhomogeneous objects. In this chapter, we focused on the scattering from an arbitrary shaped and arbitrary inhomogeneous object in a homogeneous background. In the hybridization of SIM-SEM, the SEM part provides the capability to deal with complex geometry structure and material properties with high efficiency, and the SIM part provides an accurate radiation boundary condition. By choosing the order of the SEM basis functions and size of two sets of meshes, an efficient combination of the SIM and the SEM can be achieved. However, the method proposed here requires the surface to be a cuboid to utilize the fast Fourier transform. For an arbitrary shaped object, we can always find the smallest cuboid to enclose the object, although it includes a larger solving space than using the actual boundary of the object. Nevertheless, compared with a spherical enclosure which only has one degree or freedom (radius), the cuboid has three degrees of freedom (namely the lengths in x, y and z directions). So that

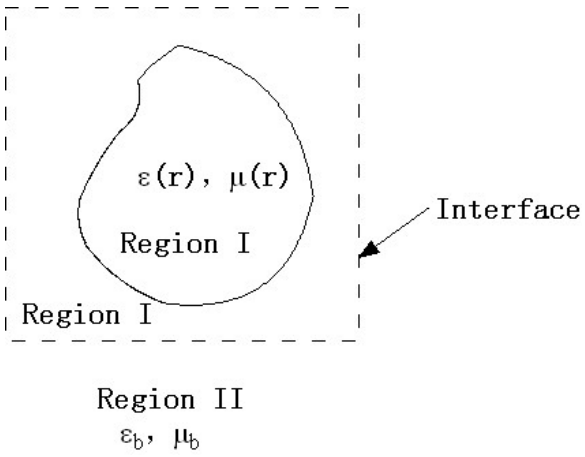

FIGURE 3.1: The SIM-SEM problem description.

the computational volume can be made smaller for most objects than a spherical enclosure (one exception is a spherical or nearly spherical object).

3.2 Formulation

In this part, first the overall scheme of the hybrid technique is presented, and then the detailed formulations of SIM and SEM and their combination is discussed.

3.2.1 Overall Scheme

In the SIM-SEM method, the whole space is divided into two regions, the interior region (region I), which includes all inhomogeneous objects, and the exterior region (region II), which is the homogeneous background, as shown in Fig. 3.1. The object has inhomogeneous, relative complex permittivity and permeability distributions denoted by $\epsilon_r(\mathbf{r})$ and $\mu_r(\mathbf{r})$, respectively.

For the interior region, the SEM is used to deal with all the inhomogeneities. The SEM is a higher order version of FEM with special nodal distributions and basis function definition. It can achieve exponential error convergency with increase of order, and without spurious modes [25]. The unknowns for the interior problem are electric field in region I, and the tangential electric field and magnetic field on the

interface.

For the exterior region, according to the equivalence principle, the scattered field in region II can be obtained from the equivalent surface electric and magnetic current densities on the interface. To model the surface electric and magnetic current densities, the SIM is used based on the surface integral equation on a cuboid. The unknowns for this part are equivalent electric current density and magnetic current density on the interface.

On the interface, unknowns from SEM (the tangential components of electric field and magnetic field) and those from SIM (equivalent surface electric and magnetic current densities) are related via the boundary conditions (the tangential components of electric field and magnetic field are continuous). The two sets of unknowns can be expressed by each other through an interpolation matrix.

An iterative solver is used to solve the final system matrix obtained above. In each iteration, the matrix-vector multiplication is accelerated by the FFT algorithm, for the SIM part. The detailed formulation will be discussed below for the SEM and SIM equations, FFT acceleration of the matrix-vector multiplications and the interpolation between SIM and SEM.

3.2.2 The SEM for the Interior Region

The SEM is used to model the field distribution in the interior region (region I) [25]. High mixed-order vector Gauss-Lobatto-Legendre (GLL) polynomials are used as the basis functions with 3D spatial discretization by curved hexahedron elements. The expression of the 1D scalar GLL polynomial defined on a 1D standard element $\xi \in [-1, 1]$ is

$$\phi_j^{(N)}(\xi) = \frac{-1}{N(N+1)L_N(\xi_j)} \frac{(1-\xi^2)L'_N(\xi)}{\xi - \xi_j} \tag{3.1}$$

where $L_N(\xi)$ and $L'_N(\xi)$ are the Nth-order Legendre polynomial and its derivative, respectively; ξ_j is the jth GLL point in the reference domain $\xi \in [-1, 1]$. The GLL points are defined as roots of equation $(1-\xi_j^2)L'_N(\xi_j) = 0$. The high mixed-order vector GLL basis function, defined on a standard 3-D cubic element, are adopted for high accuracy and to avoid the spurious modes in SIM-SEM. A high mixed-order vector GLL basis function is a multiplication of three scalar GLL basis functions, which are functions of three orthogonal coordinate variables ξ, η, ζ respectively. The order of the scalar GLL basis function, which has the same variable as the direction of this vector basis function, is one order lower than the interpolation order in this direction. The other two scalar basis functions have the same order as the interpolation order in those two directions, respectively. The expressions for the vector GLL basis functions in a reference cubic element are

$$\begin{aligned}
\mathbf{\Phi}^{\xi}_{rst} &= \hat{\xi}\phi_r^{N_\xi - 1}(\xi)\phi_s^{N_\eta}(\eta)\phi_t^{N_\zeta}(\zeta) \\
\mathbf{\Phi}^{\eta}_{rst} &= \hat{\eta}\phi_r^{N_\xi}(\xi)\phi_s^{N_\eta - 1}(\eta)\phi_t^{N_\zeta}(\zeta) \\
\mathbf{\Phi}^{\zeta}_{rst} &= \hat{\zeta}\phi_r^{N_\xi}(\xi)\phi_s^{N_\eta}(\eta)\phi_t^{N_\zeta - 1}(\zeta)
\end{aligned} \tag{3.2}$$

where N_ξ, N_η, N_ζ are interpolation orders of the vector GLL basis function in $\hat{\xi}, \hat{\eta}, \hat{\zeta}$ directions respectively, and $\mathbf{\Phi}^{\xi}_{rst}, \mathbf{\Phi}^{\eta}_{rst}, \mathbf{\Phi}^{\zeta}_{rst}$ are the vector GLL basis functions in $\hat{\xi}, \hat{\eta}, \hat{\zeta}$ directions, respectively. Then an arbitrary vector can be expressed by summation of vector GLL basis functions. If $\mathbf{E}$ field is chosen as the unknown, it can be expressed in a reference cubic element as

$$\begin{aligned}
\mathbf{E}(\xi,\eta,\zeta) = & \sum_{r=0}^{N_\xi - 1}\sum_{s=0}^{N_\eta}\sum_{t=0}^{N_\zeta} E^{\xi}(\xi_r,\eta_s,\zeta_t)\mathbf{\Phi}^{\xi}_{rst} + \sum_{r=0}^{N_\xi}\sum_{s=0}^{N_\eta - 1}\sum_{t=0}^{N_\zeta} E^{\eta}(\xi_r,\eta_s,\zeta_t)\mathbf{\Phi}^{\eta}_{rst} \\
& + \sum_{r=0}^{N_\xi}\sum_{s=0}^{N_\eta}\sum_{t=0}^{N_\zeta - 1} E^{\zeta}(\xi_r,\eta_s,\zeta_t)\mathbf{\Phi}^{\zeta}_{rst} = \sum_{j=1}^{N^{(e)}} E_j \mathbf{\Phi}_j
\end{aligned} \tag{3.3}$$

where $N^{(e)} = N_\xi(N_\eta+1)(N_\zeta+1)+(N_\xi+1)N_\eta(N_\zeta+1)+(N_\xi+1)(N_\eta+1)N_\zeta$ is the number of basis functions in a single hexahedron element, $j=(r,s,t)$ is a compound index, and $\{E_j\}$ are the expansion coefficients.

The vector wave equation for electric field $\mathbf{E}$ can be expressed as

$$\nabla \times (\mu_r^{-1}\nabla \times \mathbf{E}) - k_0^2\epsilon_r\mathbf{E} = -jk_0\eta_0\mathbf{f} \tag{3.4}$$

where $\mathbf{E}$ is the electric field, μ_r, ϵ_r are the relative complex permeability and permittivity, respectively; η_0 is the intrinsic impedance in free space; k_0 is the wave number in free space; and $\mathbf{f}$ is the excitation term.

The weak form of the vector wave equation for $\mathbf{E}$ can be expressed as

$$\int_V [\mathbf{\Phi}_i \cdot \nabla\times(\mu_r^{-1}\nabla\times\mathbf{E}) - k_0^2\epsilon_r\mathbf{\Phi}_i\cdot\mathbf{E}]dv = -jk_0\eta_0\int_V \mathbf{\Phi}_i\cdot\mathbf{f}dv \tag{3.5}$$

Using integration by parts, $\nabla\times$ operator is applied on Φ_i

$$\begin{aligned}&\int_V [\nabla\times\mathbf{\Phi}_i\cdot(\mu_r^{-1}\nabla\times\mathbf{E}) - k_0^2\epsilon_r\mathbf{\Phi}_i\cdot\mathbf{E}]dv \\ &= \int_S \mu_r^{-1}\mathbf{\Phi}_i\times(\nabla\times\mathbf{E})\cdot\hat{\mathbf{n}}ds - jk_0\eta_0\int_V\mathbf{\Phi}_i\cdot\mathbf{f}dv\end{aligned} \tag{3.6}$$

where S is the outer surface of Region I, $\hat{\mathbf{n}}$ is the unit vector of outer normal direction of S. From Maxwell's equation $\nabla\times\mathbf{E}$ can be express by $\mathbf{H}$

$$\nabla\times\mathbf{E} = -j\omega\mu\mathbf{H} \tag{3.7}$$

Substituting the above equation into equation (3.6) for $\nabla\times\mathbf{E}$ in the boundary integration term leads to

$$\begin{aligned}&\int_V [\nabla\times\mathbf{\Phi}_i\cdot(\mu_r^{-1}\nabla\times\mathbf{E}) - k_0^2\epsilon_r\mathbf{\Phi}_i\cdot\mathbf{E}]dv \\ &= -j\omega\mu_0\oint_S(\mathbf{\Phi}_i\times\mathbf{H})\cdot\hat{\mathbf{n}}ds - jk_0\eta_0\int_V\mathbf{\Phi}_i\cdot\mathbf{f}dv\end{aligned} \tag{3.8}$$

Substituting the GLL vector basis function expansion form of electric field and magnetic field, the matrix form of the SEM equation can be obtained

$$\mathbf{A}\tilde{\mathbf{e}} + \mathbf{G}\tilde{\mathbf{h}^b} = \mathbf{S}^i \tag{3.9}$$

where

$$A_{ij} = \sum_{e=1}^{K} \left[\int_{V_e} (\mu_r^{-1} \nabla \times \mathbf{\Phi}_i) \cdot (\nabla \times \mathbf{\Phi}_j) dv - k_0^2 \int_{V_e} \epsilon_r \mathbf{\Phi}_i \cdot \mathbf{\Phi}_j dv \right] \tag{3.10}$$

$$G_{ij} = -j\omega\mu_0 \sum_{b=1}^{K_b} \oint_{S_e} (\mathbf{\Phi}_i \times \mathbf{\Phi}_j) \cdot \hat{\mathbf{n}} ds \tag{3.11}$$

$$S_i^i = -jk_0\eta_0 \int_{V_e} \mathbf{\Phi}_i \cdot \mathbf{f} dv \tag{3.12}$$

where K is the total number of elements; K_b is the number of boundary elements.

For the convenience of combining with the SIM on the interface, the basis functions located inside region I and on the interface are explicitly separated

$$\mathbf{A}^{ii}\tilde{\mathbf{e}}^i \quad + \mathbf{A}^{bi}\tilde{\mathbf{e}}^b = \mathbf{S}^i \tag{3.13}$$

$$\mathbf{A}^{ib}\tilde{\mathbf{e}}^i \quad + \mathbf{A}^{bb}\tilde{\mathbf{e}}^b + \mathbf{G}\tilde{\mathbf{h}}^b = 0 \tag{3.14}$$

where $\mathbf{A}^{ii}$ is the coupling between inner basis functions and inner testing functions, $\mathbf{A}^{ib} = (\mathbf{A}^{bi})^T$ is the coupling between the inner basis functions and boundary testing functions, $\mathbf{A}^{bi}$ is the coupling between the boundary basis functions and inner testing functions, $\mathbf{A}^{bb}$ is the coupling between the boundary basis functions and boundary testing functions. $\mathbf{G}$ represents the boundary tangential magnetic field contribution. $\tilde{\mathbf{e}^i}$ is the electric field unknown vector in region I. $\tilde{\mathbf{e}^b}$ is the electric field unknown vector on boundary. $\tilde{\mathbf{h}^b}$ is the magnetic field unknown vector on boundary. The tilde on the vectors indicates that these vectors are defined in the reference domain instead of the physical domain. The vectors defined in reference domain and in physical domain can be related by the Jacobian matrix [25].

3.2.3 The SIM for the Outer Boundary

In this section, the main objective is to express the scattered field in region II by equivalent electric current and magnetic current. This is done by the same way as discussed in chapter 2, so we are not going to repeat it here.

3.2.4 The Interpolation Between SIM and SEM

As discussed above in the SEM part, high mixed-order GLL basis functions are used with $\tilde{e}^i$, $\tilde{e}^b$, and $\tilde{h}^b$ as unknowns. In the SIM part, rooftop basis functions are used with $\mathbf{J}$ and $\mathbf{M}$ as unknowns. However, the surface unknowns $\tilde{e}^b$ and $\tilde{h}^b$ are not independent of $\mathbf{J}$ and $\mathbf{M}$. The interpolation between these two sets of unknowns on the interface is required .

First, from the equivalent current density on the interface, we have

$$\mathbf{J}(\mathbf{r}) = \hat{\mathbf{n}} \times \mathbf{H}(\mathbf{r})|_S \tag{3.15}$$

$$\mathbf{M}(\mathbf{r}) = -\hat{\mathbf{n}} \times \mathbf{E}(\mathbf{r})|_S \tag{3.16}$$

where $\mathbf{J}$ and $\mathbf{M}$ are expressed in terms of the SIM basis functions, while $\mathbf{E}$ and $\mathbf{H}$ are expressed in term of the SEM basis functions. In other words, on the interface we have

$$\mathbf{M}(\mathbf{r}) = \sum_{m=1}^{N_j} m_m \mathbf{f}_m(\mathbf{r}) = -\hat{\mathbf{n}} \times \mathbf{E}(\mathbf{r})|_S = -\hat{\mathbf{n}} \times \sum_{n=1}^{N_b} E_n \mathbf{\Phi}_\mathbf{n}(\mathbf{r}) \tag{3.17}$$

$$\mathbf{J}(\mathbf{r}) = \sum_{m=1}^{N_j} j_m \mathbf{f}_m(\mathbf{r}) = \hat{\mathbf{n}} \times \mathbf{H}(\mathbf{r})|_S = \hat{\mathbf{n}} \times \sum_{n=1}^{N_b} H_n \mathbf{\Phi}_\mathbf{n}(\mathbf{r}) \tag{3.18}$$

where N_b is the number of SEM unknowns on the interface, and N_j is the number of SIM unknowns. Then the relationships between $\mathbf{J}, \mathbf{M}$ and $\mathbf{E}, \mathbf{H}$ are constructed

so that only one set of unknowns remains as the unknowns in the final system. In this paper, $\mathbf{J}$ and $\mathbf{M}$ are chosen as the final unknowns on the surface, because for scattering problems surface currents are more convenient for obtaining far-field pattern or radar cross section (RCS) and the SIM basis functions have lower order. To express $\mathbf{E}$ and $\mathbf{H}$ in terms of $\mathbf{J}$ and $\mathbf{M}$, function $\delta(\mathbf{r}-\mathbf{r_p})\hat{n}(r)\times\hat{\mathbf{\Phi}}_\mathbf{p}(\mathbf{r})$ is used to test both sides of equation (3.15 and 3.16) to yield

$$\begin{aligned}
&\int_S \mathbf{M}(\mathbf{r})\cdot\delta(\mathbf{r}-\mathbf{r_p})\hat{\mathbf{n}}(\mathbf{r})\times\hat{\mathbf{\Phi}}_\mathbf{p}(\mathbf{r})ds \\
= \quad & -\int_S \hat{\mathbf{n}}(\mathbf{r})\times\sum_{n=1}^{N_b} E_n\mathbf{\Phi}_n(\mathbf{r})\cdot\delta(\mathbf{r}-\mathbf{r_p})\hat{\mathbf{n}}(\mathbf{r})\times\hat{\mathbf{\Phi}}_p(\mathbf{r})ds \\
= \quad & -\sum_{n=1}^{N_b} E_n\mathbf{\Phi}_n(\mathbf{r}_p)\cdot\hat{\mathbf{\Phi}}_p(\mathbf{r}_p) \qquad (3.19)
\end{aligned}$$

$$\begin{aligned}
&\int_S \mathbf{J}(\mathbf{r})\cdot\delta(\mathbf{r}-\mathbf{r_p})\hat{\mathbf{n}}(\mathbf{r})\times\hat{\Phi}_p(\mathbf{r})ds \\
= \quad & \int_S \hat{\mathbf{n}}(\mathbf{r})\times\sum_{n=1}^{N_b} H_n\mathbf{\Phi}_n(\mathbf{r})\cdot\delta(\mathbf{r}-\mathbf{r_p})\hat{\mathbf{n}}(\mathbf{r})\times\hat{\mathbf{\Phi}}_\mathbf{p}(\mathbf{r})ds \\
= \quad & \sum_{n=1}^{N_b} H_n\mathbf{\Phi}_n(\mathbf{r}_p)\cdot\hat{\mathbf{\Phi}}_p(\mathbf{r}_p) \qquad (3.20)
\end{aligned}$$

where $\mathbf{r}_p$ is the location of the p_{th} SEM basis function, and $\hat{\mathbf{\Phi}}_\mathbf{p}(\mathbf{r})$ is the unit vector of p_{th} SEM basis function at location $\mathbf{r}$. Using the property of the Delta function and the orthogonal property of the basis functions yields

$$\begin{aligned}
&\mathbf{M}(\mathbf{r_p})\cdot\hat{\mathbf{n}}(\mathbf{r}_p)\times\hat{\mathbf{\Phi}}_p(\mathbf{r}_p) \\
= \quad & -\sum_{n=1}^{N_b} E_n\hat{\mathbf{n}}(\mathbf{r}_p)\times\mathbf{\Phi}_n(\mathbf{r}_p)\cdot\hat{\mathbf{n}}(\mathbf{r}_p)\times\hat{\mathbf{\Phi}}_\mathbf{p}(\mathbf{r}_p) \\
= \quad & -E_p\hat{\mathbf{n}}(\mathbf{r}_p)\times\mathbf{\Phi}_p(\mathbf{r}_p)\cdot\hat{\mathbf{n}}(\mathbf{r}_p)\times\hat{\mathbf{\Phi}}_p(\mathbf{r}_p) = -E_p \qquad (3.21)
\end{aligned}$$

$$
\begin{aligned}
& \mathbf{J}(\mathbf{r_p}) \cdot \hat{\mathbf{n}}(\mathbf{r}_p) \times \hat{\mathbf{\Phi}}_{\mathbf{p}}(\mathbf{r}_p) \\
= & \sum_{n=1}^{N_b} H_n \hat{\mathbf{n}}(\mathbf{r}_p) \times \mathbf{\Phi}_n(\mathbf{r}_p) \cdot \hat{\mathbf{n}}(\mathbf{r}_p) \times \hat{\mathbf{\Phi}}_{\mathbf{p}}(\mathbf{r}_p) \\
= & H_p \hat{\mathbf{n}}(\mathbf{r}_p) \times \mathbf{\Phi}(\mathbf{r}_p) \cdot \hat{\mathbf{n}}(\mathbf{r}_p) \times \hat{\mathbf{\Phi}}_p(\mathbf{r}_p) = H_p
\end{aligned} \tag{3.22}
$$

Then the SEM unknowns E_n and H_n can be expressed by SIM unknowns j_m and m_m, as

$$
E_n = \sum_{m=1}^{N_j} j_m \mathbf{f}_m(\mathbf{r}_n) \cdot \hat{\mathbf{n}}(\mathbf{r}_n) \times \hat{\mathbf{\Phi}}_n(\mathbf{r}_n) = \sum_{m}^{N_j} R_{nm} j_m \tag{3.23}
$$

$$
H_n = \sum_{m=1}^{N_j} m_m \mathbf{f}_m(\mathbf{r}_n) \cdot \hat{\mathbf{n}}(\mathbf{r}_n) \times \hat{\mathbf{\Phi}}_n(\mathbf{r}_n) = -\sum_{m}^{N_j} R_{nm} m_m \tag{3.24}
$$

where $\mathbf{R}$ is an interpolation matrix with

$$
R_{nm} = -\mathbf{f}_m(\mathbf{r}_n) \cdot \hat{\mathbf{n}}(\mathbf{r}_n) \times \hat{\mathbf{\Phi}}_{\mathbf{n}}(\mathbf{r}_n) \tag{3.25}
$$

If $\mathbf{J}$ and $\mathbf{M}$ are chosen as the final unknowns on the surface, the matrix form of the final linear system is

$$
\begin{bmatrix} \mathbf{A}^{ii} & \mathbf{A}^{bi}\mathbf{R} & 0 \\ \mathbf{R}^T\mathbf{A}^{ib} & \mathbf{R}^T\mathbf{A}^{bb}\mathbf{R} & -\mathbf{R}^T\mathbf{G}\mathbf{R} \\ 0 & \mathbf{Z}_b & \mathbf{Z}_a \end{bmatrix} \begin{bmatrix} \tilde{\mathbf{e}^i} \\ \mathbf{M} \\ \mathbf{J} \end{bmatrix} = \begin{bmatrix} \mathbf{S}^i \\ 0 \\ \mathbf{S}^e \end{bmatrix} \tag{3.26}
$$

Then this system matrix can be solved by iterative solver. In this work, the BiCGStab(ℓ) method with a diagonal pre-conditioner is used [26]. In the iterative solver, when the product of a matrix and a vector is needed, the SIM part is accelerated by FFT as discussed in chapter 2.

3.3 Numerical Examples

The first numerical example is a homogeneous dielectric cube with edge length $a = 0.2\lambda_0$, $\epsilon_r = 9$ can be found in [27]. The frequency of the incident plane wave is

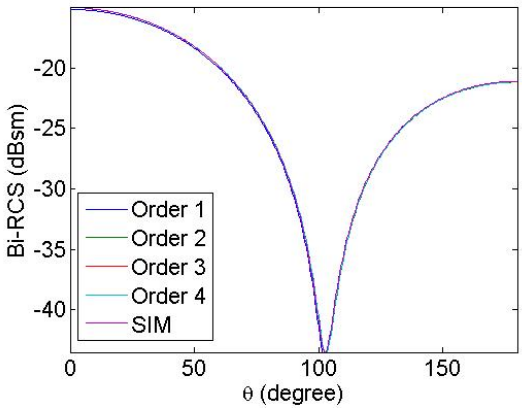

FIGURE 3.2: The Bi-static RCS of a dielectric cube with edge length 0.1 m in $\phi = 0°$ plane at 600 MHz.

600 MHz. The incident plane wave propagating in $\hat{z}$ direction has a polarization of the electric field in $\hat{x}$ direction. The mesh has $5 \times 5 \times 5$ cells in each direction. For the bi-static RCS results obtained from different order of SEM basis functions, in $\phi = 0°$ and $\phi = 90°$ planes are shown in Fig. 3.2 and Fig. 3.3. The SIM-SEM results agree well with the reference results obtained by the SIM.

As shown in Fig. 3.4, the error of the results from second-order SEM basis function is much smaller than the error from first order. For even higher order SEM basis functions the error is similar to the second order, since the error is dominated by the SIM which uses only first order basis functions.

As shown in Fig. 3.5, the x component of the electric field along x direction is no longer piece wise constant. For the first order SEM which is actually FEM, the field component variation along the same direction is very inaccurate. Using of higher order SEM basis function gives more smooth and accurate field distribution along that direction.

The second example is a PEC cube with edge length of 0.755 wavelengths. This example can be found in [27]. The frequency of the incident plane wave is 300 MHz propagating in $\hat{z}$ direction, with polarization in $\hat{x}$ direction. The SIM-SEM mesh has

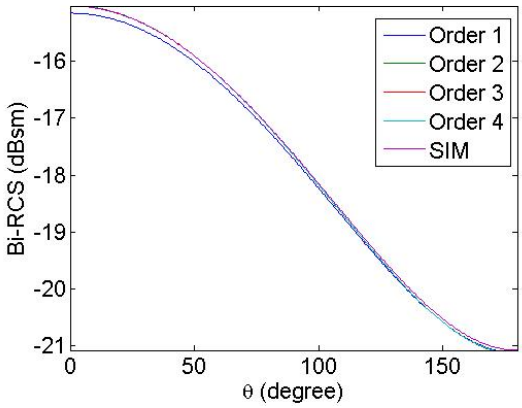

FIGURE 3.3: The Bi-static RCS of a dielectric cube with edge length 0.1 m in $\phi = 90°$ plane at 600 MHz.

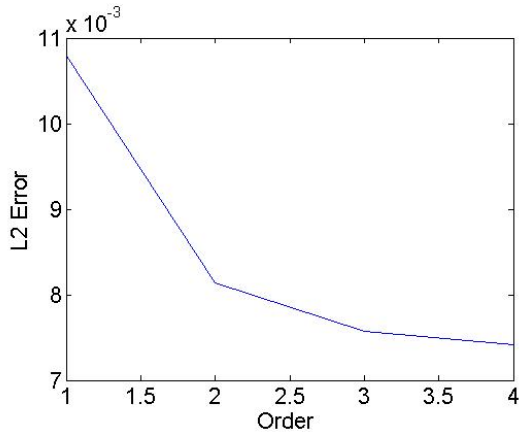

FIGURE 3.4: The error of RCS from a dielectric cube with edge length 0.1 m from different orders of SEM basis function.

$12 \times 12 \times 12$ cells in each direction, where the PEC part includes $10 \times 10 \times 10$ cells in each direction. As shown in Fig. 3.6 and Fig. 3.7, the SIM-SEM results agree well with the reference results [27].

The third case is a PEC sphere with radius $r = 1\,\text{m}$. The frequency of the incident plane wave is 30 MHz. The incident plane wave propagating in $\hat{z}$ direction has a polarization of the electric field in $\hat{x}$ direction. The mesh for the PEC sphere is generated by a mesh generator Cubit and is shown in Fig. 3.8. The bi-static RCS

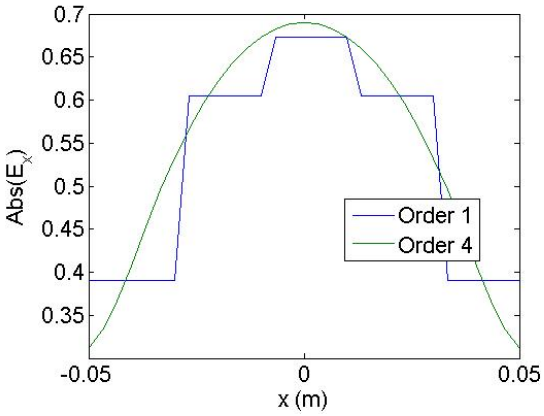

FIGURE 3.5: The x component of electric field a dielectric cube with edge length 0.1 m along x direction at 600 MHz.

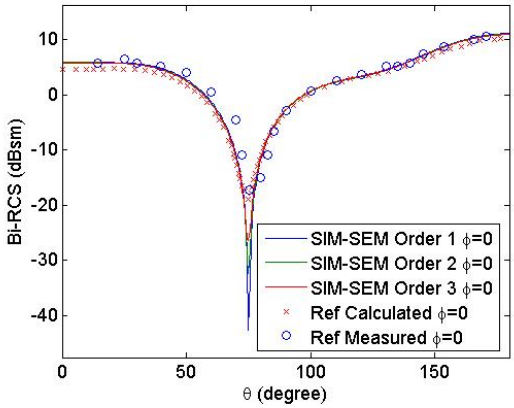

FIGURE 3.6: The Bi-static RCS of a dielectric cube with 0.75 m in $\phi = 0°$ plane at 300 MHz.

in $\phi = 0°$ and $\phi = 90°$ planes are shown in the Fig. 3.9 and Fig. 3.10, respectively. Again the SIM-SEM results for different orders are agree well with analytical results. For this case, a phenomenon is observed that when the order of the SEM basis function is increased or denser mesh is used, the results sometimes become worse. To the best knowledge of the author the reason for this phenomenon is partly because of the mesh generated for this problem can hardly satisfy the 2 requirements at the same time. The 2 requirements are, first the volume mesh should be hexahedron,

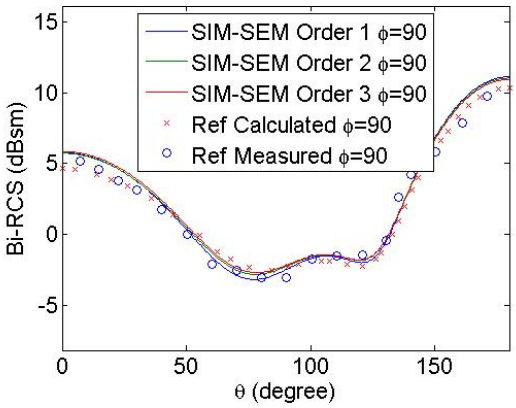

FIGURE 3.7: The Bi-static RCS of a dielectric cube with 0.75 m in $\phi = 90°$ plane at 300 MHz.

and the second, the shape of surface should be cuboid and surface grid should be uniform. And this problem is solved in chapter 6, by utilizing tetrahedron element based FEM for the regions are not easy to model by hexahedron, and non-conforming SIM-SEM scheme via DG method.

The forth case is a dielectric composite body as shown in Fig. 3.11. The thickness

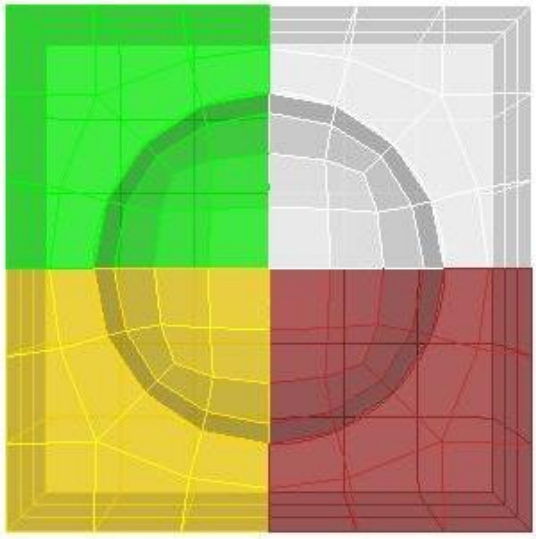

FIGURE 3.8: The mesh for SIM-SEM of a PEC sphere with $r = 1$ m.

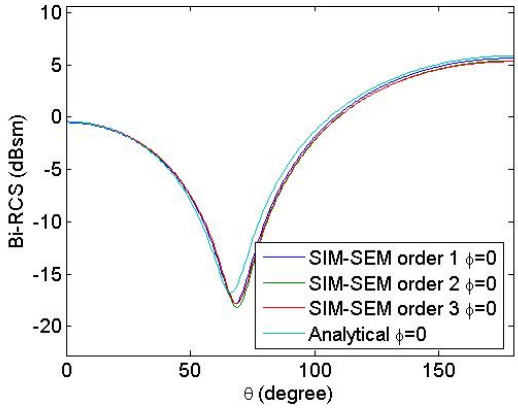

FIGURE 3.9: The Bi-static RCS of a PEC sphere with $r = 1$ m in $\phi = 0°$ plane at 30 MHz.

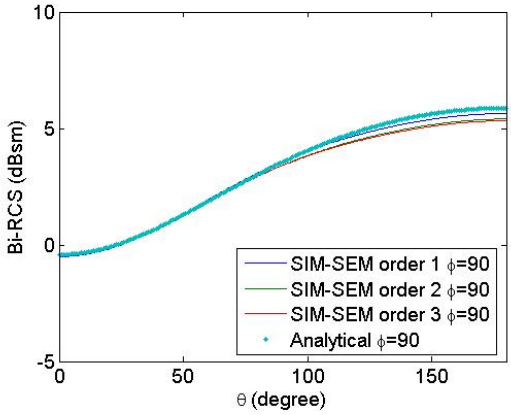

FIGURE 3.10: The Bi-static RCS of a PEC sphere with $r = 1m$ in $\phi = 90°$ plane at 30 MHz.

of the dielectric slab is $d = 0.04$ m, and the plane wave at 400 MHz is incident along the z direction. The bi-static RCS in $\phi = 0°$ and $\phi = 90°$ planes are shown in the Fig. 3.12 and Fig. 3.13, respectively. All results agree very well with the FEM-BI results.

The final example is a PEC-dielectric composite body. The object is a three-layer structure, where the center layer is PEC, and the top and bottom layers are dielectric bodies with different dielectric constants. This example is actually can not

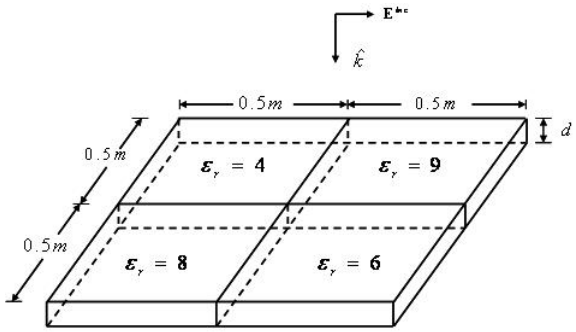

FIGURE 3.11: TThe detailed dimension of a dielectric composite body structure.

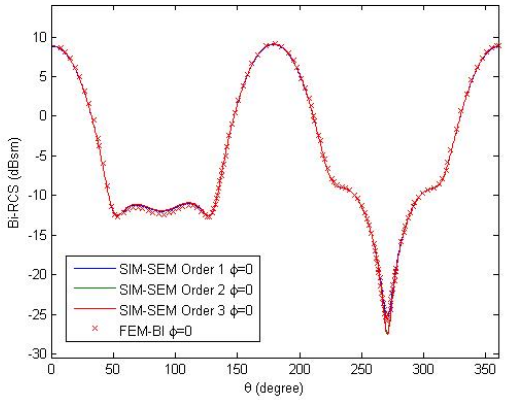

FIGURE 3.12: The Bi-static RCS of a dielectric composite body in $\phi = 0°$ plane at 400 MHz.

be solve by the CG-FFT algorithms because of the existing of the PEC structures. The detailed size and the dielectric constants are shown in Fig. 3.14. The frequency of the incident plane wave is 400 MHz, propagating in $\hat{z}$ direction, with polarization in $\hat{x}$ direction. Results in Fig. 3.15 and Fig. 3.16 agree very well with the ECT [28, 29] results. This problem can also be solved by MOM (FEKO) directly but solving of the problem cost 73G disk space and 15 days.

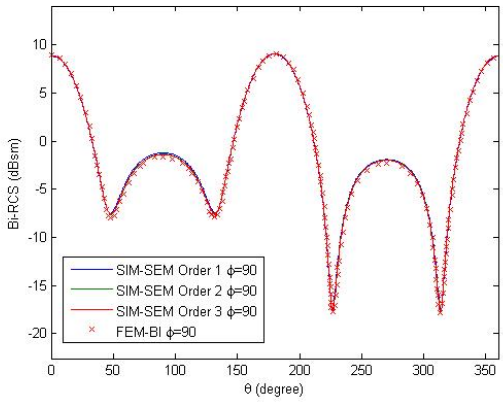

FIGURE 3.13: The Bi-static RCS of a dielectric composite body in $\phi = 90°$ plane at 400 MHz.

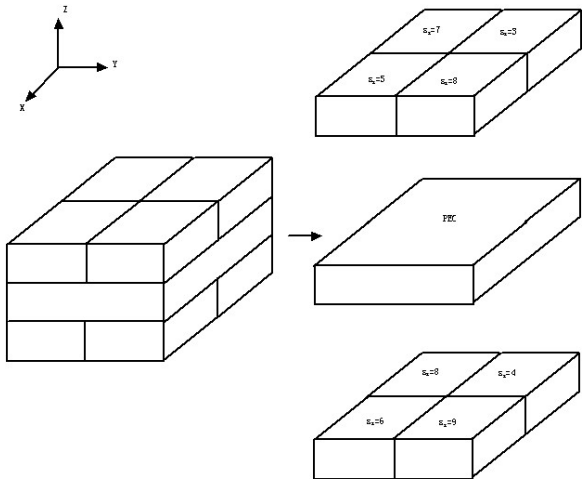

FIGURE 3.14: The detailed dimension of a PEC dielectric composite body.

3.4 Conclusion

In this chapter, we proposed the hybridization of SIM-SEM via an interpolation matrix. The SIM-SEM has advantages of both SIM and SEM. This method can deal with complex property of the targets because the SEM is used to model all the inhomogeneity. On the other hand, PML is not needed in SIM-SEM; instead SIM plays the role of the boundary condition. Because of the merits of SIM mentioned in chapter 2, the computational cost of the boundary integral part has been reduced greatly.

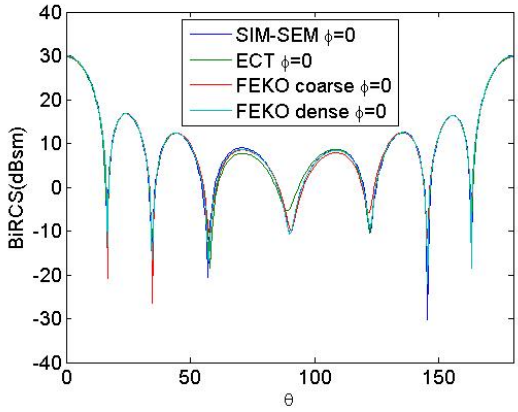

FIGURE 3.15: The Bi-static RCS of a PEC dielectric composite body in $\phi = 0°$ plane at 400 MHz.

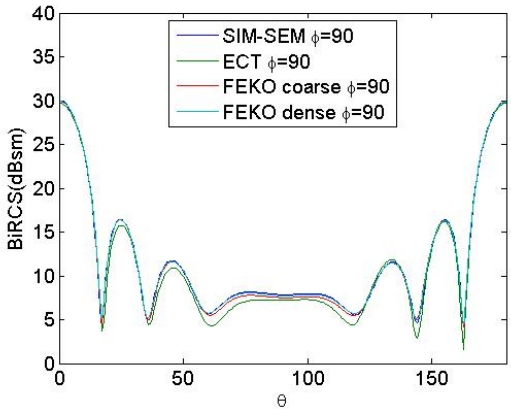

FIGURE 3.16: The Bi-static RCS of a PEC dielectric composite body in $\phi = 90°$ plane at 400 MHz.

Previously, there is not a general 3D boundary integral equation algorithm that also utilizes the fast Fourier transform. And there is no work reported about combining the SEM with boundary integral equation too. In this work, we successfully combine and apply the SIM and SEM for arbitrary 3D problems. The SIM-SEM is very efficient in terms of time and memory compared with the conventional FEM-BI. For a homogeneous dielectric problem, in order to obtain the same accuracy, we found that this method is about 15 times faster than the conventional FEM-BI method.

4

Spectral Element Method - Finite Element Method

4.1 Motivation

The circuit design, electromagnetic compatibility and signal integrity problems require powerful electromagnetic analysis tools. With the development of the integrated circuit, the size of circuit components becomes much smaller, while the size of the whole structure can still be large. These problems, which have both electrically large parts and electrically fine structures, are multi-scale problems. Conventional numerical electromagnetic analysis tools like FEM [30, 27, 11] can be used to solve these problems, because of the robustness of FEM. But for multi-scale problems the number of FEM elements can be very large for two reasons. First, FEM elements must be small enough to accurately construct the geometrical structure; second, a global conformal mesh is required for conventional FEM. The large number of elements results in large linear system which is difficult or sometimes impossible to solve.

Domain decomposition methods have been proposed to solve multi-scale problems. These methods in general first divide the whole problem into several small

problems, then solve every small problem independently, and use a proper boundary condition on the artificial interfaces between sub-domains to ensure that the division of the original problem into several smaller problems does not change the solution.

The first study of domain decomposition for solving Maxwell's equation was done by Després [31]. In Després's work, the Robin's boundary condition is utilized to impose the continuity on the artificial boundaries. Jinfa Lee used Fourier analysis to prove the convergence of the domain decomposition via Robin's boundary condition [32], and applied the domain decomposition based on FEM and Robin's boundary condition to finite periodic structures such as antenna array and photonic crystal problems [32, 33]. Because this algorithm utilizes the Robin's boundary condition, theoretically they can handle non-conforming elements. However, to the best of author's knowledge, there are no detailed numerical results and discussions which have shown the ability of this category of algorithms to solve non-conforming problems. Furthermore, all studies mentioned above are based on the conventional FEM defined in tetrahedron elements. But as shown in [25], for electrically large and smooth structures, the hexahedron based spectral element method has higher efficiency and accuracy than the conventional tetrahedron based FEM. As such, it is logical to extend the domain decomposition method with the combination of FEM and SEM for multi-scale problems.

The proposed SEM-FEM domain decomposition algorithm can efficiently handle problems with multi-scale structures, by using FEM to model electrically small sub-domains and using SEM to model electrically large and smooth sub-domains. This combination can reduce the total number of elements used in solving multi-scale problems, thus it is more efficient than conventional FEM or conventional FEM domain decomposition method. Another merit of the proposed method is that it is capable of handling arbitrary non-conforming elements, including non-conforming tetrahedron-tetrahedron elements, hexahedron-hexahedron elements and tetrahedron-hexahedron

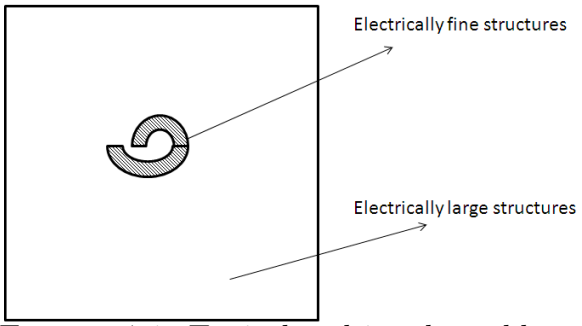

FIGURE 4.1: Typical multi-scale problems

elements. Because of the Robin's boundary condition, there is no conforming requirement for elements on sub-domain interfaces. Both geometry modeling and mesh generation are totally independent for different sub-domains, thus the geometry modeling and mesh generation for the proposed SEM-FEM domain decomposition method are highly flexible.

In this section we focus on problems with multi-scale structures. A multi-scale problem usually contains both electrically large, smooth parts and electrically fine detail structures. A typical multi-scale problem is shown in Fig. 4.1.

4.2 Formulation

If conventional FEM is used to solve a multi-scale problem, the vector Helmholtz equation for electric field

$$\nabla \times \frac{1}{\mu_r} \nabla \times \mathbf{E} - k_0^2 \epsilon_r \mathbf{E} = -j\omega\mu_0 \mathbf{J}^{imp} \tag{4.1}$$

together with boundary conditions

$$\begin{aligned} &\mathbf{E}^t = 0 \quad \text{on PEC} \\ &(\frac{1}{\mu_r} \nabla \times \mathbf{E})^t = 0 \quad \text{on PMC} \\ &\mathbf{E}^t - (\frac{1}{\mu_r} \nabla \times \mathbf{E})^t = 0 \quad \text{on infinity surface} \end{aligned} \tag{4.2}$$

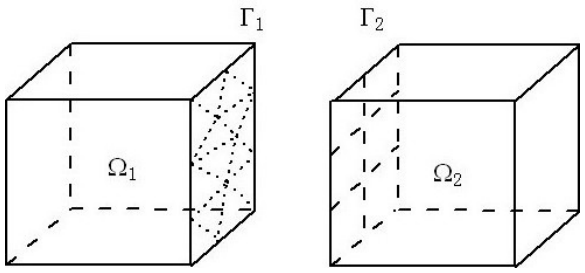

FIGURE 4.2: Illustration of domain decomposition of SEM-FEM with two sub-domains

need to be solved. Where the superscript t denotes the tangential component of a vector.

On the other hand, the idea of the proposed domain decomposition method is first dividing the computational domain into several different sub-domains, then the SEM based on hexahedron elements is used for electrically large and smooth sub-domains, and the FEM based on tetrahedron elements is used for electrically fine structures. Let's consider the simplest case first, where the whole problem is divided into two sub-domains as shown in Fig. 4.2. Because there is an artificial interface inserted into the computational domain, additional boundary conditions are required to guarantee continuity of the tangential electric field and magnetic field on artificial boundaries. The Robin's boundary condition [32] is used. For this case, the Robin's boundary condition can be expressed as

$$\hat{\mathbf{n}} \times \frac{1}{\mu_{r,1}} \nabla \times \mathbf{e}_1^b - jk\mathbf{e}_1^b = -\hat{\mathbf{n}} \times \frac{1}{\mu_{r,2}} \nabla \times \mathbf{e}_2^b - jk\mathbf{e}_1^b \tag{4.3}$$

which actually imposes the continuity on the artificial interface. Where $\mathbf{e}_i^b$ denotes the boundary electric field in i_{th} sub-domain, and $\hat{\mathbf{n}}$ denotes the unit vector of outer normal direction of corresponding sub-domain. In the domain decomposition frame

work, electric field in sub-domain 1 satisfies following equations

$$\begin{aligned}
&\nabla \times \frac{1}{\mu_{r,1}} \nabla \times \mathbf{E}_1 - k_0^2 \epsilon_{r,1} \mathbf{E}_1 = -j\omega\mu_0 \mathbf{J}_1^{imp} \\
&\mathbf{E}_1^t = 0 \quad \text{on PEC} \\
&(\frac{1}{\mu_{r,1}} \nabla \times \mathbf{E}_1)^t = 0 \quad \text{on PMC} \\
&\mathbf{E}_1^t - (\frac{1}{\mu_{r,1}} \nabla \times \mathbf{E}_1)^t = 0 \quad \text{on infinity surface} \\
&\hat{\mathbf{n}} \times \frac{1}{\mu_{r,1}} \nabla \times \mathbf{e}_1^b - jk\mathbf{e}_1^b = -\hat{\mathbf{n}} \times \frac{1}{\mu_{r,2}} \nabla \times \mathbf{e}_2^b - jk\mathbf{e}_2^b
\end{aligned} \tag{4.4}$$

where e_1^b denotes the electric field on the interface of sub-domain 1.

Similarly, electric field in sub-domain 2 satisfies following equations

$$\begin{aligned}
&\nabla \times \frac{1}{\mu_{r,2}} \nabla \times \mathbf{E}_2 - k_0^2 \epsilon_{r,2} \mathbf{E}_2 = -j\omega\mu_0 \mathbf{J}_2^{imp} \\
&\mathbf{E}_2^t = 0 \quad \text{on PEC} \\
&(\frac{1}{\mu_{r,2}} \nabla \times \mathbf{E}_2)^t = 0 \quad \text{on PMC} \\
&\mathbf{E}_2^t - (\frac{1}{\mu_{r,2}} \nabla \times \mathbf{E}_2)^t = 0 \quad \text{on infinity surface} \\
&\hat{\mathbf{n}} \times \frac{1}{\mu_{r,2}} \nabla \times \mathbf{e}_2^b - jk_0\mathbf{e}_2^b = -\hat{\mathbf{n}} \times \frac{1}{\mu_{r,1}} \nabla \times \mathbf{e}_1^b - jk_0\mathbf{e}_1^b
\end{aligned} \tag{4.5}$$

The first equations in equation (4.4 and 4.5) are vector Helmholtz equation for electric field in sub-domain 1 and sub-domain 2, respectively. The weak form of those two equations can be expressed as

$$\int \mathbf{\Phi} \cdot [\nabla \times \frac{1}{\mu_{r,p}} \nabla \times \mathbf{E}_p - k_0^2 \epsilon_{r,p} \mathbf{E}_p] ds = -j\omega\mu_0 \int \mathbf{\Phi} \cdot \mathbf{J}_p^{imp} ds \tag{4.6}$$

where p denotes the index of sub-domain.

For FEM sub-domain, the constant tangential linear normal (CT-LN) curl conforming basis function is used to expand the electric field. The definition of the CT-LN curl conforming basis function is

$$\mathbf{\Phi}_n = w_n(L_i \nabla L_j - L_j \nabla L_i) \tag{4.7}$$

where(L_1, L_2, L_3, L_4) are simplex coordinates and w_n denotes the length of edge. The electric field can be expanded by FEM basis functions

$$\mathbf{E}(\mathbf{r}) = \sum_{j=1}^{N^{(e)}} E_j \mathbf{\Phi}_j(\mathbf{r}) \tag{4.8}$$

where $N^{(e)}$ is the number of edges in one tetrahedron, and E_j are the expansion coefficients. The CT-LN FEM basis functions are defined in the physical domain.

For SEM sub-domain, the mixed-order curl conforming Gauss-Lobatto-Legendre (GLL) basis function is used to expand the electric field. The mixed-order curl conforming GLL basis functions are defined in a reference cube $\xi \in [-1,1], \eta \in [-1,1], \zeta \in [-1,1]$ as

$$\begin{aligned}
\mathbf{\Phi}^{\xi}_{rst} &= \hat{\xi}\phi_r^{(N_\xi - 1)}(\xi)\phi_s^{(N_\eta)}(\eta)\phi_t^{(N_\zeta)}(\zeta) \\
\mathbf{\Phi}^{\eta}_{rst} &= \hat{\eta}\phi_r^{(N_\xi)}(\xi)\phi_s^{(N_\eta - 1)}(\eta)\phi_t^{(N_\zeta)}(\zeta) \\
\mathbf{\Phi}^{\zeta}_{rst} &= \hat{\zeta}\phi_r^{(N_\xi)}(\xi)\phi_s^{(N_\eta)}(\eta)\phi_t^{(N_\zeta - 1)}(\zeta)
\end{aligned} \tag{4.9}$$

where N_ξ, N_η, N_ζ are interpolation orders of the vector GLL basis function in $\hat{\xi}, \hat{\eta}, \hat{\zeta}$ directions respectively, and $\mathbf{\Phi}^{\xi}_{rst}, \mathbf{\Phi}^{\eta}_{rst}, \mathbf{\Phi}^{\zeta}_{rst}$ are the vector GLL basis functions in $\hat{\xi}, \hat{\eta}, \hat{\zeta}$ directions, respectively. Then an arbitrary $\mathbf{E}$ vector can be expressed by summation of vector GLL basis functions. If $\mathbf{E}$ field is chosen as the unknown, it

can be expressed in a reference cubic element as:

$$\begin{aligned}\tilde{\mathbf{E}}(\xi,\eta,\zeta) &= \sum_{r=0}^{N_\xi-1}\sum_{s=0}^{N_\eta}\sum_{t=0}^{N_\zeta} E^{\xi}(\xi_r,\eta_s,\zeta_t)\mathbf{\Phi}^{\xi}_{rst} \\ &+ \sum_{r=0}^{N_\xi}\sum_{s=0}^{N_\eta-1}\sum_{t=0}^{N_\zeta} E^{\eta}(\xi_r,\eta_s,\zeta_t)\mathbf{\Phi}^{\eta}_{rst} \\ &+ \sum_{r=0}^{N_\xi}\sum_{s=0}^{N_\eta}\sum_{t=0}^{N_\zeta-1} E^{\zeta}(\xi_r,\eta_s,\zeta_t)\mathbf{\Phi}^{\zeta}_{rst} \\ &= \sum_{j=1}^{N^{(e)}} E_j\mathbf{\Phi}_j(\xi,\eta,\zeta) \end{aligned} \tag{4.10}$$

where $N^{(e)} = N_\xi(N_\eta+1)(N_\zeta+1) + (N_\xi+1)N_\eta(N_\zeta+1) + (N_\xi+1)(N_\eta+1)N_\zeta$ is the number of basis functions in a single hexahedron element, $j=(r,s,t)$ is a compound index, and $\{E_j\}$ are the expansion coefficients, and the tilde denotes that the SEM basis functions are defined in the reference domain and need to be transferred into the physical domain by a covariant transformation [27]

$$\mathbf{E}(x,y,z) = \mathbf{J}_g^{-1}\tilde{\mathbf{E}}(\xi,\eta,\zeta) \tag{4.11}$$

where $\mathbf{J}_g$ is the Jacobian matrix for the geometry mapping from a hexahedron to reference cube.

For the Robin's boundary condition (last equation in equation(4.4 and 4.5)), if we define

$$\mathbf{J}_p = \hat{\mathbf{n}} \times \frac{1}{\mu_{r,p}}\nabla \times \mathbf{E}_p^b \tag{4.12}$$

as the auxiliary current density on the interfaces between two sub-domains, a divergence conforming basis function can be used to discretize the auxiliary current density. For FEM sub-domain, mesh on the interface is triangle. The CN-LT basis

function defined on triangle is use to expand auxiliary current. The definition of CN-LT basis function is

$$\mathbf{f} = \hat{\mathbf{n}} \times w_n(L_i \nabla L_j - L_j \nabla L_i) \tag{4.13}$$

where(L_1, L_2, L_3) are simplex coordinates and w_n denotes the length of an edge. The auxiliary current can be expanded as

$$\mathbf{J}(\mathbf{r}) = \sum_{m=1}^{N^{(e)}} J_m \mathbf{f}_m(\mathbf{r}) \tag{4.14}$$

where $N^{(e)}$ is the number of edges in 1 triangle, and J_m is the expanding coefficients. The constant normal linear tangential (CN-LT) basis function is defined in the physical domain.

For SEM sub-domain, mesh on the interface is rectangular. Using mixed-order divergence conforming basis functions defined on a reference square $\xi \in [-1, 1], \eta \in [-1, 1]$

$$\begin{aligned} \mathbf{f}^{\xi}_{rs} &= \hat{\mathbf{n}} \times \hat{\xi} \phi_r^{(N_\xi - 1)}(\xi) \phi_s^{(N_\eta)}(\eta) \\ \mathbf{f}^{\eta}_{rs} &= \hat{\mathbf{n}} \times \hat{\eta} \phi_r^{(N_\xi)}(\xi) \phi_s^{(N_\eta - 1)}(\eta) \end{aligned} \tag{4.15}$$

the auxiliary current can be expanded as

$$\begin{aligned} \tilde{\mathbf{J}}(\xi, \eta) &= \sum_{r=0}^{N_\xi} \sum_{s=0}^{N_\eta - 1} J^{\xi}(r, s) \mathbf{f}^{\xi}_{rs}(\xi, \eta) + \sum_{r=0}^{N_\xi - 1} \sum_{s=0}^{N_\eta} J^{\eta}(r, s) \mathbf{f}^{\eta}_{rs}(\xi, \eta) \\ &= \sum_{m=1}^{N^{(e)}} J_m \mathbf{f}_m(\xi, \eta) \end{aligned} \tag{4.16}$$

where the tilde denotes a vector defined in the reference domain, $N^{(e)} = N_\xi(N_\eta + 1) + (N_\xi + 1)N_\eta$ is the number of basis functions in a single rectangle element, $m = (r, s)$ is a compound index, and $\{J_m\}$ are the expansion coefficients. The

mixed-order divergence conforming basis function is defined in the reference domain. A transformation from reference domain to the physical domain by a contravariant transformation is needed [27].

$$\mathbf{J}(x,y,z) = \frac{1}{Q}\mathbf{J}_g^T\tilde{\mathbf{J}}(\xi,\eta) \tag{4.17}$$

where $\mathbf{J}_g$ is a 2×3 Jacobian matrix for the geometry mapping from a trapezoid to a reference square, and Q is defined as

$$Q = \left[(\frac{\partial y}{\partial \eta}\frac{\partial z}{\partial \xi} - \frac{\partial z}{\partial \eta}\frac{\partial y}{\partial \xi})^2 + (\frac{\partial z}{\partial \eta}\frac{\partial x}{\partial \xi} - \frac{\partial x}{\partial \eta}\frac{\partial z}{\partial \xi})^2 + (\frac{\partial x}{\partial \eta}\frac{\partial y}{\partial \xi} - \frac{\partial y}{\partial \eta}\frac{\partial x}{\partial \xi})^2\right]^{\frac{1}{2}} \tag{4.18}$$

So for this two sub-domains case, the system matrix can be expressed in a matrix form

$$\begin{bmatrix} A_1 & C_1 & 0 & 0 & 0 & 0 \\ C_1^t & B_1 & D_1 & 0 & 0 & 0 \\ 0 & D_1^t & \frac{jT_1}{k_0} & 0 & -D_{12}^t & \frac{jT_{12}}{k_0} \\ 0 & 0 & 0 & A_2 & C_2 & 0 \\ 0 & 0 & 0 & C_2^t & B_2 & D_2 \\ 0 & -D_{21}^t & \frac{jT_{21}}{k_0} & 0 & D_2^t & \frac{jT_2}{k_0} \end{bmatrix} \begin{bmatrix} e_1^i \\ e_1^b \\ J_1 \\ e_2^i \\ e_2^b \\ J_2 \end{bmatrix} = \begin{bmatrix} \mathbf{y}_1^i \\ \mathbf{y}_1^b \\ 0 \\ \mathbf{y}_2^i \\ y_2^b \\ 0 \end{bmatrix} \tag{4.19}$$

where

$$A_{p,mn} = \int \left[\frac{1}{\mu_{r,p}}\nabla\times\mathbf{\Phi}_{p,m}^i\cdot\nabla\times\mathbf{\Phi}_{p,n}^i - k_0^2\epsilon_{r,p}\mathbf{\Phi}_{p,m}^i\cdot\mathbf{\Phi}_{p,n}^i\right]dv \tag{4.20}$$

$$B_{p,mn} = \int \left[\frac{1}{\mu_{r,p}}\nabla\times\mathbf{\Phi}_{p,m}^b\cdot\nabla\times\mathbf{\Phi}_{p,n}^b - k_0^2\epsilon_{r,p}\mathbf{\Phi}_{p,m}^b\cdot\mathbf{\Phi}_{p,n}^b\right]dv \tag{4.21}$$

$$C_{p,mn} = \int \left[\frac{1}{\mu_{r,p}}\nabla\times\mathbf{\Phi}_{p,m}^i\cdot\nabla\times\mathbf{\Phi}_{p,n}^b - k_0^2\epsilon_{r,p}\mathbf{\Phi}_{p,m}^i\cdot\mathbf{\Phi}_{p,n}^b\right]dv \tag{4.22}$$

$$C_{p,mn}^t = \int \left[\frac{1}{\mu_{r,p}}\nabla\times\mathbf{\Phi}_{p,m}^b\cdot\nabla\times\mathbf{\Phi}_{p,n}^i - k_0^2\epsilon_{r,p}\mathbf{\Phi}_{p,m}^b\cdot\mathbf{\Phi}_{p,n}^i\right]dv \tag{4.23}$$

$$D_{p,mn} = \int \mathbf{\Phi}^b_{p,m} \cdot \mathbf{f}_{p,n} ds \tag{4.24}$$

$$D^t_{p,mn} = \int \mathbf{f}_{p,m} \cdot \mathbf{\Phi}^b_{p,n} ds \tag{4.25}$$

$$D^t_{pq,mn} = \int \mathbf{f}_{p,m} \cdot \mathbf{\Phi}^b_{q,n} ds \tag{4.26}$$

$$T_{p,mn} = \int \mathbf{f}_{p,m} \cdot \mathbf{f}_{p,n} ds \tag{4.27}$$

$$T_{pq,mn} = \int \mathbf{f}_{p,m} \cdot \mathbf{f}_{q,n} ds \tag{4.28}$$

$$y^i_p = -j\omega\mu_0 \int \mathbf{\Phi}^i_{p,m} \cdot \mathbf{J}^{imp} dv \tag{4.29}$$

$$y^b_p = -j\omega\mu_0 \int \mathbf{\Phi}^b_{p,m} \cdot \mathbf{J}^{imp} dv \tag{4.30}$$

where superscript i denotes the interior, and superscript b denotes boundary, e^i_p denotes the interior electric field in sub-domain p, e^b_p denotes the boundary electric field in sub-domain p, J_p denotes the auxiliary current on the interface of sub-domain p, y denotes the source term, J^{imp} denotes the internal imposed electric current source.

Up to here, the sub-domains are still coupled together. The next step is to use a stationary point iterative solver to solve the system. For the $(k+1)$th step, realizing that solutions for each sub-domain at the k_{th} step are already known, the update equation for sub-domain 1 can be expressed as

$$\begin{bmatrix} A_1 & C_1 & 0 \\ C_1^T & B_1 & D_1 \\ 0 & D_1^T & \frac{j}{k_0} T_1 \end{bmatrix} \begin{bmatrix} e^i_{1,k+1} \\ e^b_{1,k+1} \\ J_{1,k+1} \end{bmatrix} = \begin{bmatrix} y^i_1 \\ y^b_1 \\ 0 \end{bmatrix} + \begin{bmatrix} 0 & 0 & 0 \\ 0 & 0 & 0 \\ 0 & D^T_{2,1} & -\frac{j}{k_0} T_{2,1} \end{bmatrix} \begin{bmatrix} e^i_{2,k} \\ e^b_{2,k} \\ J_{2,k} \end{bmatrix} \tag{4.31}$$

similar for sub-domain 2,

$$\begin{bmatrix} A_2 & C_2 & 0 \\ C_2^T & B_2 & D_2 \\ 0 & D_2^T & \frac{j}{k_0}T_2 \end{bmatrix} \begin{bmatrix} e^i_{2,k+1} \\ e^b_{2,k+1} \\ J_{2,k+1} \end{bmatrix} = \begin{bmatrix} y^i_2 \\ y^b_2 \\ 0 \end{bmatrix} + \begin{bmatrix} 0 & 0 & 0 \\ 0 & 0 & 0 \\ 0 & D^T_{1,2} & -\frac{j}{k_0}T_{1,2} \end{bmatrix} \begin{bmatrix} e^i_{1,k} \\ e^b_{1,k} \\ J_{1,k} \end{bmatrix} \quad (4.32)$$

It is clear from the two equations above that at the $(k+1)_{th}$ step the solution of one sub-domain is only related to the solution of all sub-domains at the k_{th} step, so the two sub-domains are decoupled. The above formulas can be easily extended to problems with n sub-domains. Then for ith sub-domain, the update equation can be expressed as

$$\begin{bmatrix} A_i & C_i & 0 \\ C_i^T & B_i & D_i \\ 0 & D_i^T & \frac{j}{k_0}T_i \end{bmatrix} \begin{bmatrix} e^i_{i,k+1} \\ e^b_{i,k+1} \\ J_{i,k+1} \end{bmatrix} = \begin{bmatrix} y^i_i \\ y^b_i \\ 0 \end{bmatrix}$$

$$+ \sum_{j \neq i}^{j \in neig(i)} \begin{bmatrix} 0 & 0 & 0 \\ 0 & 0 & 0 \\ 0 & D^T_{i,j} & -\frac{j}{k_0}T_{i,j} \end{bmatrix} \begin{bmatrix} e^i_{j,k} \\ e^b_{j,k} \\ J_{j,k} \end{bmatrix} \quad (4.33)$$

After obtaining the above equation, the solving process can be done in two steps. The first step is the LU factorization for every sub-domain. The second step is carrying a loop for each sub-domain. In the loop, we first update the RHS term for current sub-domain using the solution obtained in last step, and then solve for current sub-domain using the LU factorization and update the solution for current sub-domain. When the residue is smaller than a prescribed tolerance, the program can be terminated.

4.3 Numerical Examples

The first validation case is a cavity case. There is a cubic PMC cavity with a edge length $a_1 = 1$ m filled with dielectric cube with edge length $a_2 = 0.5$ m with $\epsilon_r = 9$ at center part. The dielectric cube is discretized by tetrahedron, and the other part

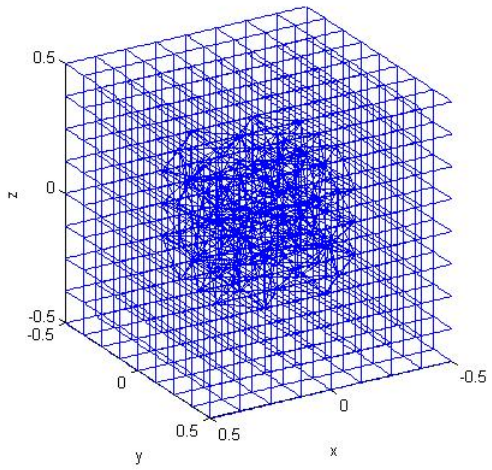

FIGURE 4.3: Spatial discretization in SEM-FEM of the dielectric filled PMC cavity case

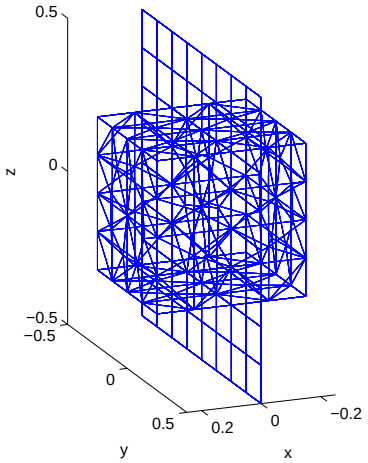

FIGURE 4.4: Edges on the interface between sub-domains of the dielectric filled PMC cavity case

is discretized by hexahedron. The spatial discretization is show in Fig.4.3. In order to test all three types of non-conforming meshes, all regions is cutted through $x = 0$ plane, then there are two tetrahedron sub-domains, two hexahedron sub-domains, and all three types of interfaces. The edges located on the interfaces between sub-domains are shown in Fig.4.4.

There is an imposed electric current source $\mathbf{J}^{imp}$ located on the edge from point

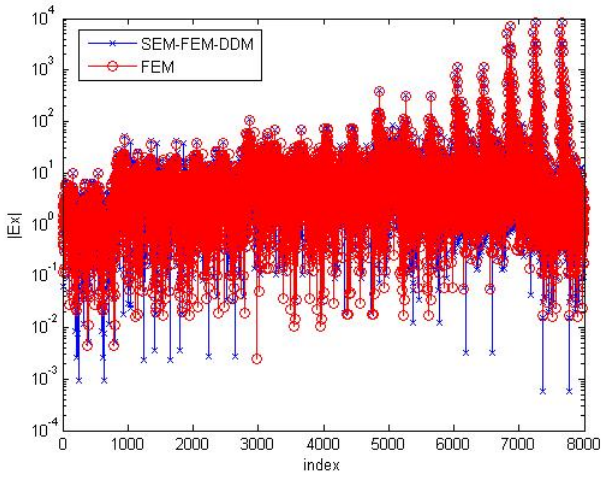

FIGURE 4.5: Result comparison between FEM and SEM-FEM-DDM the dielectric filled PMC cavity case

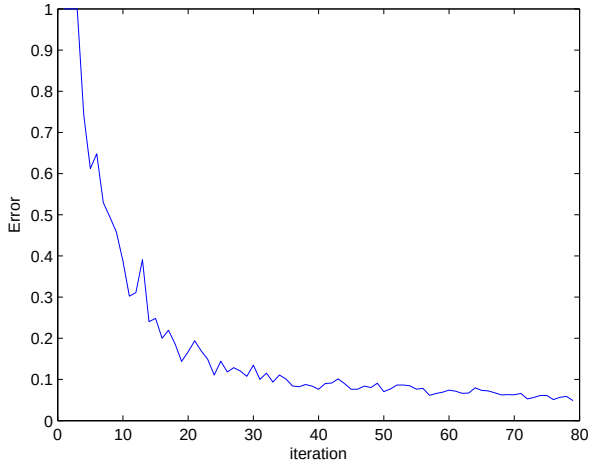

FIGURE 4.6: Error convergence in SEM-FEM-DDM the dielectric filled PMC cavity case

$(0.05, -0.375, 0.05)$ to point $(0.05, -0.375, 0.05)$, and the working frequency is 200 MHz. The electric field at 8000 uniformly distributed point inside the cavity is calculated, and the conventional FEM solution is used as reference as shown in Fig. 4.5. The convergence curve in the stationary point solver is shown in Fig. 4.6. And

the total L_2 error is defined as

$$L_2 = \frac{|E - E_{ref}|_2}{|E_{ref}|_2} \tag{4.34}$$

the L_2 error is 4.85% when the tolerance is equal to 0.05.

Then we will solve a real multi-scale problem. This problem includes a fine spiral structure and large homogeneous free space. The spiral is composed by 3 semicircles with radius $R_1 = 0.14$ m, $R_2 = 0.16$ m, and $R_3 = 0.18$ m, respectively, as shown in Fig. 4.7. The thickness of the spiral structure is 0.02 m. The spiral structure is made of dielectric with $\epsilon_r = 9$. And the spiral structure is placed in a cube cavity with edge length of 1.5 m. There is a imposed electric current source located on the edge from $(0.0, 0.16, -0.01)$ to $(0.0, 0.18, 0.01)$, the working frequency is 166 MHz. Conventional FEM and SEM-FEM DDM are used to solve the filed problem in the cavity. The electric field at 8000 uniformly distributed point inside the cavity is calculate, and conventional FEM solution is used as reference. The mesh for conventional FEM is shown in Fig. 4.8. The mesh for SEM-FEM is shown in Fig. 4.9. The electric field in the cavity is shown in the Fig. 4.10.

The L_2 error is 3.41% when the 2 order SEM basis function is used and the tolerance is set to be 0.01.

The CPU time costs by using FEM and SEM-FEM are shown in Table. 4.1. The preprocessing time includes the time for assembling and LU decomposition of the system matrix. Solving time is the time for the Gauss-Seidel iteration. Post processing time is the time for field interpolation.

And the peak memory costs in FEM and SEM-FEM (2 order SEM basis function) are 1.1 G byte and 240 M byte, respectively. According to the CPU time and memory cost for SEM-FEM, it is clear that the SEM-FEM is more efficient than conventional FEM for multi-scale problems.

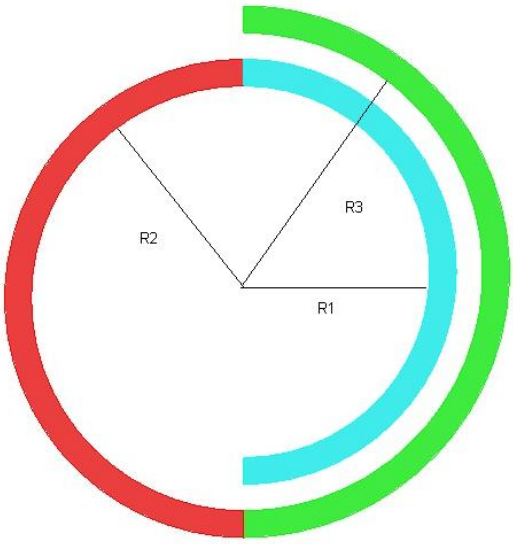

FIGURE 4.7: Detailed dimension of the spiral structure

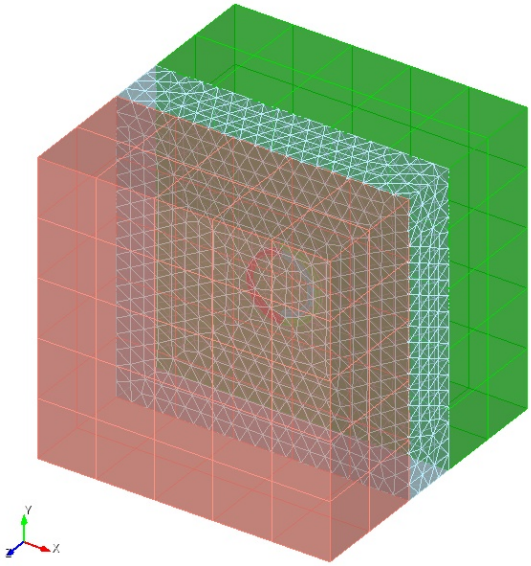

FIGURE 4.8: Mesh of the spiral structure used in SEM-FEM-DDM

4.4 Conclusion

In this chapter, we studied the SEM-FEM DDM via Robin's boundary condition. This method combines hexahedron based SEM and tetrahedron based FEM. The Robin's boundary condition is used to impose continuity on interfaces between sub-

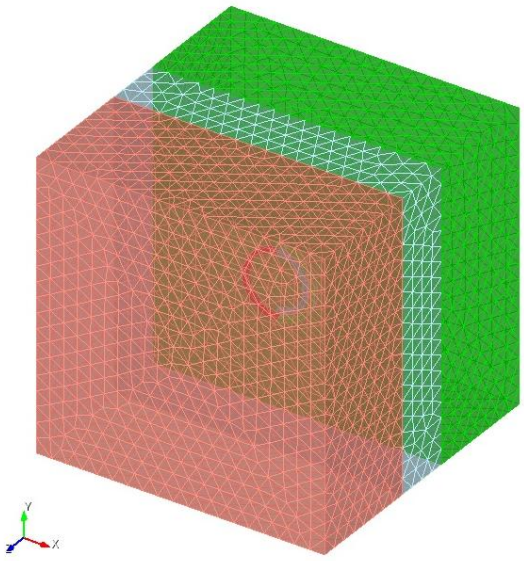

FIGURE 4.9: Mesh of the spiral structure used in FEM

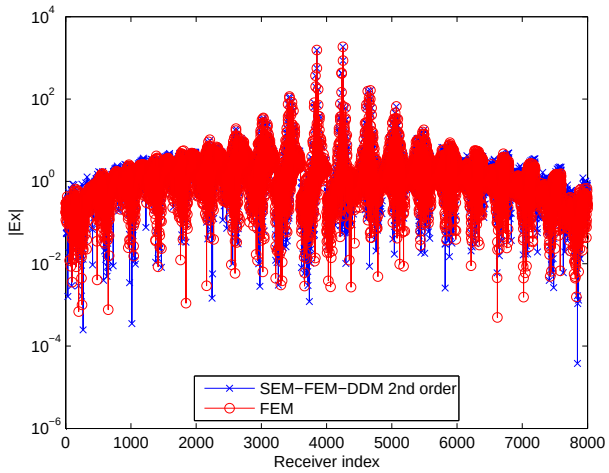

FIGURE 4.10: Result comparison between FEM and SEM-FEM-DDM of the spiral structure

domains, thus it is possible to use arbitrary non-conforming element in different sub-domains. As a result, the number of elements in SEM-FEM DDM for multi-scale problems is much less than the number of elements in conventional FEM. Therefore SEM-FEM DDM is more efficient than conventional FEM.

Table 4.1: CPU time comparison for FEM and SEM-FEM for a spiral structure inside a PMC cube

CPU time (s)	Pre-processing	Solving	Post-processing
FEM	1199	85	160
SEM-FEM (order 1)	98	10	42
SEM-FEM (order 2)	94	35	41

5

FEM-SEM-DDM for Interconnect Applications

5.1 Motivation

In the last chapter, a non-conforming domain decomposition algorithm based on SEM and FEM via Robin's boundary condition is studied. It shows advantages over conventional FEM for solving multi-scale problems, and can be applied to interconnect structures. The proposed method is especially efficient for modeling of interconnect structures together with large structures. In this chapter, the application of the DDM algorithm in interconnect problems is discussed. The proposed DDM algorithm is applied to interconnect problems. The scattering parameter is extracted by the proposed DDM algorithm for some printed circuit examples. The DDM algorithm in this chapter is applied by discontinuous Galerkin via Riemann solver which is different from the Robin's boundary condition used in last chapter. And PML is used as the absorbing boundary conditions in this chapter.

As discussed in last chapter, domain decomposition methods [31] generally divide the whole problem into several smaller sub-domains, solve these smaller problems independently, and then use proper boundary conditions on the interfaces between

sub-domains to ensure that the division of the original problem into several smaller problems does not change the solution. So far, the boundary conditions applied in DDM include ABC's [34], alternating Schwarz method [35, 36, 37] , Dirichlet type boundary condition and Robin's boundary conditions [32, 33]. In this and latter chapters, a discontinuous Galerkin method [38] with the Riemann solver is used as the boundary condition. A better convergence rate in the fixed point iterative solver (Gauss-Seidel) is achieved than using Robin's boundary condition.

In this chapter, the detailed formulation of SEM-FEM DDM via discontinuous Galerkin and the implementation of lumped element in FEM are discussed. Then some numerical results are given to show that SEM-FEM DDM is more efficient than conventional FD [39, 40, 41] or FEM for solving interconnect problems.

5.2 Formulation

5.2.1 DDM via the Discontinuous Galerkin Method

If conventional FEM is used to solve a multi-scale problem, the vector Helmholtz equation for electric field

$$\nabla \times \frac{1}{\mu_r} \nabla \times \mathbf{E} - k_0^2 \epsilon_r \mathbf{E} = -j\omega\mu_0 \mathbf{J}^{imp} \tag{5.1}$$

together with boundary conditions

$$\begin{aligned} &\mathbf{E}^t = 0 \quad \text{on PEC} \\ &(\frac{1}{\mu_r} \nabla \times \mathbf{E})^t = 0 \quad \text{on PMC} \\ &\mathbf{E}^t - (\frac{1}{\mu_r} \nabla \times \mathbf{E})^t = 0 \quad \text{on infinity surface} \end{aligned} \tag{5.2}$$

need to be solved. Where the superscript t denotes the tangential component of a vector.

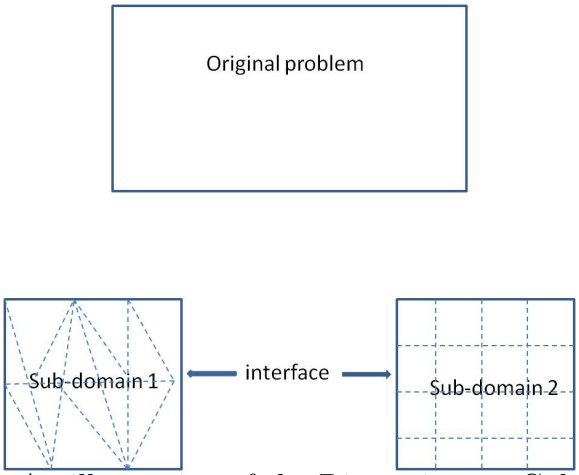

FIGURE 5.1: An illustration of the Discontinuous Galerkin method

In DG scheme, the entire object is divided into several smaller sub-domains, as shown in Fig. 5.1. The original problem is divided into 2 sub-domains, sub-domain 1 is further discretized by tetrahedron element, and sub-domain 2 is discretized by hexahedron. Every sub-domain still satisfies equation (5.1). A testing function $\mathbf{T}$ is used to apply Galerkin procedure on every sub-domain.

$$\int_{v_i} \mathbf{T} \cdot [\nabla \times \frac{1}{\mu_r} \nabla \times \mathbf{E} - k_0^2 \epsilon_r \mathbf{E}] dv = -j\omega\mu_0 \int_{v_i} \mathbf{T} \cdot \mathbf{J}^{imp} dv \tag{5.3}$$

Using integration by part, the equation (5.3) will arrive at

$$\int_{v_i} (\nabla \times \mathbf{T}) \cdot (\frac{1}{\mu_r} \nabla \times \mathbf{E}) dv +$$

$$\int_{\partial V_i} \mathbf{T} \cdot [\hat{\mathbf{n}} \times (\frac{1}{\mu_r} \nabla \times \mathbf{E})] ds - k_0^2 \epsilon_r \int_{v_i} \mathbf{T} \cdot \mathbf{E} dv = -j\mu_0\omega \int_{v_i} \mathbf{T} \cdot \mathbf{J}^{imp} dv \tag{5.4}$$

If we define

$$\mathbf{J}|_{\partial v_i} = \hat{\mathbf{n}} \times \mathbf{H} \tag{5.5}$$

equation (5.4) can be deduced into

$$\int_{v_i} (\nabla \times \mathbf{T}) \cdot (\frac{1}{\mu_r} \nabla \times \mathbf{E}) dv - j\omega\mu_0 \int_{\partial V_i} \mathbf{T} \cdot \mathbf{J} ds$$

$$-k_0^2 \epsilon_r \int_{v_i} \mathbf{T} \cdot \mathbf{E} dv = -j\mu_0\omega \int_{v_i} \mathbf{T} \cdot \mathbf{J}^{imp} dv \tag{5.6}$$

In equation (5.6), $\mathbf{J}$ on interface between sub-domains need to be evaluated. The Riemann solver for $\mathbf{J}$ is used to evaluate the $\mathbf{J}$ on interface

$$\mathbf{J}|_{\partial V_i} = \frac{Z^{(1)}\mathbf{J}^{(1)} + \hat{\mathbf{n}} \times \hat{\mathbf{n}} \times \mathbf{E}^{(1)} - Z^{(2)}\mathbf{J}^{(2)} - \hat{\mathbf{n}} \times \hat{\mathbf{n}} \times \mathbf{E}^{(2)}}{Z^{(1)} + Z^{(2)}} \tag{5.7}$$

where $Z^{(i)}$ is the wave impedance of sub-domain i, $Z^{(i)} = \sqrt{\frac{\mu_{r,i}}{\epsilon_{r,i}}}$, $\hat{\mathbf{n}}$ is the unit vector of the outer normal direction.

Then, the $\mathbf{J}$ is substituted into equation (5.6) and expand the $\mathbf{E}$ and $\mathbf{J}$ by basis function, and choose testing function the same as basis function.

For FEM sub-domain, the constant tangential linear normal (CT-LN) curl conforming basis function is used to expand the electric field.

$$\mathbf{E}(\mathbf{r}) = \sum_{j=1}^{N^{(e)}} E_j \mathbf{\Phi}_j(\mathbf{r}) \tag{5.8}$$

where $N^{(e)}$ is the number of edges in 1 tetrahedron, and E_j is the expansion coefficients. The FEM basis functions are defined in the physical domain ,and the detailed definition can be found in chapter 4.

For SEM sub-domain, the mixed-order curl conforming Gauss-Lobatto-Legendre (GLL) basis function is used to expand the electric field.

The **E** field can be expressed in a reference cubic element as

$$\begin{aligned}\tilde{\mathbf{E}}(\xi,\eta,\zeta) &= \sum_{r=0}^{N_\xi-1}\sum_{s=0}^{N_\eta}\sum_{t=0}^{N_\zeta} E^{\xi}(\xi_r,\eta_s,\zeta_t)\mathbf{\Phi}^{\xi}_{rst} + \sum_{r=0}^{N_\xi}\sum_{s=0}^{N_\eta-1}\sum_{t=0}^{N_\zeta} E^{\eta}(\xi_r,\eta_s,\zeta_t)\mathbf{\Phi}^{\eta}_{rst} \\ &+\sum_{r=0}^{N_\xi}\sum_{s=0}^{N_\eta}\sum_{t=0}^{N_\zeta-1} E^{\zeta}(\xi_r,\eta_s,\zeta_t)\mathbf{\Phi}^{\zeta}_{rst} = \sum_{j=1}^{N^{(e)}} E_j\mathbf{\Phi}_j(\xi,\eta,\zeta) \end{aligned} \tag{5.9}$$

where $N^{(e)} = N_\xi(N_\eta+1)(N_\zeta+1)+(N_\xi+1)N_\eta(N_\zeta+1)+(N_\xi+1)(N_\eta+1)N_\zeta$ is the number of basis functions in a single hexahedron element, $j=(r,s,t)$ is a compound index, and $\{E_j\}$ are the expansion coefficients. The detailed definition SEM basis function can be found in chapter 4.

Up to here, we have $\sum_{i=1}^{N_s}(N_i^{ei}+N_i^{eb}+N_i^{j})$ unknowns but only $\sum_{i=1}^{N_s}(N_i^{ei}+N_i^{eb})$ equations, where N_s is the number of sub-domains, N_i^{ei} is the number of unknowns for internal electric in sub-domain i, N_i^{eb} is the number of unknowns for boundary electric in sub-domain i, N_i^{j} is the number of unknowns for auxiliary current in sub-domain i. The fact is only the continuity of tangential component of **H** is enforced on the interface between sub-domains, by using equation(5.7). The continuity of tangential component of **E** on the interface between sub-domains need to be enforced. The Riemann solver for **E** can be expressed as

$$\hat{\mathbf{n}}\times\mathbf{E} = \frac{\hat{\mathbf{n}}\times(Y^{(1)}\mathbf{E}^{(1)}-\mathbf{J}^{(1)}+Y^{(2)}\mathbf{E}^{(2)}-\mathbf{J}^{(2)})}{Y^{(1)}+Y^{(2)}} \tag{5.10}$$

where $Y^{(i)}$ is the wave admittance of sub-domain i, $Y^{(i)}=\sqrt{\frac{\epsilon_{r,i}}{\mu_{r,i}}}$, $\hat{\mathbf{n}}$ is the unit vector of the outer normal direction.

By the same manner the **E** and **J** are expanded by appropriate basis function. And using $\hat{\mathbf{n}}\times\mathbf{T}$ to apply the Galerkin procedure for equation (5.10). The same number of equations and unknowns can be obtained. And the linear equations can

be expressed in matrix form as

$$\begin{bmatrix} A_i & C_i & 0 \\ C_i^T & B_i & D_i \\ 0 & E_i & T_i \end{bmatrix} \begin{bmatrix} e_i^i \\ e_i^b \\ J_i \end{bmatrix} = \begin{bmatrix} y_i^i \\ y_i^b \\ 0 \end{bmatrix} + \sum_{j \neq i}^{j \in neig(i)} \begin{bmatrix} 0 & 0 & 0 \\ 0 & B_{i,j} & D_{i,j} \\ 0 & E_{i,j} & T_{i,j} \end{bmatrix} \begin{bmatrix} e_j^i \\ e_j^b \\ J_j \end{bmatrix} \quad (5.11)$$

where subscription i indicate sub-domain index. The first two equations in equation (5.11) is obtained from equation (5.6) by separating the internal and boundary unknowns for electric field (e^i, e^b represent the expanding coefficient of internal and boundary electric field, respectively). The last equation in equation (5.11) is obtained from equation (5.10).

The equation (5.11) still shows the coupling between sub-domains. If we use an iterative scheme (Gauss-Seidel etc.) and take the previous steps solution of all neighbor sub-domain to update the coupling term on the right hand side of the equation (5.11), the matrix form iterative linear equation can be obtained,

$$\begin{bmatrix} A_i & C_i & 0 \\ C_i^T & B_i & D_i \\ 0 & E_i & T_i \end{bmatrix} \begin{bmatrix} e_{i,k+1}^i \\ e_{i,k+1}^b \\ J_{i,k+1} \end{bmatrix} = \begin{bmatrix} y_i^i \\ y_i^b \\ 0 \end{bmatrix}$$
$$+ \sum_{j \neq i}^{j \in neig(i)} \begin{bmatrix} 0 & 0 & 0 \\ 0 & B_{i,j} & D_{i,j} \\ 0 & E_{i,j} & T_{i,j} \end{bmatrix} \begin{bmatrix} e_{j,k}^i \\ e_{j,k}^b \\ J_{j,k} \end{bmatrix} \quad (5.12)$$

where $k+1$ and k represent the solution of unknown vector in the $k+1_{th}$ and k_{th} step , respectively.

The detailed expressions for those sub-matrices in equation (5.12) are shown in following equations

$$A_{i,mn} = \int_{V_i} \left[(\nabla \times \mathbf{\Phi}_m^i) \cdot \frac{1}{\mu_r} (\nabla \times \mathbf{\Phi}_n^i) - k_0^2 \epsilon_r \mathbf{\Phi}_m^i \cdot \mathbf{\Phi}_n^i \right] dv \quad (5.13)$$

$$B_{i,mn} = \int_{V_i} \left[(\nabla \times \mathbf{\Phi}^b_m) \cdot \frac{1}{\mu_r} (\nabla \times \mathbf{\Phi}^b_n) - k_0^2 \epsilon_r \mathbf{\Phi}^b_m \cdot \mathbf{\Phi}^b_n \right] dv$$
$$- j\omega\mu_0 \int_{\Gamma_i} \frac{1}{Z^{(i)} + Z^{(j)}} \mathbf{\Phi}^b_m \cdot (\hat{\mathbf{n}} \times \hat{\mathbf{n}} \times \mathbf{\Phi}^b_n) ds \tag{5.14}$$

$$C_{i,mn} = \int_{V_i} \left[(\nabla \times \mathbf{\Phi}^i_m) \cdot \frac{1}{\mu_r} (\nabla \times \mathbf{\Phi}^b_n) - k_0^2 \epsilon_r \mathbf{\Phi}^i_m \cdot \mathbf{\Phi}^b_n \right] dv \tag{5.15}$$

$$D_{i,mn} = -j\omega\mu_0 \int_{\Gamma_i} \frac{Z^{(i)}}{Z^{(i)} + Z^{(j)}} \mathbf{\Phi}^b_{i,m} \cdot \mathbf{f}_{j,n} ds \tag{5.16}$$

$$E_{i,mn} = \int_{\Gamma_i} \frac{Y^{(j)}}{Y^{(i)} + Y^{(j)}} (\hat{\mathbf{n}} \times \mathbf{f}_{i,m}) \cdot (\hat{\mathbf{n}} \times \mathbf{\Phi}^b_{i,n}) ds \tag{5.17}$$

$$T_{i,mn} = \int_{\Gamma_i} \frac{1}{Y^{(i)} + Y^{(j)}} (\hat{\mathbf{n}} \times \mathbf{f}_{i,m}) \cdot (\hat{\mathbf{n}} \times \mathbf{f}_{i,n}) ds \tag{5.18}$$

$$B_{ij,mn} = \int_{\Gamma_i} \frac{-j\omega\mu_0}{Z^{(i)} + Z^{(j)}} \mathbf{\Phi}^b_{i,m} \cdot (\hat{\mathbf{n}} \times \hat{\mathbf{n}} \times \mathbf{\Phi}^b_{j,n}) ds \tag{5.19}$$

$$D_{ij,mn} = -j\omega\mu_0 \int_{\Gamma_i} \frac{Z^{(j)}}{Z^{(i)} + Z^{(j)}} \mathbf{\Phi}^b_{i,m} \cdot \mathbf{f}_{j,n} ds \tag{5.20}$$

$$E_{ij,mn} = \int_{\Gamma_i} \frac{Y^{(j)}}{Y^{(i)} + Y^{(j)}} (\hat{\mathbf{n}} \times \mathbf{f}_{i,m}) \cdot (\hat{\mathbf{n}} \times \mathbf{\Phi}^b_{j,n}) ds \tag{5.21}$$

$$T_{ij,mn} = -\int_{\Gamma_i} \frac{1}{Y^{(i)} + Y^{(j)}} (\hat{\mathbf{n}} \times \mathbf{f}_{i,m}) \cdot (\hat{\mathbf{n}} \times \mathbf{f}_{j,n}) ds \tag{5.22}$$

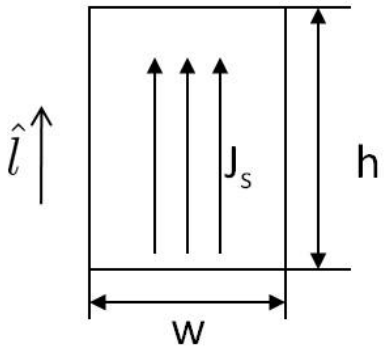

FIGURE 5.2: An implementation of a 2D lumped element in FEM (SEM)

5.2.2 Modeling of Lumped Element

In interconnect problems, the most useful excitation is a voltage source with internal resistance. This voltage source can be modeled by a lumped element [42, 43, 44]. The lumped element can be treated as an additional electrical current source in the wave equation. There are different types of implementation of the lumped elements. The lumped element can be 1D, 2D or 3D, which imposes the additional electric current on an edge, a face or a volume. In this work, 2D lumped element is chosen [45].

A 2D lumped element is defined on a FEM surface, which is a rectangle with length of h and width of w, as shown in Fig. 5.2. The $\mathbf{J}^{lump}$ is uniformly distributed on the rectangle, and the direction of $\mathbf{J}^{lump}$ is $\hat{l}$.

The equivalent circuit of the lumped element is shown in Fig. 5.3. The lumped element is a voltage source with V_s, with internal resistance R_s. If $V_s = 0$, the lumped element becomes a resistor.

The lumped element can be considered as a current source J^{lump} in the wave equation, the modified wave equation is

$$\nabla \times \frac{1}{\mu_r} \nabla \times \mathbf{E} - k_0^2 \epsilon_r \mathbf{E} = -j\omega\mu_0 \mathbf{J}^{imp} - j\omega\mu_0 \mathbf{J}^{lump} \tag{5.23}$$

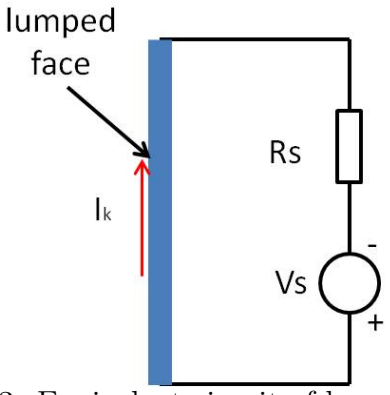

FIGURE 5.3: Equivalent circuit of lumped element

The electric current density can be expressed as

$$\mathbf{J}_s = \frac{I}{w}\hat{l} \tag{5.24}$$

Substituting the voltage-current relationship of the lumped element, the electric current density can be expressed as

$$\mathbf{J}_s = \frac{I}{w}\hat{l} = \frac{V_s - V}{wR_s}\hat{l} \tag{5.25}$$

where V is the voltage drop on the lumped element, it can be expressed by a line integral of the electric field,

$$V = -\int \mathbf{E} \cdot d\bar{l} \tag{5.26}$$

In lumped element, the size of the element is very small compared with wavelength, so

$$V = -\int \mathbf{E} \cdot d\bar{l} = -h\mathbf{E} \cdot \hat{l} \tag{5.27}$$

the surface current density is substituted into the wave equation (5.23)

$$\nabla \times \frac{1}{\mu_r}\nabla \times \mathbf{E} - k_0^2 \epsilon_r \mathbf{E} = -j\omega\mu_0 \mathbf{J}^{imp} - j\omega\mu_0 \frac{V_s + h\mathbf{E} \cdot \hat{l}}{wR_s}\hat{l} \tag{5.28}$$

The Galerkin process $\int_V \mathbf{\Phi}_k \cdot dv$ is applied to the wave equation, the additional term corresponding to the lumped element can be expressed as

$$-j\omega\mu_0 \int_V \mathbf{\Phi}_k \cdot \mathbf{J}^{lump} dv = -j\omega\mu_0 \int_S \mathbf{\Phi}_k \cdot \hat{l} \frac{V_s + h\mathbf{E} \cdot \hat{l}}{wR_s} dS$$
$$= -\frac{j\omega\mu_0 V_s}{wR_s} \int_S \mathbf{\Phi}_k \cdot \hat{l} dS + \frac{j\omega\mu_0 h}{wR_s} \int_S (\mathbf{E} \cdot \hat{l})(\mathbf{\Phi}_k \cdot \hat{l}) dS \tag{5.29}$$

The first term is an additional term in the RHS corresponding to source. The $\mathbf{E}$ in the can be expanded by the basis function as

$$\mathbf{E} = \sum_{p=1}^{N^{(e)}} e_p \mathbf{\Phi}_p \tag{5.30}$$

And the $\mathbf{J}^{lump}$ only exists on the lumped element surface, the corresponding additional LHS can be expressed as

$$A_{p,k}^{lump} = \frac{j\omega\mu_0 h}{wR_s} \int_S (\mathbf{\Phi}_p \cdot \hat{l})(\mathbf{\Phi}_k \cdot \hat{l}) dS \tag{5.31}$$

The $A_{p,k}^{lump}$ is added to the system matrix in the left part of the equation (5.12) to the corresponding entries $A_{p,k}$. Then the linear equations, which include the contribution of the lumped element, can be obtained.

After obtaining the linear equations, the solving process can be done in two steps. The first step is the LU factorization for every sub-domain. The second step is doing a Gauss-Seidel iteration for every sub-domain; in the loop, we first update the RHS term for current sub-domain using the solution obtained in last step, and then solve for current sub-domain using the LU factorization, update the solution for current sub-domain. When the residue is smaller than a prescribed tolerance the program can be terminated. The procedure is shown in the Fig. 5.4.

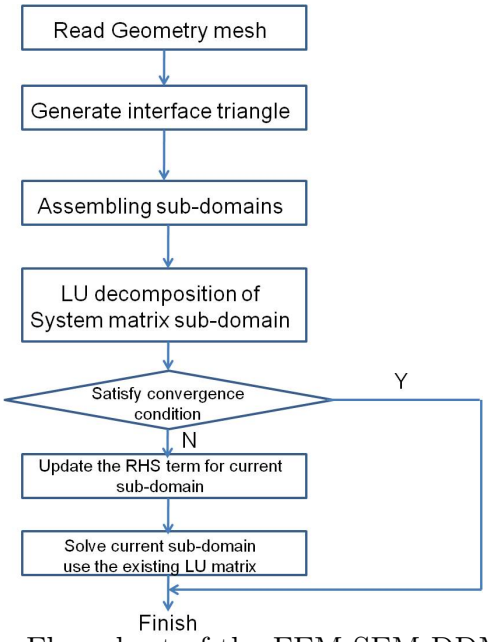

FIGURE 5.4: Flow chart of the FEM-SEM DDM algorithm

5.3 Numerical Examples

The first example is a micro-stripe low pass filter. The model of this low pass filter is shown in the Fig. 5.5. The dimension of the filter is on the order of 1 cm. The dielectric constant of the substrate material is $\epsilon_r = 4.8$, and the thickness of the substrate is 3.18 mm. There are two lumped ports placed at two terminals of the microstrip line, the first port is a 1V voltage source located at the $+X$ terminal micro-strip line (as shown in Fig. 5.5), with a 50 Ω internal resistance, in $\hat{z}$ direction , the second lumped port is located at $-X$ terminal of the micro-strip line (as shown in Fig. 5.5), with a 50 Ω matching resistor. The detail dimension is shown in the Fig. 5.6.

The scattering parameter is extracted for 0.8 GHz to 3 GHz as shown in Fig. 5.7 and Fig. 5.8. The comparison shows the SEM-FEM result has good agreement with HFFS and WCT results.

Next example is a real multi-scale problems. This example is to simulate the

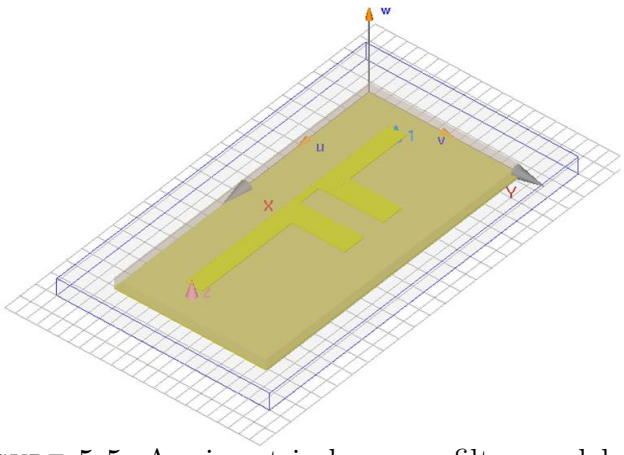

FIGURE 5.5: A microstrip low pass filter model

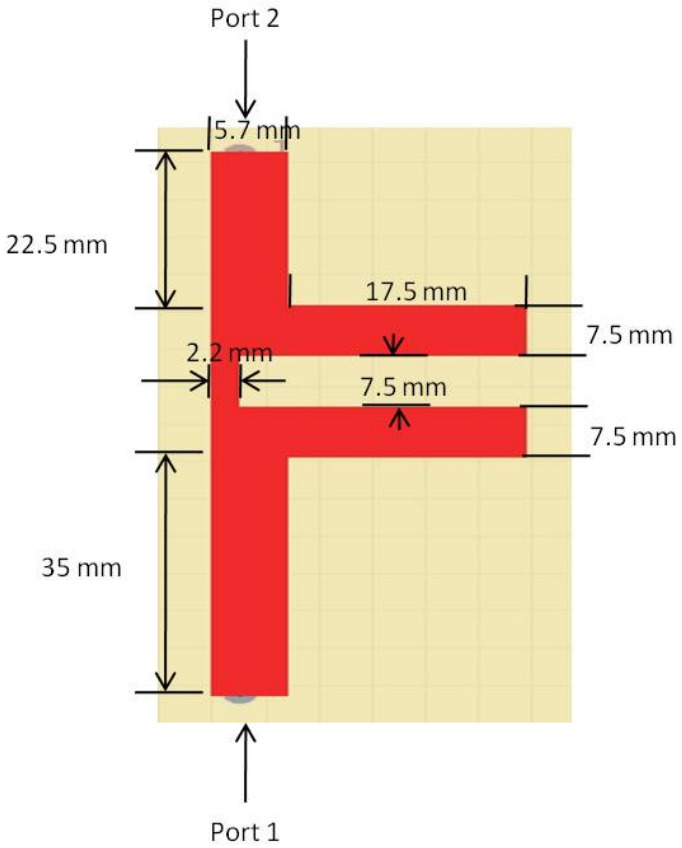

FIGURE 5.6: The detailed dimension of microstrip low pass filter model

filter in the example 1 beside a PEC stirrer. The detail dimension of the stirrer is shown in Fig. 5.9. The filter is excited at port 1, and port 2 is loaded with a 50 Ω matched resistor. The ratio of the largest dimension and the smallest dimension of

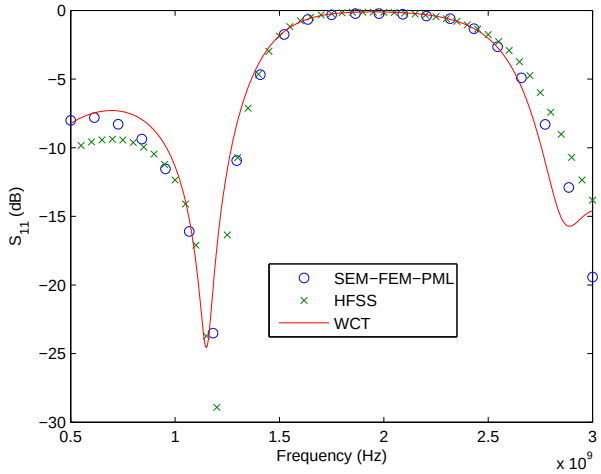

FIGURE 5.7: The S_{11} of microstrip low pass filter model from 0.8 GHz to 3 GHz

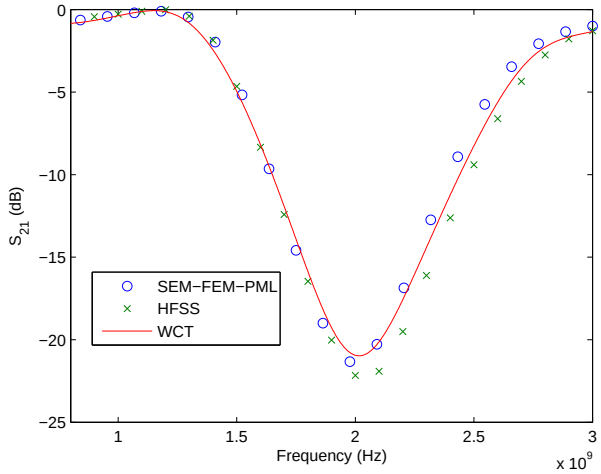

FIGURE 5.8: The S_{21} of microstrip low pass filter model from 0.8 GHz to 3 GHz

the structure is 1032. The example is calculated by FEM-SEM, HFSS and WCT. The results of FEM-SEM agree well with WCT results. The HFSS result agree well with other results for low frequency, for the high frequency is not accurate becuase the limit of memory. The S_{11} and S_{21} from different methods are shown in the Fig. 5.10 and Fig. 5.11, respectively.

The computational costs are list in Table. 5.1. From the comparison of the SIM-SEM DDM and HFSS in Table. 5.1, we can conclude the proposed method is much

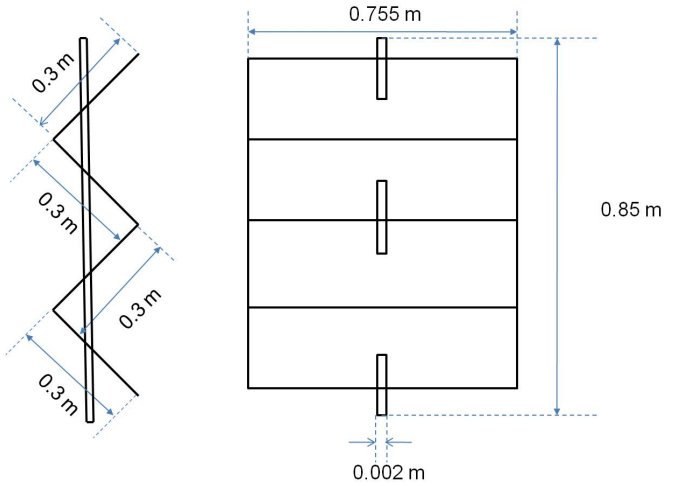

FIGURE 5.9: The detailed dimension of PEC stirrer

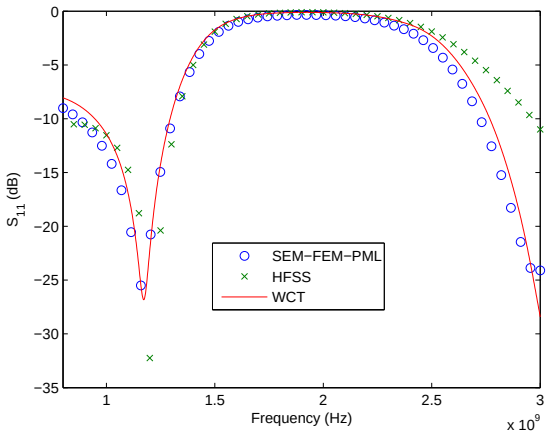

FIGURE 5.10: S_{11} of the microstrip low pass filter beside the PEC stirrer from 0.8 GHz to 3 GHz

more efficient both in terms of memory and CPU time for multi-scale structure.

The third example is a patch antenna. The dielectric constant of the substrate is $\epsilon_r = 2.2$. The thickness of substrate is 3.176 mm. The antenna is fed by a lumped port which is named as port 1, as shown in Fig. 5.12. The dimension of the antenna is shown as the Fig. 5.12. The model is divided in to 12 sub-domains (8 hexahedron sub-domains and 4 tetrahedron sub-domains) as shown in Fig. 5.13. The largest size of FEM element is 35 mm, and the smallest size of FEM element is 2.2 mm.

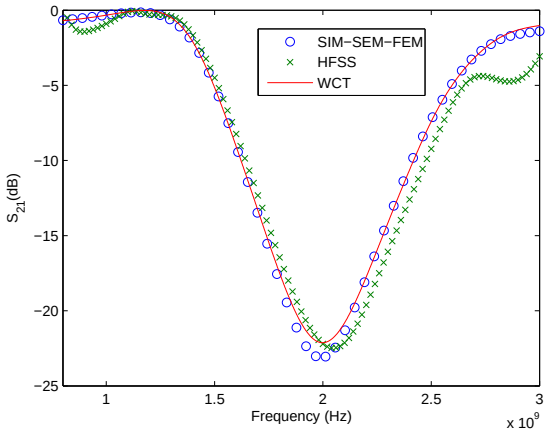

FIGURE 5.11: S_{11} of the microstrip low pass filter beside the PEC stirrer from 0.8 GHz to 3 GHz

Table 5.1: Memory and CPU time cost of a microstrip low pass filter beside PEC stirrer example

	HFSS	SEM-FEM DDM
CPU time	6:51:24 for fast sweep up to 2 GHz (3 cores)	122 s per frequency
Memory (GB)	22.7	1.99

The scattering parameter is extracted from 0.2 GHz to 2.5 GHz as shown in Fig. 5.14. The results of FEM-SEM agree well with WCT results. The HFSS result agree well with other results for low frequency, for the high frequency is not accurate becuase the limit of memory. The S_{11} has a valley value at which is corresponding the resonant frequency of the antenna. The computational costs are listed in the Table. 5.2.

From the comparison of the SIM-SEM DDM and HFSS in Table. 5.2, we can

Table 5.2: Memory and CPU time cost of a patch antenna beside PEC stirrer example

	HFSS	SEM-FEM DDM
CPU time (per frequencies) (s)	more than 3 days	147
Memory (GB)	30	2.883

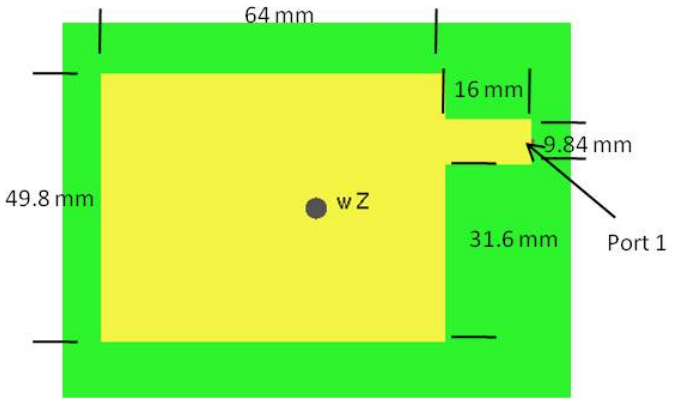

FIGURE 5.12: The detailed dimension of the patch antenna model

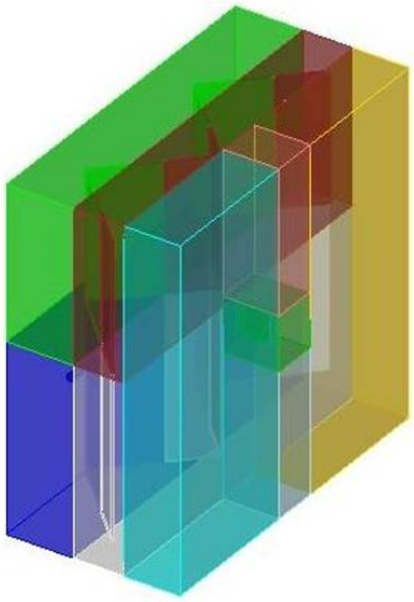

FIGURE 5.13: The front view of the PEC stirrer

conclude the proposed method is much more efficient both in terms of memory and CPU time for multi-scale structure.

5.4 Conclusion

In this chapter, we studied the applications of SEM-FEM-DDM algorithm for interconnect problems. This method combines FEM and SEM by discontinuous Galerkin method. Instead of using global conforming elements as in conventional FEM,

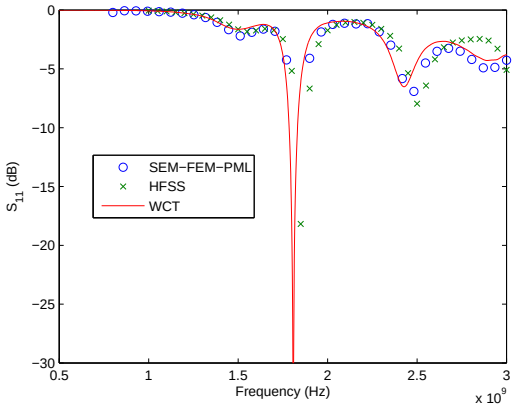

FIGURE 5.14: S_{11} of the patch antenna beside a PEC stirrer from 0.2 GHz to 2.5 GHz

the proposed method can use arbitrary non-conforming elements for different subdomains. The scattering parameter is extracted and compared with commercial software. The results show good agreement. The proposed method is much more efficient both in memory and CPU time than conventional FEM for interconnect problems. Furthermore, the proposed method is very flexible in geometry modeling and mesh generation. The proposed method is a very good choice for solving multi-scale interconnect problems.

6

DDM with SIM-SEM-FEM for Multi-scale Scattering Problems

6.1 Motivation

In the chapter 4 and chapter 5, the SEM-FEM DDM is implemented via Robin's boundary condition and discontinuous Galerkin method. It is applied for bounded problems and interconnect problems with PML. In chapter 3, an interpolation matrix is used between SIM and SEM. So the SEM surface mesh needs to be conforming to SIM mesh, which is a uniform mesh on a cuboid surface. However, it is very difficult to generate a mesh for an arbitrary 3D structure which can satisfy this requirement.

In this chapter, the idea of discontinuous Galerkin method is borrowed into the hybridization of SIM and SEM. We take advantage of the ability of DG to deal with non-conforming meshes. The geometrical modeling for the SIM-SEM-FEM based on DG is much more flexible. And the flexibility of geometrical modeling for multi-scale problems means much smaller number of elements. As domain decomposition methods (DDM) can separate electrically large parts from electrically fine parts, the number of elements can be reduced and a large linear system can be converted into

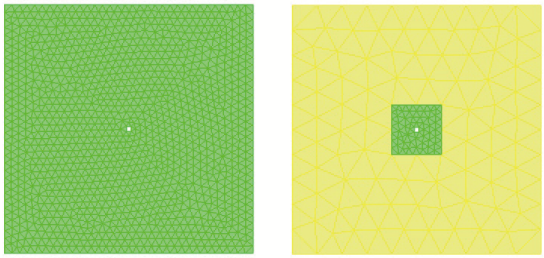

FIGURE 6.1: The spatial discretization schemes in conventional FEM (a) on the left, and in non-conformal domain decomposition scheme (b) on the right. The conventional scheme uses 2,410 triangular elements , while the non-conformal domain decomposition scheme uses only 302 triangular elements

several smaller linear systems which are easier to solve. Fig. 6.1 (a) shows a simple 2D FEM mesh for such a multi-scale problem. This structure has a fine scale feature size of 0.01λ (1% of a wavelength) and the large size of $1\lambda \times 1\lambda$. In order to construct fine structure accurately, element size in conventional FEM is equal to 0.03λ. The conformal triangular mesh is shown in Fig. 6.1 (a). The number of conformal triangular elements is 2410. And following DDM scheme, the problem can be divided into 2 sub-domains to separate electrically large part and electrically fine part. With a non-conformal mesh, different sub-domains can be meshed independently, as shown in Fig. 6.1 (b). For the fine structure the same element size as in the conformal mesh is used. For the other parts the element size of 0.1λ which is a typical element size in conventional FEM for smooth structure is used. In the DDM scheme, the number of triangular elements can be reduced to 302. It is our goal to develop such a domain decomposition to solve multi-scale electromagnetic problems more efficiently.

The discontinuous Galerkin method [38, 46, 47] is a category of domain decomposition methods. In a DG method, the continuity of tangential field components is imposed approximately by the numerical flux across an interface between different sub-domains. As evaluating the numerical flux does not require a conformal mesh between the adjacent sub-domains, the DG method can deal with an arbitrary non-conformal mesh on the sub-domain interface. Thus, the mesh generation procedure

is independent for each sub-domain, making the mesh generation considerably easier as the size and type of meshes can be completely different in different sub-domains. The ability to deal with arbitrary non-conformal mesh provides DG methods with high flexibility in geometric modeling.

The objective of the proposed algorithm is to efficiently handle problems with multi-scale structures, by using the FEM to model electrically fine sub-domains, using the SEM [25] to model electrically coarse and smooth sub-domains, and using the SIM [9, 48] to truncate field on the outer boundary. This combination can reduce the total number of elements used in solving multi-scale problems, thus it is more efficient than conventional FEM. The DG method with a Riemann solver provides a good framework for non-conformal meshes to be used in the proposed DDM.

6.2 Formulation

A typical problem with multi-scale structures is shown in Fig. 6.2, which contains both electrically coarse structures and electrically fine details compared with the wavelength.

In the conventional FEM for such a multi-scale problem in Fig. 6.2, the electric field is calculated from the vector Helmholtz equation

$$\nabla \times \frac{1}{\mu_r} \nabla \times \mathbf{E} - k_0^2 \epsilon_r \mathbf{E} = -j\omega\mu_0 \mathbf{J}^{imp} \tag{6.1}$$

where $\mathbf{E}$ is the electric field, ϵ_r and μ_r are the relative permittivity and permeability respectively, k_0 is the wave number of free space, $\mathbf{J}^{imp}$ is the imposed electric current density. The whole computational domain is discretized by continuous edge elements in a globally conformal mesh. In a multi-scale problem, due to the presence of both geometrically fine details and large coarse structures, the number of elements can be very large and the computational cost is high. A typical conformal FEM mesh in 2D is shown in Fig. 6.1(a).

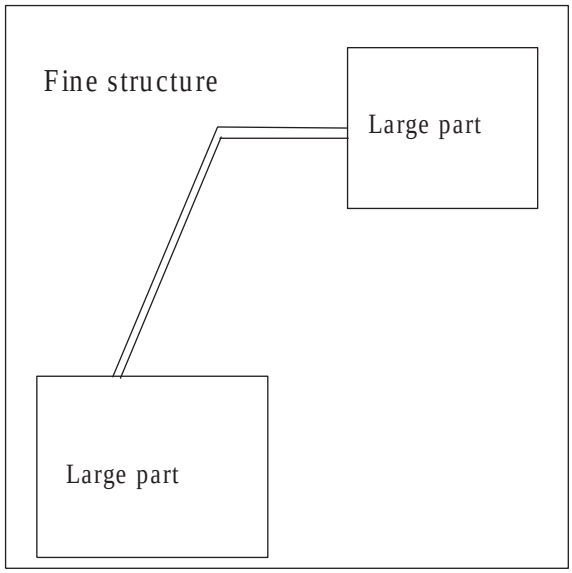

FIGURE 6.2: A typical multi-scale problem with both electrically coarse structures and electrically fine details in comparison with the wavelength. (The problem is illustrated in 2D for simplicity, but this work deals with 3D multi-scale problems.)

On the other hand, the proposed domain decomposition method will first divide the problem into several sub-domains, each of which will be meshed independently, as shown in Fig. 6.1(b). Then the SEM based on hexahedron elements is used for electrically large and smooth sub-domains, the FEM based on tetrahedron elements is used for electrically fine structures, and the SIM is used as the exact radiation boundary condition. In general, the whole problem is divided into N_s SEM sub-domains, N_f FEM sub-domains, and one SIM sub-domain for the radiation boundary condition.

For sub-domain i, the $\mathbf{\Psi}$ is chosen as the testing function, after applying testing procedure, the weak form of the wave equation can be expressed as

$$\int_{\Omega_i} \mathbf{\Psi} \cdot [\nabla \times \frac{1}{\mu_{r_i}} \nabla \times \mathbf{E} - k_0^2 \epsilon_{r_i} \mathbf{E}] dv = -j\omega\mu_0 \int_{\Omega_i} \mathbf{\Psi} \cdot \mathbf{J}^{imp} dv \tag{6.2}$$

Applying integration by part for equation (6.2) yields

$$\int_{\Omega_i} [\nabla \times \mathbf{\Psi} \cdot \frac{1}{\mu_{r_i}} \nabla \times \mathbf{E} - k_0^2 \epsilon_{r_i} \mathbf{\Psi} \cdot \mathbf{E}] dv +$$

$$\int_{\Gamma_i} \mathbf{\Psi} \cdot [\hat{\mathbf{n}} \times (\frac{1}{\mu_{r_i}}) \nabla \times \mathbf{E}] ds = \int_{\Omega_i} -j\omega\mu_0 \mathbf{\Psi} \cdot \mathbf{J}^{imp} dv \tag{6.3}$$

where $\hat{\mathbf{n}}$ is the outer normal direction of ith sub-domain, and Γ_i is the surface of Ω_i. Substituting the relationship of electric field $\mathbf{E}$ and magnetic field $\mathbf{H}$ from Maxwell's equation

$$\frac{1}{\mu_{r_i}} \nabla \times \mathbf{E} = -j\omega\mu_0 \mathbf{H} \tag{6.4}$$

we can obtain

$$\int_{\Omega_i} [\nabla \times \mathbf{\Psi} \cdot \frac{1}{\mu_{r_i}} \nabla \times \mathbf{E} - k_0^2 \epsilon_{r_i} \mathbf{\Psi} \cdot \mathbf{E}] dv +$$

$$-j\omega\mu_0 \int_{\Gamma_i} \mathbf{\Psi} \cdot (\hat{\mathbf{n}} \times \mathbf{H}) ds = \int_{\Omega_i} -j\omega\mu_0 \mathbf{\Psi} \cdot \mathbf{J}^{imp} dv \tag{6.5}$$

It is clear that the tangential magnetic field need to be evaluated on the interface of sub-domains i. As mentioned in the introduction part, Robin's boundary condition and Riemann solver are two types schemes widely used to connect different sub-domains.

If we choose the Robin's boundary condition [32] which can be expressed as

$$\frac{1}{\mu_r^{(i)}} \nabla \times \mathbf{E}^{(i)} - jk^{(i)} \mathbf{E}^{(i)} = \frac{1}{\mu_r^{(j)}} \nabla \times \mathbf{E}^{(j)} - jk^{(j)} \mathbf{E}^{(j)} \tag{6.6}$$

where the superscript is the index of the sub-domain, and sub-domain j is a neighbor of sub-domain i. From equations (6.5 and 6.6), the interior problem can be solved by standard Galerkin procedure.

On the other hand, if we choose Riemann solver as the numerical flux, where the Riemann solver for $\mathbf{H}$ can be expressed as

$$\begin{aligned}(Z^{(i)} + Z^{(j)})\hat{\mathbf{n}}^{(i)} \times \mathbf{H} = \hat{\mathbf{n}}^{(i)} \times (Z^{(i)}\mathbf{H}^{(i)} + Z^{(j)}\mathbf{H}^{(j)}) \\ +\hat{\mathbf{n}}^{(i)} \times \hat{\mathbf{n}}^{(i)} \times (\mathbf{E}^{(i)} - \mathbf{E}^{(j)})\end{aligned} \tag{6.7}$$

where$Z^{(i)} = \sqrt{\frac{\mu_i}{\epsilon_i}}$ is the wave impedance of the ith sub-domain, and $Z^{(j)} = \sqrt{\frac{\mu_j}{\epsilon_j}}$ is the wave impedance of the neighboring j sub-domain. Substitute the $\hat{\mathbf{n}}^{(i)} \times \mathbf{H}$ into the surface integral term in equation (6.5)

$$\begin{aligned}&\int_{\Omega_i} [\nabla \times \mathbf{\Psi} \cdot \frac{1}{\mu_{r_i}} \nabla \times \mathbf{E} - k_0^2 \epsilon_{r_i} \mathbf{\Psi} \cdot \mathbf{E}] dv + \\ &-j\omega\mu_0 \int_{\Gamma_i} \mathbf{\Psi} \cdot \frac{\hat{\mathbf{n}}^{(i)} \times (Z^{(i)}\mathbf{H}^{(i)} + Z^{(j)}\mathbf{H}^{(j)})}{Z^{(i)} + Z^{(j)}} ds \\ &-j\omega\mu_0 \int_{\Gamma_i} \mathbf{\Psi} \cdot \frac{\hat{\mathbf{n}}^{(i)} \times \hat{\mathbf{n}}^{(i)} \times (\mathbf{E}^{(i)} - \mathbf{E}^{(j)})}{Z^{(i)} + Z^{(j)}} ds \\ &= \int_{\Omega_i} -j\omega\mu_0 \mathbf{\Psi} \cdot \mathbf{J}^{imp} dv\end{aligned} \tag{6.8}$$

Riemann solver for $\mathbf{E}$ is used to construct an additional equation,

$$\begin{aligned}(Y^{(i)} + Y^{(j)})\hat{\mathbf{n}}^{(i)} \times \mathbf{E} = \hat{\mathbf{n}}^{(i)} \times (Y^{(i)}\mathbf{E}^{(i)} + Y^{(j)}\mathbf{E}^{(j)}) \\ +\hat{\mathbf{n}}^{(i)} \times \hat{\mathbf{n}}^{(i)} \times (-\mathbf{H}^{(i)} + \mathbf{H}^{(j)})\end{aligned} \tag{6.9}$$

where$Y^{(i)} = \sqrt{\frac{\epsilon_1}{\mu_i}}$ is the wave admittance of i sub-domain, and $Y^{(j)} = \sqrt{\frac{\epsilon_j}{\mu_j}}$ is the wave admittance of neighbor j sub-domain. For simplicity, we use $\mathbf{J}^{(i)} = \hat{\mathbf{n}}^{(i)} \times \mathbf{H}^{(i)}$, which is auxiliary current on interface. The superscript is used to denote sub-domain.

Then the equation(6.8,6.9) for sub-domain i can be rewritten as,

$$\int_{\Omega_i}[\nabla\times\mathbf{\Psi}\cdot\frac{1}{\mu_{r_i}}\nabla\times\mathbf{E}-k_0^2\epsilon_{r_i}\mathbf{\Psi}\cdot\mathbf{E}]dv+$$
$$-j\omega\mu_0\int_{\Gamma_i}\mathbf{\Psi}\cdot\frac{(Z^{(i)}\mathbf{J}^{(i)}-Z^{(j)}\mathbf{J}^{(j)})}{Z^{(i)}+Z^{(j)}}ds$$
$$-j\omega\mu_0\int_{\Gamma_i}\mathbf{\Psi}\cdot\frac{\hat{\mathbf{n}}^{(i)}\times\hat{\mathbf{n}}^{(i)}\times(\mathbf{E}^{(i)}-\mathbf{E}^{(j)})}{Z^{(i)}+Z^{(j)}}ds$$
$$=\int_{\Omega_i}-j\omega\mu_0\mathbf{\Psi}\cdot\mathbf{J}^{imp}dv \tag{6.10}$$

$$\hat{\mathbf{n}}^{(i)}\times\mathbf{E}=\frac{\hat{\mathbf{n}}^{(i)}\times(Y^{(i)}\mathbf{E}^{(i)}-\mathbf{J}^{(i)}+Y^{(j)}\mathbf{E}^{(j)}-\mathbf{J}^{(j)})}{Y^{(i)}+Y^{(j)}} \tag{6.11}$$

The next step is to add the SIM into the system. The SIM can be derived from surface integral equation. And the combined field integral equation can be obtained by linear combination of electric field integral equation (EFIE) and magnetic field integral equation (MFIE) as

$$\alpha\frac{1}{\eta_0}\text{EFIE}+(1-\alpha)\text{MFIE} \tag{6.12}$$

and the matrix form can be express as

$$\mathbf{Z}_a\mathbf{J}^{sim}+\mathbf{Z}_b\mathbf{M}^{sim}=\mathbf{S}^{sim} \tag{6.13}$$

The detail formula for SIM part can be found in [9, 48]. As mentioned, the SIM is treated as a single sub-domain and Riemann solver is applied by the similar way as on the interface of SEM-FEM. One equation coming from Riemann solver is added. The linear combination of Riemann solver for **E** and Riemann solver for **H** is used.

Riemann solver for $\mathbf{E}$ can be expressed by

$$\begin{aligned}(Y^{(sim)}+Y^{(j)})\mathbf{M}^{(sim)} &= Y^{(sim)}\mathbf{M}^{(sim)}\\ -\hat{\mathbf{n}}^{(sim)}\times\mathbf{J}^{(sim)} &- Y^{(j)}\hat{\mathbf{n}}^{(sim)}\times\mathbf{E}^{(j)}\\ +\hat{\mathbf{n}}^{(sim)}\times\mathbf{J}^{(j)}&\end{aligned} \tag{6.14}$$

where $\hat{\mathbf{n}}^{(sim)}$ is the outer normal direction of SIM sub-domain. Riemann solver for $\mathbf{H}$ can be expressed by

$$\begin{aligned}(Z^{(sim)}+Z^{(j)})\mathbf{J} &= Z^{(sim)}\mathbf{J}^{(sim)}+Z^{(j)}\mathbf{J}^{(j)}\\ +\hat{\mathbf{n}}^{(sim)}\times\mathbf{M}^{(sim)} &+ \hat{\mathbf{n}}^{(sim)}\times\hat{\mathbf{n}}^{(sim)}\times\mathbf{E}^{(j)}\end{aligned} \tag{6.15}$$

The linear combination of Riemann solver for $\mathbf{E}$ and $\mathbf{F}$

$$\alpha\text{Riemann}_E+(1-\alpha)\eta_0\text{Riemann}_H=0; \tag{6.16}$$

where α can be chosen between 0 and 1, and η_0 is the impedance of free space.

As of now, all equations have been constructed, the next step is expanding all unknown fields including $\mathbf{E}$, $\mathbf{H}$, $\mathbf{J}$, $\mathbf{J}^{sim}$ and $\mathbf{M}^{sim}$ by appropriate basis functions.

For $\mathbf{E}$ in FEM sub-domain, the CT-LN curl conforming basis functions are used to expand the electric field.

$$\mathbf{E}(\mathbf{r})=\sum_{j=1}^{N^{(e)}}E_j\mathbf{\Phi}_j(\mathbf{r}) \tag{6.17}$$

The detailed formulation of CT-LN basis function can be found in chapter 4.

For SEM sub-domain, the mixed-order curl conforming GLL basis functions are used to expand the electric field.

$$\begin{aligned}\tilde{\mathbf{E}}(\xi,\eta,\zeta) &= \sum_{r=0}^{N_\xi-1}\sum_{s=0}^{N_\eta}\sum_{t=0}^{N_\zeta}E^{\xi}(\xi_r,\eta_s,\zeta_t)\mathbf{\Phi}^{\xi}_{rst}+\sum_{r=0}^{N_\xi}\sum_{s=0}^{N_\eta-1}\sum_{t=0}^{N_\zeta}E^{\eta}(\xi_r,\eta_s,\zeta_t)\mathbf{\Phi}^{\eta}_{rst}\\ &+\sum_{r=0}^{N_\xi}\sum_{s=0}^{N_\eta}\sum_{t=0}^{N_\zeta-1}E^{\zeta}(\xi_r,\eta_s,\zeta_t)\mathbf{\Phi}^{\zeta}_{rst}=\sum_{j=1}^{N^{(e)}}E_j\mathbf{\Phi}_j(\xi,\eta,\zeta)\end{aligned} \tag{6.18}$$

The detailed formulation of SEM basis function can be found in chapter 3.

Divergence conforming basis functions $\hat{\mathbf{n}} \times \mathbf{\Phi}$ are used to expand the auxiliary current on the interfaces between sub-domains. This part is the same as in chapter 5. And for SIM sub-domain, the rooftop basis function is used to expand the equivalent electric current and magnetic current as in chapter 2.

After expanding all unknown field and choosing testing function by Galerkin method the system matrix can be obtained, for SEM or FEM sub-domain we have,

$$\begin{bmatrix} A_i & C_i & 0 \\ C_i^T & B_i & D_i \\ 0 & E_i & T_i \end{bmatrix} \begin{bmatrix} e_i^i \\ e_i^b \\ J_i \end{bmatrix} - \sum_{j \in neighbor(i)} \begin{bmatrix} 0 & 0 & 0 \\ 0 & B_{ij} & D_{ij} \\ 0 & E_{ij} & T_{ij} \end{bmatrix} \begin{bmatrix} e_j^i \\ e_j^b \\ J_j \end{bmatrix}$$

$$- \begin{bmatrix} 0 & 0 \\ B_{ij}^{sim} & D_{ij}^{sim} \\ E_{ij}^{sim} & T_{ij}^{sim} \end{bmatrix} \begin{bmatrix} M_{sim} \\ J_{sim} \end{bmatrix} = \begin{bmatrix} y_i^i \\ y_i^b \\ 0 \end{bmatrix} \tag{6.19}$$

The third term on the left side exists only when ith sub-domain is attached to SIM interface.

For the SIM sub-domain we have

$$\begin{bmatrix} B^{sim} & D^{sim} \\ Z_b & Z_a \end{bmatrix} \begin{bmatrix} M_{sim} \\ J_{sim} \end{bmatrix}$$

$$- \sum_{j \in neighbor(sim)} \begin{bmatrix} 0 & F_{ij} & G_{ij} \\ 0 & 0 & 0 \end{bmatrix} \begin{bmatrix} e_j^i \\ e_j^b \\ J_j \end{bmatrix} = \begin{bmatrix} 0 \\ y^{sim} \end{bmatrix} \tag{6.20}$$

The detailed expressions of the matrices related to SIM sub-domain are

$$B_{i,mn}^{sim} = \frac{\alpha Y^j}{Y^{sim} + Y^j} \int_{\Gamma_i} \mathbf{f}_m^{sim} \cdot \mathbf{f}_n^{sim} ds - \frac{(1-\alpha)\eta_0}{Z^{sim} + Z^j} \int_{\Gamma_i} (\hat{\mathbf{n}} \times \mathbf{f}_m^{sim}) \cdot (\hat{\mathbf{n}} \times \mathbf{f}_n^{sim}) ds \tag{6.21}$$

$$B_{ij,mn}^{sim} = -j\omega\mu_0 \int_{\Gamma_i} \frac{1}{Z^{(sim)} + Z^{(j)}} \mathbf{\Phi}_{i,m}^b \cdot (\hat{\mathbf{n}} \times \mathbf{f}_{j,n}^{sim}) ds \tag{6.22}$$

$$D_{ij,mn}^{sim} = j\omega\mu_0 \int_{\Gamma_i} \frac{Z^{(j)}}{Z^{(sim)} + Z^{(j)}} \mathbf{\Phi}_{i,m}^b \cdot \mathbf{f}_{j,n}^{sim} ds \tag{6.23}$$

$$D^{sim}_{i,mn} = \frac{\alpha}{Y^{sim}+Y^j}\int_{\Gamma_i} \mathbf{f}^{sim}_m \cdot (\hat{\mathbf{n}} \times \mathbf{f}^{sim}_n) ds$$
$$+\frac{(1-\alpha)\eta_0 Z^{sim}}{Z^{sim}+Z^j}\int_{\Gamma_i} (\hat{\mathbf{n}} \times \mathbf{f}^{sim}_m) \cdot \mathbf{f}^{sim}_n ds \tag{6.24}$$

$$F^{sim}_{ij,mn} = \frac{\alpha Y^j}{Y^{sim}+Y^j}\int_{\Gamma_i} \mathbf{f}^{sim}_m \cdot (\hat{\mathbf{n}} \times \mathbf{\Phi}_n) ds$$
$$+\frac{(1-\alpha)\eta_0}{Z^{sim}+Z^j}\int_{\Gamma_i} (\hat{\mathbf{n}} \times \mathbf{f}^{sim}_m) \cdot (\hat{\mathbf{n}} \times \hat{\mathbf{n}} \times \mathbf{\Phi}_n) ds \tag{6.25}$$

$$G^{sim}_{ij,mn} = (\frac{\alpha Y^{sim}}{Y^{sim}+Y^j})\int_{\Gamma_i} \mathbf{f}^{sim}_m \cdot (\hat{\mathbf{n}} \times \mathbf{f}_{j,n}) ds$$
$$+\frac{(1-\alpha)\eta_0 Z^{(j)}}{Z^{sim}+Z^j}\int_{\Gamma_i} (\hat{\mathbf{n}} \times \mathbf{f}^{sim}_m) \cdot \mathbf{f}_{j,n} ds \tag{6.26}$$

And other matrices not related to SIM sub-domain have the same expressions as in chapter 5.

Up to this point, all sub-domains are still coupled together, the next step is using fixed point iteration [32] to separate all sub-domains. First, an initial guess solution is assigned to all sub-domains, then all sub-domains are solved one by one. When solving for the ith sub-domain, the solutions of all other sub-domains in the previous iteration step are used as an approximation in the corresponding terms to the right side of the equation. Then the final update equation, which can be solved by Gauss-Seidel method is obtained.

For SEM or FEM sub-domains we have

$$\begin{bmatrix} A_i & C_i & 0 \\ C_i^T & B_i & D_i \\ 0 & E_i & T_i \end{bmatrix} \begin{bmatrix} e^i_{i,k+1} \\ e^b_{i,k+1} \\ J_{i,k+1} \end{bmatrix} = \sum_{j \in neighbor(i)} \begin{bmatrix} 0 & 0 & 0 \\ 0 & B_{ij} & D_{ij} \\ 0 & E_{ij} & T_{ij} \end{bmatrix} \begin{bmatrix} e^i_{j,k} \\ e^b_{j,k} \\ J_{j,k} \end{bmatrix}$$
$$+ \begin{bmatrix} 0 & 0 \\ B^{sim}_{ij} & D^{sim}_{ij} \\ E^{sim}_{ij} & T^{sim}_{ij} \end{bmatrix} \begin{bmatrix} M_{sim,k} \\ J_{sim,k} \end{bmatrix} + \begin{bmatrix} y^i_i \\ y^b_i \\ 0 \end{bmatrix} \tag{6.27}$$

For the SIM sub-domain we have

$$\begin{bmatrix} B^{sim} & D^{sim} \\ Z_b & Z_a \end{bmatrix} \begin{bmatrix} M_{sim,k+1} \\ J_{sim,k+1} \end{bmatrix}$$

$$= \sum_{j \in neighbor(sim)} \begin{bmatrix} 0 & F_{ij} & G_{ij} \\ 0 & 0 & 0 \end{bmatrix} \begin{bmatrix} e^i_{j,k} \\ e^b_{j,k} \\ J_{j,k} \end{bmatrix} + \begin{bmatrix} 0 \\ y^{sim} \end{bmatrix} \tag{6.28}$$

From equations (6.27 and 6.28), it is clear when solving for the ith sub-domain, the information needed is the solutions of all neighbor sub-domains at the previous iteration, so the whole system is decoupled into many smaller systems.

After obtaining equations (6.27 and 6.28), the solving process can be done in two steps. The first step is to perform LU factorization for every sub-domain. The next step is to solve the equation by Gauss-Seidel iteration looping through all sub-domains. In the loop, first update the right-hand side for the current sub-domain using the solution obtained in the previous iteration. Then we solve for the current sub-domain and update the solution for current sub-domain. Pre-calculated LU factorization matrices are used to solve SEM and FEM sub-domains. An iterative solver is used to solve the SIM sub-domain, where the SIM is used to obtain the fast matrix-vector multiplications during each iteration [48]; and the solution of the SIM sub-domain at the previous iteration step is used as the initial guess in the iterative solver to reduce the number of iterations. When the residue of the Gauss-Seidel iteration is smaller than a prescribed tolerance, the program can be terminated. Other iterative solvers such as SOR or subspace can also be used, but in this work those materials are not included.

6.3 Comparison of SIM-SEM via Interpolation Matrix and Discontinuous Galerkin Method

In chapter 3 the SIM and SEM are connected by a interpolation matrix which is derived from the boundary condition on the interface of the SIM and SEM. So in chapter 3, only a special case is studied, that the SEM and SIM surface mesh is conforming. And if the interpolation matrix is used, there is only one the sub-domain can attached to SIM. If the problem is very large, the SEM sub-domain attached to SIM can be very large. And computational cost for the single large sub-domain will dominant computational cost.

Using DG between SIM and SEM can solve these two problems. First, the DG operator has the ability to deal with arbitrary non-conforming element on the interface. Second, it allows multiple sub-domains to attach to the SIM sub-domain. It can avoid the single large sub-domain.

So the SIM-SEM-FEM DDM is generally very flexible in geometrical modeling, as all surface mesh on the interface can be arbitrary non-conforming. The flexibility of the SIM-SEM-FEM DDM can solve the geometrical modeling difficulties has been mentioned in chapter 3.

6.4 Numerical Examples

The first example is used to show the capability of the proposed method to deal with an arbitrary non-conformal mesh. The scatterer is a dielectric cube with side length of 0.1 m and the relative permittivity $\epsilon_r = 9$. A plane wave at 600 MHz is incident in the z direction, with $\mathbf{E}$ field polarized in the x direction. This example is also solved by the conventional FEM in [27]. In the DDM, the whole problem is divided into 3 sub-domains, as shown in Fig. 6.3. The tetrahedron element based FEM is used for the central sub-domain (dielectric cube), hexahedron-element based second

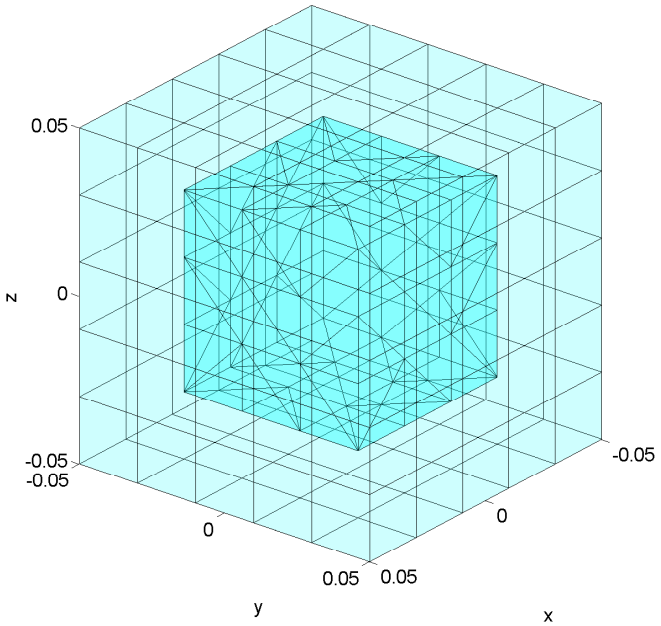

FIGURE 6.3: Non-conformal SIM-SEM-FEM mesh used for a dielectric cube with side length of 0.01 m

order SEM basis function is used for the region between SIM and FEM and the SIM is used for the outer boundary. The mesh is non-conformal as shown in Fig. 6.3. The bi-static RCS on the $\phi = 0°$ and $\phi = 90°$ planes are calculated. The SIM-SEM-FEM results are shown in the Fig. 6.4 with the MOM solution as a reference result. Note that in this case the SEM sub-domain is not necessary (it can also solved by conformal tetrahedron or hexahedron elements), but it is used to demonstrate that a non-conformal mesh can be used.

The convergence curve of the relative error in the Gauss-Seidel iteration is shown in Fig. 6.5.

In order to compare Riemann solver and Robin's boundary condition, the interface between exterior boundary integration part and interior finite element (spectral element) part is dealt with interpolation matrix [48], and only treat interface between finite element (spectral element) by Riemann solver or Robin's boundary condition.

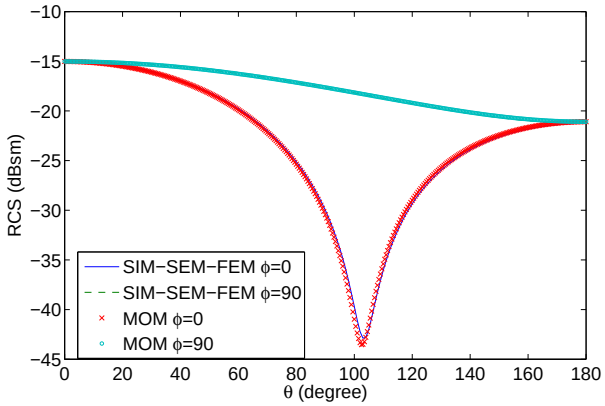

FIGURE 6.4: Bi-static RCS from a dielectric cube with side length of 0.01 m at 600 MHz, on the $\phi = 0°$ and $\phi = 90°$ planes.

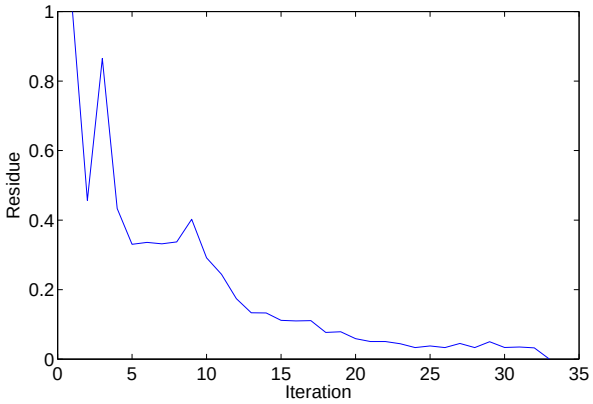

FIGURE 6.5: Convergence curve in the Gauss-Seidel iterative solver

We calcualted the spectral radius of the 2 systems, which are shown in the Fig. 6.6 and the Fig. 6.7. And convergence curves are shown in the Fig. 6.8

From this comparison, the Riemann solver shows much faster convergence rate than Robin's boundary condition.

To investigate the effects of different numbers of sub-domains, the SEM sub-domain is further divided into 2, 4, and 8 sub-domains (the total number of sub-domains are 4, 6 and 10) with the third-order SEM basis functions. All RCS results with different sub-domain divisions almost the same, as shown in Fig. 6.9. The CPU time and memory cost by different numbers of sub-domains are shown in Table

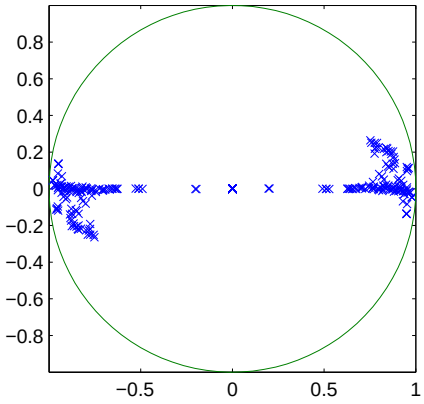

FIGURE 6.6: Spectral radius of the system obtained from the Robin's boundary condition

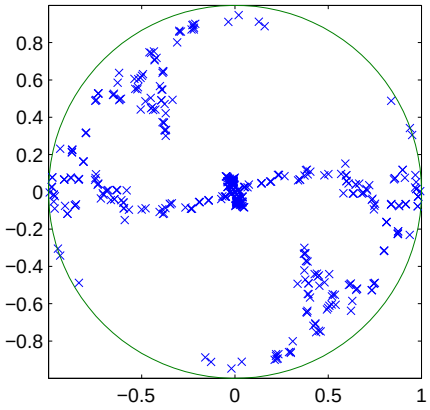

FIGURE 6.7: Spectral radius of the system obtained from the discontinuous Galerkin method

6.1. From table 6.1, it is observed that increasing the number of sub-domains can save both memory and CPU time. However, it is expected this change will become smaller after the number of sub-domains reaches a certain level.

The second example is used to validate the result of a dielectric coated PEC sphere. The radius of inner PEC core is 1.5 m; the outer radius of the coating is 1.05 m, and the relative permittivity of the coating part is $\epsilon_r = 4$. A plane wave at 300 MHz is incident in the z direction, with $\mathbf{E}$ field polarization in the x direction. This

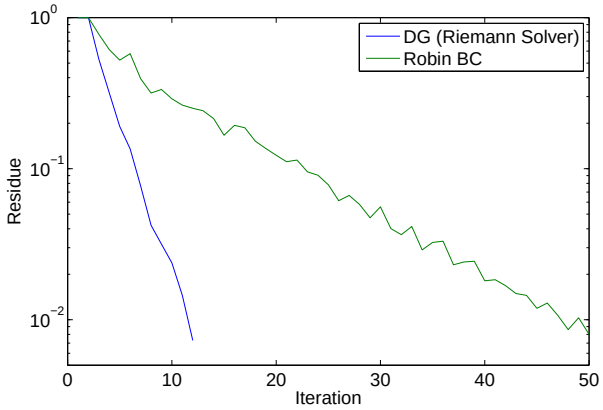

FIGURE 6.8: Convergence comparison of DDM by the DG method and DDM by Robin's boundary condition.

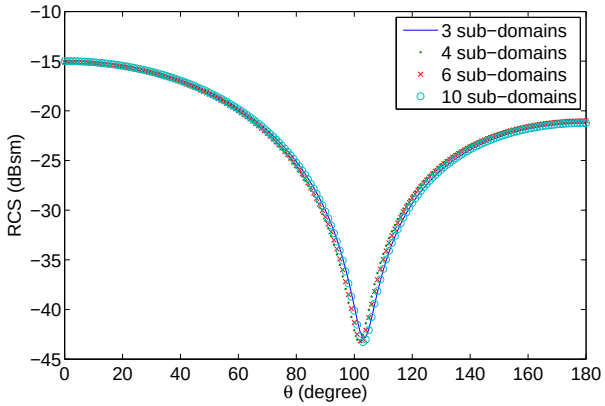

FIGURE 6.9: Bi-static RCS for $\phi = 0°$ from a dielectric cube with side length 0.01 m at 600 MHz, using different numbers of SEM sub-domains.

problem is divided into 17 sub-domains. The bi-static RCS for $\phi = 0°$ and $\phi = 90°$ are calculated and shown in Fig. 6.10. The numerical results agree well with the analytical results.

This example shows the SIM-SEM-DDM solved the geometrical modeling problem as mentioned in the chapter 3.

The third example is a PEC-dielectric composite object. The detailed dimensions and material properties are shown in Fig. 6.11. The source for this example is a 300 MHz plane wave incident in the z direction, with $\mathbf{E}$ field polarization in the x

Table 6.1: Memory and CPU time cost for a dielectric cube example, using different number of sub-domains.

number of sub-domains	3	4	6	10
Memory cost (MB)	149.2	124.4	100.6	98.8
CPU time (s)	577	412.8	263.1	171.9
number of GS iteration	36	37	42	51

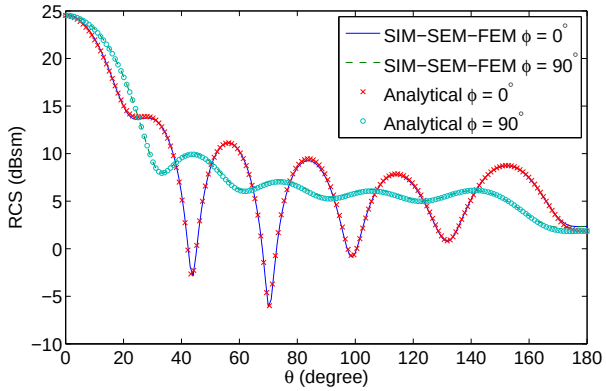

FIGURE 6.10: Bi-static RCS from a coated PEC sphere with PEC core radius=1.5 m and thickness of coating 0.05 m, coating material $\epsilon_r = 4$ at 300 MHz, in $\phi = 0°$ and $\phi = 90°$ plane

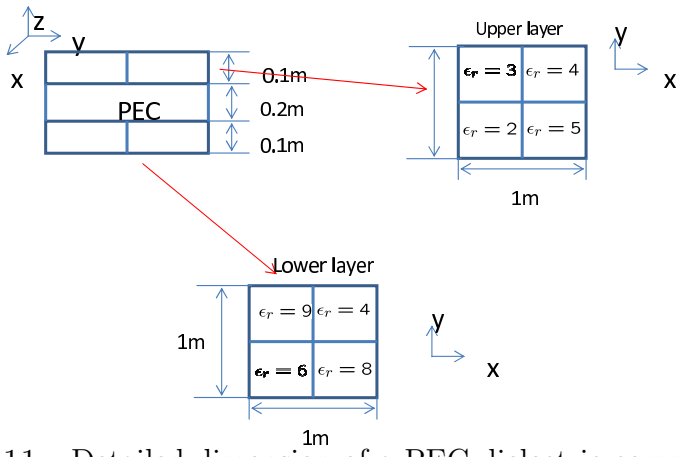

FIGURE 6.11: Detailed dimension of a PEC dielectric composite body

direction. The bi-static RCS in $\phi = 0°$ and $\phi = 90°$ planes are calculated and shown in Fig. 6.12 and Fig. 6.13. For this example, the DDM results agree well with the reference results obtained by software Wavenolgy [28].

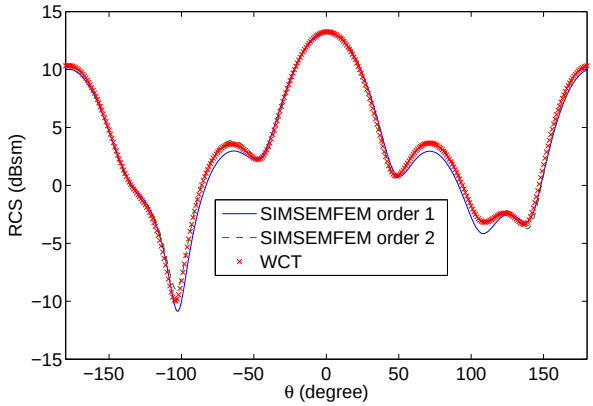

FIGURE 6.12: Bi-static RCS from a PEC dielectric composite body , at 300 MHz, in $\phi = 0°$ plane

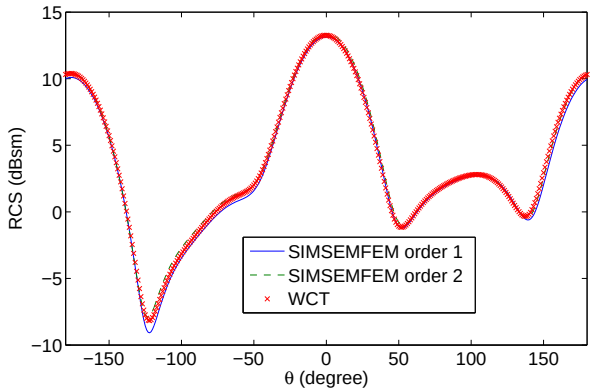

FIGURE 6.13: Bi-static RCS from a PEC dielectric composite body , at 300 MHz, in $\phi = 90°$ plane

The forth example is a single PEC reflector shown in Fig. 6.14. The reflector has four PEC plates each with dimensions of 0.3 m by 0.755 m by 0.004 m, and a circular cylinder with height of 0.85 m and radius of 0.01 m. The four plates are connected to each other by 90° forming a 'W' shape, and the cylinder goes through the center of the 'W'. The detailed dimension is shown in the fig. 6.15.

The ratio of the largest dimension to the smallest dimension in this example is 212.5. The source for this example is 300 MHz plane wave incident in the z direction, with $\mathbf{E}$ field polarization in the x direction. The bi-static RCS in $\phi = 0°$ and $\phi = 90°$

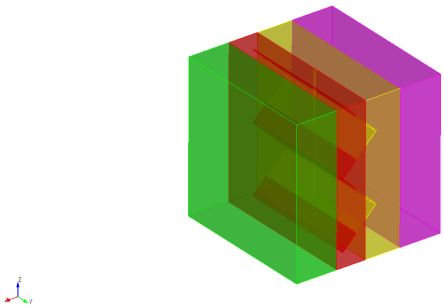

FIGURE 6.14: 3D model of the corner reflector.

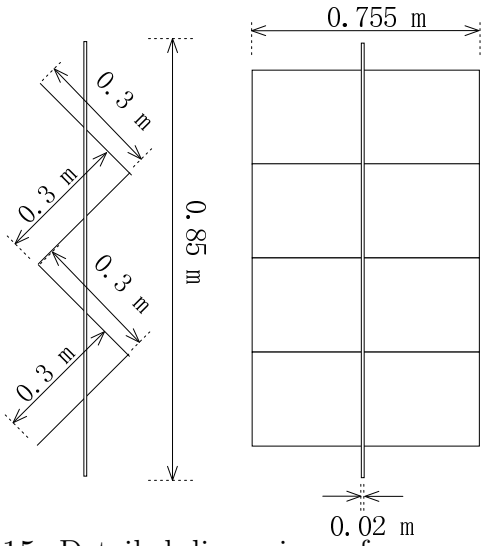

FIGURE 6.15: Detailed dimensions of a corner reflector.

planes are shown in Fig. 6.16.

The final example has two PEC reflectors, each with the same dimensions as in the fourth example; and the distance between these two reflectors is 0.84 m. The 3D model is shown in the Fig. 6.17. The ratio between the largest dimension and the smallest dimension in this example is 330. With the same incident plane wave, the bi-static RCS in $\phi = 0°$ and $\phi = 90°$ planes are shown in Fig. 6.18. The CPU time for SIM-SEM-FEM is 2,742 seconds and the memory cost is 960 Mb, while HFSS cost 6,643 seconds and cost 2.82 Gb memory on the same computer.

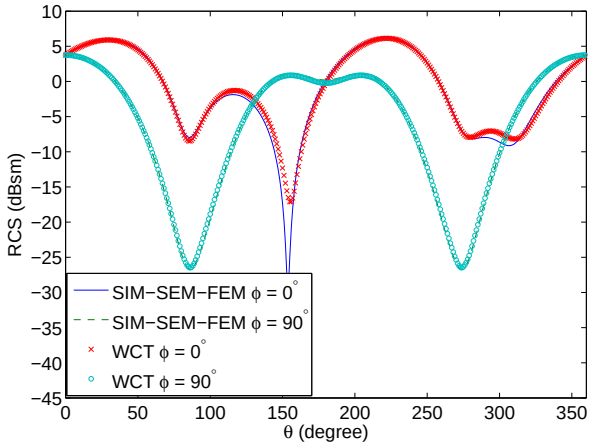

FIGURE 6.16: Bi-static RCS from a corner reflector at 300 MHz, in $\phi = 0°$ and $\phi = 90°$ plane

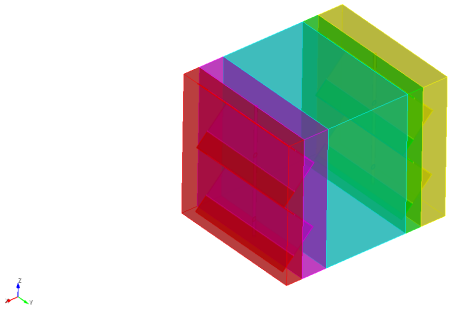

FIGURE 6.17: 3D model of 2 PEC reflectors

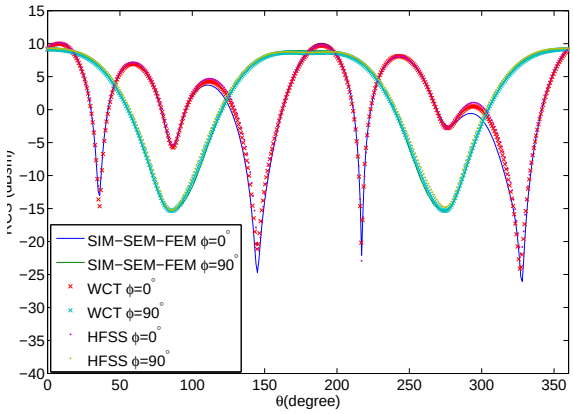

FIGURE 6.18: Bi-static RCS from 2 corner reflectors at 300 MHz, in $\phi = 0°$ and $\phi = 90°$ plane

6.5 Conclusion

In this chapter, we proposed the SIM-SEM-FEM via DG for multi-scale electromagnetic problems. This method hybridizes FEM, SEM and SIM into a DG scheme. In the DG scheme, Riemann solver is used as the numerical flux to connect different sub-domains. Instead of using conformal elements on SIM-SEM interfaces, as in chapter 3, the proposed method is able to use a non-conformal mesh between SIM-SEM or SIM-FEM interfaces. The proposed method is much more efficient both in memory and CPU time than the conventional FEM for multi-scale problems.

7

Future work

In this section, we will discuss some work that can be done in the near future, and can greatly enhance the capability of the current version SIM-FEM-SEM DDM.

7.1 DDM for Periodic Structures

Periodic structures have very interesting properties, and the propagation of electromagnetic wave in periodic structures is always a hot topic and gain much attention. The DDM algorithm is also very suitable for periodic structures (finite or infinite) such as photonic crystal structure or antenna arrays. In these problems the "cell" structures exist repeatedly. Due to this nature, DDM can model only one "cell". Basically, the memory cost will not increase as the number of cells increases, (the memory used to store the LU factorization of system matrix account more than 80 percent of the total memory usage) only LU factorization of one cell needs to be stored in memory. The memory requirement can be greatly reduced.

7.2 DDM for Integral Equation Methods

In this work, FEM or SEM region can be divided into many sub-domains, but the integral equation is always only one domain. If the problem size grows sustainably, the FEM can be further divided into smaller sub-domains to reduce the computational costs. But in the IE part, because of the global coupling of the Green's function, the conventional integral equation cannot be divided into sub-domains. A single large IE sub-domain increases the computational costs. Some recent work [49] shows that it is also possible to do DDM for integral equation. As a result, the computational cost of the IE part can be further reduced.

8

Conclusion

A SIM-SEM-FEM DDM algorithm is proposed to solve inhomogeneous multi-scale problems. In the DDM scheme, whole computational domain is divideod into sub-domains. Electrically fine and coarse structures are modeled by FEM and SEM, respectively. The SIM (which is treat as a single sub-domain too) is used as an efficient boundary condition. The discontinuous Galerkin method is used to connect all sub-domains. The DG scheme allows size and type of elements in different sub-domains to be totally independent. The non-conforming DG can reduce the number of elements and convert the original one large problem into several small problems. Numerical results show the proposed method is more efficient than conventional methods.

9

Appendix I : Generation of the Triangles Meshes Shared by 2 Non-conforming Meshes

The discontinuous Garlerkin method need to evaluate the integration of basis function defined in a different sub-domain. For example there is an interface between sub-domain 1 and 2. We need to calculate the integration of basis function defined in sub-domain 1 on the surface mesh of sub-domain 2. So we need to find the polygon shared by the surface element from 2 sub-domains.

The first step is to find the bonding box of 2 polygon. If they have overlap area,

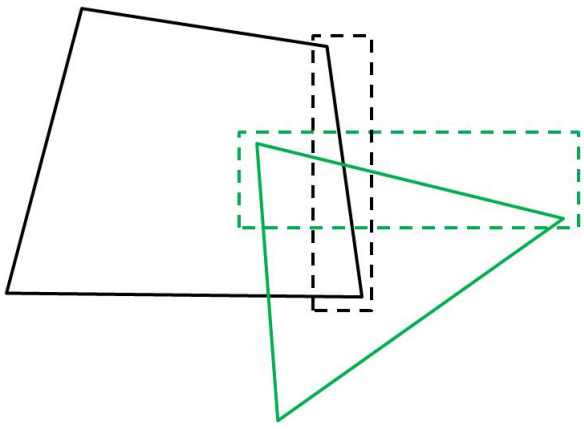

FIGURE 9.1: Two sets of mesh on the interface between sub-domains

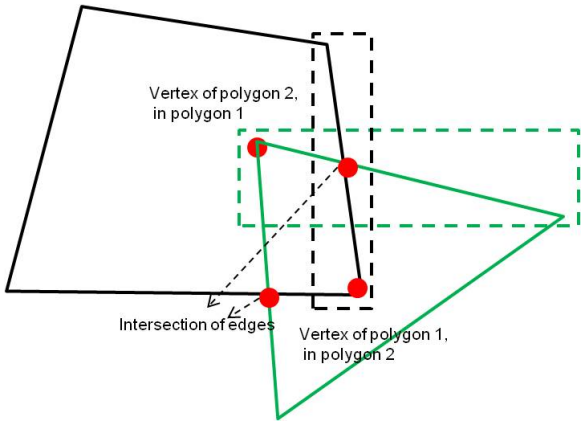

FIGURE 9.2: Vertex of the polygon of the shared area of polygon 1 and polygon 2

continue with vertex finding procedure.

- Bounding box for 2 polygons have overlap

The second step is to find all the vetex for the polygon shared area by 2 polygon. The vertexes for the polygon shared area by 2 polygon include 3 types, as shown in Fig. 9.2.

- Vertexes of polygon 2 inside polygon 1
- Vertexes of polygon 1 inside polygon 2
- Intersections of all edges (most time consuming parts)

The third step is reorder all vertex in a correct orderas shown in Fig. 9.3.

- Reorder all points

As mentioned above, the algorithm for finding the intersection of 2 lines in 3D space is needed. The algorithm for finding intersection of 2 lines in 3D space is discussed in following part [50].

The parameter equation for line defined by a point $\mathbf{P}_1$ and a unit direction $\hat{\mathbf{V}}_1$, in 3D space can be expressed as

$$\mathbf{L}_1(t) = \mathbf{P}_1 + \hat{\mathbf{V}}_1 t \tag{9.1}$$

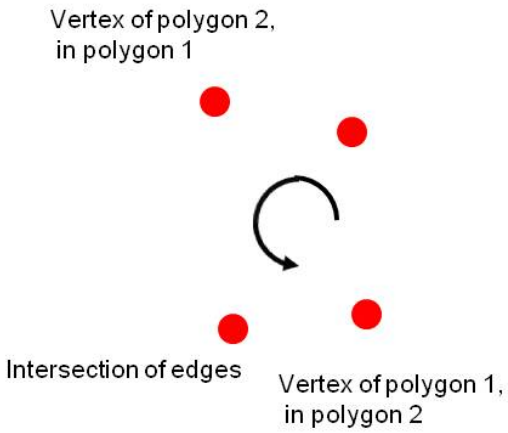

FIGURE 9.3: Reorder vertexes of the polygon of the shared area of polygon 1 and polygon 2

Another line in 3D space, defined by a point $\mathbf{P}_2$ and a unit direction $\hat{\mathbf{V}}_2$

$$\mathbf{L}_2(s) = \mathbf{P}_2 + \hat{\mathbf{V}}_2 s \tag{9.2}$$

The intersection of these 2 lines occurs when

$$\mathbf{L}_1(t) = \mathbf{L}_2(s) \tag{9.3}$$

or,

$$\mathbf{P}_1 + \hat{\mathbf{V}}_1 t = \mathbf{P}_2 + \hat{\mathbf{V}}_2 s \tag{9.4}$$

move $\mathbf{P}_1$ to the right hand side, and cross 2 sides by $\hat{\mathbf{V}}_2$

$$\hat{\mathbf{V}}_1 \times \hat{\mathbf{V}}_2 t = (\mathbf{P}_2 - \mathbf{P}_1) \times \hat{\mathbf{V}}_2 \tag{9.5}$$

Then dotting two side by $\hat{\mathbf{V}}_1 \times \hat{\mathbf{V}}_2$

$$(\hat{\mathbf{V}}_1 \times \hat{\mathbf{V}}_2) \cdot (\hat{\mathbf{V}}_1 \times \hat{\mathbf{V}}_2) t = (\hat{\mathbf{V}}_1 \times \hat{\mathbf{V}}_2) \cdot [(\mathbf{P}_2 - \mathbf{P}_1) \times \hat{\mathbf{V}}_2] \tag{9.6}$$

$$t = \frac{(\hat{\mathbf{V}}_1 \times \hat{\mathbf{V}}_2) \cdot [(\mathbf{P}_2 - \mathbf{P}_1) \times \hat{\mathbf{V}}_2]}{(\hat{\mathbf{V}}_1 \times \hat{\mathbf{V}}_2) \cdot (\hat{\mathbf{V}}_1 \times \hat{\mathbf{V}}_2)} \tag{9.7}$$

by the same manner

$$s = \frac{(\hat{\mathbf{V}}_1 \times \hat{\mathbf{V}}_2) \cdot [(\mathbf{P}_2 - \mathbf{P}_1) \times \hat{\mathbf{V}}_2]}{(\hat{\mathbf{V}}_1 \times \hat{\mathbf{V}}_1) \cdot (\hat{\mathbf{V}}_1 \times \hat{\mathbf{V}}_2)} \tag{9.8}$$

If $(\hat{\mathbf{V}}_1 \times \hat{\mathbf{V}}_2) = 0$, 2 lines are parallel to each other. If 2 points obtained by t and s are not the same point, 2 lines are skew, and 2 points represented by t and s parameters are the closest points on 2 lines. If the points obtained by t and s are the same point, the point represented by t and s parameters is the intersection point of 2 lines.

Bibliography

[1] R. F. Harrington, *Field Computation by Moment Methods.* NewYork: MacMillian, 1968.

[2] R. Coifman, V. Rokhlin, and S.Wandzura, "The fast multipole method for the wave equation: A pedestrian prescription," *IEEE Trans. Antennas Propag.*, vol. 35, pp. 7–12, 1993.

[3] J. M. Song and W. C. Chew, "Multilevel fast-multipole algorithm for solving combined field integral equations of electromagnetic scattering," *Microw. Opt. Technol. Lett*, vol. 10, pp. 15–19, 1995.

[4] E. Bleszynski, M. Bleszynski, and J. Jaroszewicz, "AIM: Adaptive integral method for solving large-scale electromagnetic scattering and radiation problems," *Radio Sci.*, vol. 31, pp. 1225–1251, 1996.

[5] F. Ling, C. F. Wang, and J. M. Jin, "Application of adaptive integral method to scattering and radiation analysis of arbitrarily shaped planar structures," *J. Electromag. Waves Applicat.*, vol. 12, pp. 1021–1038, Aug. 1998.

[6] J. M. Jin, J. L. Volakis, and J. D. Collins, "A finite element boundary integral method for scattering and radiation by two- and three-dimensional structures," *IEEE Antennas Propag. Mag.*, vol. 33, pp. 22–32, Jun. 1991.

[7] J. M. Jin and J. L.Volakis, "A finite element-boundary integral formulation for scattering by three-dimensional cavity backed apertures," *IEEE Trans. Antennas Propag.*, vol. 39, pp. 97–104, 1991.

[8] E. Simsek, J. Liu, and Q. H. Liu, "A spectral integral method and hybrid SIM/FEM for layered media," *IEEE Trans. Microw. Theory Tech.*, vol. 54, no. 11, pp. 3878–3884, Nov. 2006.

[9] Q. H. Liu, Y. Lin, J. Liu, J.-H. Lee, and E. Simsek, "A 3-D spectral integral method (SIM) for surface integral equations," *IEEE Microw. Wireless Compon. Lett.*, vol. 19, no. 2, pp. 62–64, Feb. 2009.

[10] E. Lucente and A. Monorchio, "A parallel iteration-free MOM algorithm based on the characteristic basis functions method," *URSI Electromagnetic Theory Symposium, Ottawa, ON, Canada*, pp. 26–28, Jul. 2007.

[11] J. M. Jin, *The Finite Element Method in Electromagnetics.* New York: Wiley, 1993.

[12] J. L. Volakis, A. Chatterjee, and L. C. Kempel, *Finite Element Method for Electromagnetics.* Piscataway, N.J.: IEEE Press, 1998.

[13] J. Berenger, "A perfectly matched layer for the absorption of electromagnetic waves," *Journal of Computational Physics*, vol. 114, pp. 185–200, 1994.

[14] B. Stupfel, "A study of the condition number of various finite element matrices involved in the numerical solution of maxwell's equations," *IEEE Trans. Antennas Propag.*, vol. 52, no. 11, Nov. 2004.

[15] J. M. Jin and V. V. Liepa, "Application of hybrid finite element method to electromagnetic scattering from coated cylinders," *IEEE Trans. Antennas Propag.*, vol. 36, no. 1, pp. 50–54, Jan. 1988.

[16] K. D. Paulsen, D. R. Lynch, and J. W. Strahbehn, "Three-dimensional finite, boundary, and hybrid element solutions of the maxwell equations for lossy dielectric media," *IEEE Trans. Microw. Theory Tech.*, vol. 36, no. 4, pp. 682–693, Apr. 1988.

[17] D. J. Hoppe, L. W. Epp, and J. F. Lee, "A hybrid symmetric FEM/MOM formulation applied to scattering by inhomogeneous bodies of revolution," *IEEE Trans. Antennas Propag.*, vol. 42, no. 6, Jun. 1994.

[18] U. Pekel and R. Mittra, "A first order hybrid FEM/MOM approach for the analysis of two dimensional structures," *Microwave and Opt. Tech. Lett.*, vol. 8, no. 2, Feb. 1995.

[19] M. W. Ali, T. H. Hubing, and J. L. Dreniak, "A hybrid FEM/MOM technique for electromagnetic scattering and radiation from dielectric objects with attached wires," *IEEE Trans. Electromagn. Compat.*, vol. 39, pp. 304–314, Nov. 1997.

[20] X. Q. Sheng, J. M. Jin, J. M. Song, C. C. Lu, and W. Chew, "On the formulation of hybrid finite-element and boundary-integral method for 3d scattering," *IEEE Trans. Antennas Propag.*, vol. 46, no. 3, pp. 303–311, Mar. 1998.

[21] J. Liu and J. M. Jin, "A novel hybridization of higher order finite element and boundary integral methods for electromagnetic scattering and radiation problems," *IEEE Trans. Antennas Propag.*, vol. 49, no. 12, pp. 1794–1806, Dec. 2001.

[22] J. Liu and Q. H. Liu, "A spectral integral method (SIM) for periodic and non-periodic structures," *IEEE Microw. Wireless Compon. Lett.*, vol. 14, no. 3, pp. 97–99, Mar. 2004.

[23] E. Simsek, J. Liu, and Q. H. Liu, "A spectral integral method (SIM) for layered media," *IEEE Trans. Antennas Propag.*, vol. 54, no. 6, pp. 1742–1749, Jun 2006.

[24] J. Liu and Q. H. Liu, "A novel radiation boundary condition for finite-element method," *Microwave Opt. Technol. Lett.*, vol. 49, no. 8, pp. 1995–2002, 2007.

[25] J. H. Lee, T. Xiao, and Q. H. Liu, "A 3-D spectral-element method using mixed-order curl conforming vector basis functions for electromagnetic fields," *IEEE Trans. Microw. Theory Tech.*, vol. 54, no. 1, pp. 437–444, Jan. 2006.

[26] L. G. Sleijpen and D. R. Fokkema, "Bicgstab(l) for linear equations involving unsymmetric matrices with complex spectrum," *Electronic Transactions on Numerical Analysis*, vol. 1, pp. 11–32, Sep. 1993.

[27] A. F. Peterson, S. L. Ray, and R. Mittra, *Computational Methods for Electromagnetics*. New York: Wiley-IEEE Press, Dec. 1997.

[28] T. Xiao and Q. H. Liu, "Enlarged cells for the conformal FDTD method to avoid the time step reduction," *IEEE Microw. Wireless Compon. Lett.*, vol. 14, no. 12, pp. 551–553, Dec. 2004.

[29] ——, "A 3-D enlarged cell technique (ECT) for the conformal fdtd method," *IEEE Trans. Antennas Propag.*, vol. 56, no. 3, pp. 765–773, Mar. 2008.

[30] P. P. Silvester and R. L. Ferrari, *Finite Elements for Electrical Engineers*, 3rd ed. Cambridge University Press, Sep. 1996.

[31] B. Despre, "Méthodes de deomposition de domaine pour les problémes de propagation dóndes en régime harmonique," Ph.D. dissertation, 1991.

[32] S.-C. Lee, M. N. Vouvakis, and J.-F. Lee, "A non-overlapping domain decomposition method with non-matching grids for modeling large finite antenna arrays," *J. Comput. Phys.*, vol. 203, pp. 1–21, Feb. 2005.

[33] M. N. Vouvakis, Z. Cendes, and J.-F. Lee, "A fem domain decomposition method for photonic and electromagnetic band gap structures," *IEEE Trans. Antennas Propag.*, vol. 54, pp. 721–733, Feb. 2006.

[34] B. Stupfel, "A fast-domain decomposition method for the solution of electromagnetic scattering by large objects," *IEEE Trans. Antennas Propag.*, vol. 44, pp. 1375–1385, Oct. 1996.

[35] M. Gander, F. Magouls, and F. Nataf, "Optimized schwarz methods without overlap for the helmholtz equation," *SIAM J. Sci. Comput.*, vol. 24, no. 1, pp. 38–60, 2002.

[36] B. Smith, P. Bjrstad, and W. Gropp, *Domain Decomposition Parallel Multilevel Methods for Elliptic Partial.* New York: Cambridge University Press, Cambridge University Press, 1996.

[37] A. Quarteroni and A. Valli, *Domain Decomposition Methods for Partial Differential Equations.* New York: Oxford University Press, 1999.

[38] G. Cohen, X. Ferrieres, and S. Pernet, "A spatial high-order hexahedral discontinuous Galerkin method to solve maxwell's equations in time domain," *J. Comput. Phys.*, vol. 217, pp. 340–363, Feb. 2006.

[39] K. Yee, "Numerical solution of initial boundary value problems involving Maxwell's equations in isotropic media," *IEEE Trans. Antennas Propag.*, vol. 14, pp. 302–307, 1966.

[40] A. Taflove, "Application of the finite-difference time-domain method to sinusoidal steady state electromagnetic penetration problems," *IEEE Trans. Electromagn. Compat.*, vol. 22, pp. 191–202, 1980.

[41] D. Sheen, S. Ali, M. Abouzahra, and J. Kong, "Application of the three-dimensional finite-difference time-domain method to the analysis of planar microstrip circuits," *IEEE Trans. Microw. Theory Tech.*, vol. 38, no. 7, pp. 849–857, Jul. 2006.

[42] S.-h. Lee, "Efficient finite element electromagnetic analysis for high-frequency/high-speed circuits and multiconductor transmission lines," Ph.D. dissertation, UIUC, 2009.

[43] K. Guillouard, M. F. Wong, V. F. Hanna, and J. Citerne, "A new global finite element analysis of microwave circuits including lumped elements," *IEEE Trans. Microw. Theory Tech.*, vol. 44, no. 12, pp. 2587–2594, Dec. 1996.

[44] M. Feliziani and F. Maradei, "Modeling of electromagnetic fields and electrical circuits with lumped and distributed elements by the wetd method," pp. 1666–1669, May 1999.

[45] A. D. Grigoryev, R. V. Salimov, and R. I. Tikhonov, "Multiple-cell lumped element and port models for the vector finite element method," *Electromagnetics*, vol. 28, pp. 18–26, 2008.

[46] B. Cockburn, G. Karniadakis, and C.-W. Shu, "The development of discontiunuous Galerkin methods lecture notes," *Computational Science and Engineering*, vol. 11, 2000.

[47] I. Perugia, D. Schtzau, and P. Monk, "Stabilized interior penalty methods for time-harmonic Maxwell equations," *Comput. Meth. Appl. Mech. Eng.*, vol. 191, pp. 4675–4697, 2002.

[48] Y. Lin, J. H. Lee, J. Liu, M. Chai, J. A. Mix, and Q. H. Liu, "A hybrid SIM-SEM method for 3-D electromagnetic scattering problems," *IEEE Trans. Antennas Propag.*, vol. 57, no. 11, pp. 3655–3663, Nov. 2009.

[49] Z. Peng, X. chuan Wang, and J.-F. Lee, "Integral equation domain decomposition method for solving electromagnetic wave scattering from non-penetrable objects," *ICEAA*, pp. 20–24, Sep. 2010.

[50] A. S. Glassner, *Graphics Gems*. Academic Press Inc., 1990.

Biography

The author (Yun Lin) was born on May 18, 1981, in Leshan, Sichuan province P. R. China. He received B.S. and M.S. degree in Microwave Engineering in 2003 and 2006 respectively from University of Electronic Science and Technology of China (UESTC), in Chengdu, Sichuan province P. R. China. He received Ph. D. degree in Electrical and Computer Engineering from Duke University in 2011, Durham, North Carolina, U. S. He published 2 journal papers and submitted anohter 2 papers, during his Ph. D. period.